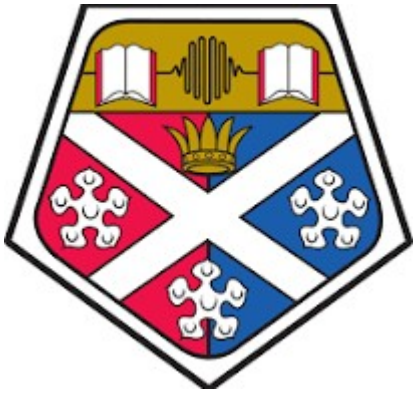

University of Strathclyde Glasgow

Department of Naval Architecture, Ocean and Marine Engineering

A numerical model for the simulation of hydrogen embrittlement mechanism in presence of dynamic hydrogen coverage

A thesis submitted in fulfilment of the requirements for the degree of Doctor of Philosophy

Dario Gavina

2026

This thesis is the result of the Author's original research. It has been composed by the Author and has not been previously submitted for examination which has led to the award of a degree.

Volli, e Sempre Volli, e Fortissimamente Volli

A Raffaella, Daniele e Federico

This dissertation is the culmination of a journey that would not have been possible without the unwavering support, guidance, and encouragement of many remarkable individuals. It is with profound gratitude that I acknowledge their contributions.

First and foremost, I wish to express my deepest gratitude to my supervisor, Professor Erkan Oterkus and Prof. Selda Oterkus. Your boundless enthusiasm, your insightful guidance, and your unwavering patience have been the bedrock of this project. Thank you for challenging me to think more critically, for your steadfast support during moments of doubt, and for your mentorship that extended far beyond the confines of this thesis.

My most profound debt of gratitude is to my family. To my parents, Daniele Gravina and Vincenza Simone, thank you for your unconditional love and support throughout my entire education. You instilled in me a curiosity about the world and the belief that I could achieve anything I set my mind to. This achievement is as much yours as it is mine.

To my wife Raffaella, words cannot express my gratitude. You have been my rock, my confidant, and my greatest source of strength. Thank you for your endless patience, for believing in me even when I did not believe in myself, and for shouldering more than your share to allow me to pursue this dream. I could not have done this without you.

And to Daniele and Federico, thank you for your love and for providing the perfect, joyful distractions that kept everything in perspective. You are the reason for everything.

I gratefully acknowledge the financial support provided by the McDermott International via ECIBT Engineering Construction Industry Training Board.

Finally, I acknowledge that any errors or omissions in this work are mine alone.

Metallic materials are widely used in industrial structures and components. However, hydrogen embrittlement significantly degrades the mechanical behaviour of metals and alloys, compromising structural integrity in numerous industrial applications. One of the major challenges of our time is the development of models that predict the onset and propagation of damage in corrosive environments. This thesis aims to contribute to this goal by using cohesive zone models and a mechanistic characterization of the mechanical behaviour in the vicinity of the crack.

First, a cohesive crack model is proposed capable of modelling damage due to static and hydrogen embrittlement. The developed numerical framework includes, in a coupled manner,

- mass transport, incorporating the influence of microstructural traps, and
- mechanical behaviour characterized by the plasticity theory at finite strains, and
- cracking with dynamic hydrogen coverage.

The model qualitatively reproduces the relevant trends observed in the experimental tests, and the existing quantitative differences are extensively discussed. The results show that a significantly higher hydrogen concentration in the fracture process zone is required to achieve quantitative agreement. One possibility, consistent with microscale experiments and dislocation dynamics simulations, is that stress, and consequently hydrogen concentration increases considerably when plastic strain gradients accumulate in a small volume. This effect of inhomogeneous plastic deformation and its stress rise can be captured in the continuum by strain gradient theories.

The model also qualitatively reproduces the hydrogen dynamic coverage and provides inside of the importance associated with the correct implementation and modelling of the mentioned phenomena with the numerical analysis.

Table of Content

Table of Figures

Nomenclature

AISI	American Iron and Steel Institute
BC	Boundary Condition
CMSG	Conventional Mechanism Strain Gradient Plasticity
CZM	Cohesive Zone Model
FPZ	Fracture Process Zone
FTU	Specified Ultimate Tensile Strength
GNDs	Geometrically Necessary Dislocations
HEAC	Hydrogen Environment Assisted Cracking
HEDE	Hydrogen-enhanced decohesion
HELP	Hydrogen-enhanced localized plasticity
IHAC	Internal Hydrogen Assisted Cracking
MSG	Mechanism-based Strain Gradient Plasticity
NILS	Normal Interstitial Lattice Sites
SGP	Strain Gradient Plasticity
SIF	stress intensity factor
SSDS	Statistically Stored Dislocations
TSL	Traction Separation Law

Terminology

C	Total hydrogen concentration
C_L	Total hydrogen concentration
C_T	Total hydrogen concentration
J_m	Hydrogen Flux
S	Hydrogen Source Term
N_L	Lattice site density
N_T	Trap site density
N_A	Avogadro constant
β	Number of interstitial lattice sites per iron (Fe) atom
ρ	Density of material
A_r	molar mass of Fe
K_T	equilibrium constant
ΔW_B	binding enthalpy
ε_p	Equivalent plastic strain:
$\bar{a}$	lattice parameter of BBC iron
$\bar{\rho}$	density of dislocation
$\bar{\rho}_0$	dislocation density for annealed material
D_L	effective diffusivity of interstitial concentration (lattice part);
V_H	partial molar volume;
R	universal gas constant
T	thermodynamic temperature

σ_H	hydrostatic stress.
Γ_0	fracture energy
$\sigma_{max,0}$	tensile strength in absence of hydrogen
σ_{max,θ_H}	tensile strength in presence of hydrogen
l_{ch}	material's characteristic length
k	cohesive energy scaling factor
ψ	ratio between the hydrogen concentration and the concentration of hydrogen at saturation level
θ_H	concentration of hydrogen
$\overline{\theta_H}$	concentration of hydrogen at saturation level
u_y	Displacement along y axis
E	Young's Modulus
ϑ	Poisson's Ratio

1 Introduction

1.1 Hydrogen cracking

Hydrogen embrittlement (HE) is a pervasive and complex phenomenon that poses a significant threat to the structural integrity of metallic materials, particularly high-strength steels used in subsea pipelines. This form of degradation occurs when atomic hydrogen diffuses into the metal lattice, leading to a loss of ductility, premature crack initiation, and catastrophic failure under stress levels far below the material's yield strength. The consequences of HE are particularly severe in subsea environments, where pipelines are subjected to high hydrostatic pressures, corrosive seawater, and cyclic loading, all of which exacerbate hydrogen uptake and subsequent embrittlement.

As per above, subsea pipelines operate in harsh offshore environments where they are continuously exposed to hydrostatic pressure, corrosive seawater, and cyclic mechanical loading that can accelerate fatigue damage and structural degradation. Cyclic loading arises from internal pressure fluctuations, wave and current actions, vortex-induced vibrations, thermal expansion and contraction, and operational start-up or shut-down events. Temperature changes create repeated expansion and contraction stresses that may lead to buckling or crack initiation over time. When excitation frequencies from flow turbulence, rotating equipment, or ocean currents approach the pipeline’s natural frequency, resonance can occur, producing significantly larger vibration amplitudes and increasing fatigue risk. To manage these conditions, operators implement instrumentation strategies using strain gauges, accelerometers, pressure and temperature sensors, corrosion monitoring probes, and distributed fiber-optic sensing systems for continuous structural health monitoring. Inspection and maintenance protocols typically follow risk-based integrity management standards, combining real-time monitoring with periodic remotely operated vehicle surveys and non-destructive testing to ensure long-term operational safety and reliability.

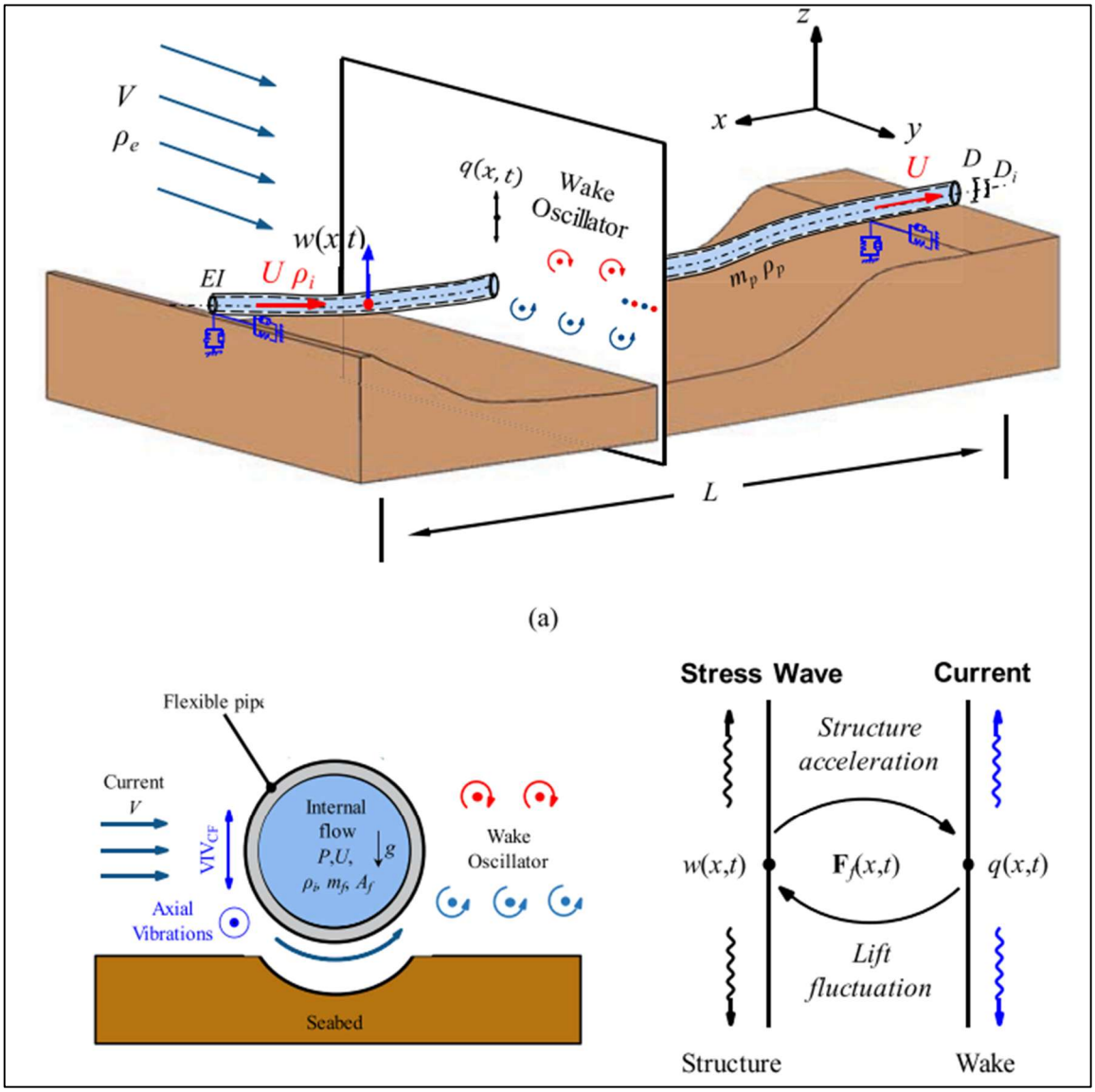

Figure 1-1: Examples of type of loading on the subsea pipelines *[1]*

To note that gas and hydrogen pipelines must differ because hydrogen has unique physical and chemical properties that create additional engineering challenges. Hydrogen molecules are much smaller than methane molecules in natural gas, which increases leakage risks and requires tighter seals and higher material integrity. As mentioned above, major challenge is hydrogen embrittlement, where hydrogen diffuses into steel and weakens the pipe material, potentially causing cracks and failures under pressure. Geometry and scale also play an important role. To transport the same amount of energy, hydrogen pipelines generally require larger diameters or higher flow velocities because hydrogen has a much lower volumetric energy density than natural gas. For example, hydrogen carries roughly one-third of the energy per cubic meter compared with natural gas. This means that, at equal pressure and pipe

diameter, a hydrogen pipeline delivers significantly less energy. In addition, hydrogen compression consumes more energy due to its low density, increasing operational costs and affecting the design of compressors and storage systems.

The mechanisms of hydrogen embrittlement have been extensively studied, yet they remain a subject of debate among researchers. Three primary theories dominate the literature: (1) Hydrogen-Enhanced Decohesion (HEDE), which posits that hydrogen reduces the cohesive strength of atomic bonds at crack tips or grain boundaries; (2) Hydrogen-Enhanced Localized Plasticity (HELP), where hydrogen facilitates dislocation motion, leading to localized plastic deformation and crack propagation; and (3) Adsorption-Induced Dislocation Emission (AIDE), a hybrid mechanism combining decohesion and plasticity effects. While these theories provide valuable insights, the precise interplay between hydrogen and microstructural features – such as grain boundaries, precipitates, and dislocations – remains an active area of research.

Subsea pipelines are particularly vulnerable to hydrogen embrittlement due to their exposure to hydrogen-producing environments. Cathodic protection (CP), a widely used corrosion prevention technique, can inadvertently introduce hydrogen into the steel through electrochemical reduction reactions. Additionally, operational conditions such as high-pressure hydrogen gas transport, sour service (H_2S – containing environments), and mechanical stress further accelerate hydrogen ingress. The problem is compounded in aging infrastructure, where pre-existing defects, fatigue damage, and weld residual stresses create preferential sites for hydrogen-assisted cracking.

The increasing demand for hydrogen as a clean energy carrier has further intensified research into HE, as new pipelines are being designed to transport pure hydrogen or hydrogen-natural gas blends. However, existing codes and standards – developed primarily for hydrocarbon service – may not adequately address the unique challenges posed by hydrogen. Thus, understanding HE in both existing and new subsea pipelines is critical for ensuring long-term structural reliability and preventing environmentally disastrous failures.

1.2 Background and Motivation

The oil and gas industry has long recognized hydrogen embrittlement as a critical failure mechanism in subsea pipelines. Historical incidents, such as the catastrophic failure of high-strength steel components in offshore platforms and subsea risers, have underscored the need for rigorous assessment and mitigation strategies. For instance, the failure of the Piper Alpha platform in 1988, though primarily caused by a gas leak, highlighted the role of material degradation in offshore disasters. More recently, hydrogen-related failures in subsea umbilicals and pipelines transporting sour gas have reinforced the urgency of understanding HE in deep-water applications.

The transition towards renewable energy and the growing interest in hydrogen as a sustainable fuel have introduced new challenges. Existing pipelines, originally designed for natural gas, are being repurposed for hydrogen transport, raising concerns about material compatibility. Hydrogen molecules, being significantly smaller than methane, can permeate steel more easily, leading to enhanced embrittlement risks. Moreover, the higher pressures required for efficient hydrogen transport exacerbate the susceptibility to HE. These factors necessitate a fundamental reassessment of pipeline design, material selection, and integrity management practices.

The motivation for this study stems from several critical gaps in current knowledge:

- **Lack of Predictive Models for Subsea Conditions**: Most HE models are derived from laboratory tests under idealized conditions, which may not accurately replicate the complex loading and environmental factors in subsea pipelines.
- **Insufficient Data on Hydrogen Transport Effects**: While hydrogen embrittlement in static conditions is well-documented, the combined effects of flowing hydrogen, cyclic pressure fluctuations, and seawater corrosion remain poorly understood.
- **Material Compatibility for Hydrogen Service**: Existing pipeline steels were not originally designed for hydrogen transport, and their long-term performance under hydrogen exposure is uncertain.
- **Weld and Heat-Affected Zone (HAZ) Susceptibility**: Welded joints are particularly prone to HE due to microstructural heterogeneities and residual stresses, yet standardized testing methods for assessing weld integrity in hydrogen environments are lacking.

Addressing these gaps is essential for ensuring the safe and economic deployment of hydrogen infrastructure, whether through the repurposing of existing pipelines or the development of new hydrogen-compatible materials.

1.3 Researching Activities and modelling approaches

As general trend, the current research activities aim to develop a comprehensive understanding of hydrogen embrittlement in both existing and new subsea pipelines, with a focus on predictive modelling, experimental validation, and mitigation strategies. The research is structured around the following key objectives:

1. **Characterization of Hydrogen-Material Interactions**: Investigate the diffusion kinetics, trapping mechanisms, and hydrogen-induced cracking behaviour in pipeline steels under subsea conditions. Advanced techniques such as thermal desorption spectroscopy (TDS), scanning Kelvin probe force microscopy (SKPFM), and in-situ

electrochemical hydrogen charging will be employed to quantify hydrogen uptake and localization.

2. **Development of a Multiscale HE Model**: Establish a coupled diffusion-mechanics framework that integrates atomistic simulations (density functional theory, DFT), microstructural modelling (crystal plasticity finite element method, CPFEM), and continuum-based fracture mechanics to predict hydrogen-assisted crack initiation and growth.
3. **Experimental Validation under Realistic Conditions**: Conduct slow strain rate tests (SSRT), fracture toughness tests, and fatigue crack growth experiments under simulated subsea environments (seawater, cathodic protection, and high-pressure H_2). The influence of variable loading (e.g., pressure fluctuations due to tidal effects or operational changes) will be examined.
4. **Assessment of Existing and New Pipeline Materials**: Evaluate the HE susceptibility of conventional API 5L steels (X65, X70) and advanced high-strength steels (X80, X100) under hydrogen exposure. The role of microalloying (e.g., Nb, V, Ti) and microstructure (ferrite-pearlite vs. acicular ferrite) in mitigating HE will be analyzed.
5. **Mitigation Strategies for Hydrogen-Resistant Pipelines**: Explore surface treatments (coatings, nitriding), alloy design modifications, and operational controls (CP potential optimization, hydrogen partial pressure limits) to enhance resistance to HE.

By addressing these objectives, research seeks to provide a scientifically robust foundation for the design, operation, and life extension of hydrogen-exposed subsea pipelines.

Modelling hydrogen embrittlement in subsea pipelines is a formidable challenge due to the multiphysics nature of the problem, involving electrochemical reactions, hydrogen diffusion, mechanical stress, and material microstructure. Existing approaches can be broadly categorized into:

- Empirical and Phenomenological Models

Early HE models were largely empirical, correlating hydrogen concentration with mechanical properties such as reduction in area (RA) or threshold stress intensity factor (K_{th}). The Oriani's equilibrium theory and Troiano's critical hydrogen concentration concept laid the groundwork for understanding hydrogen trapping. However, these models lack predictive capability for complex loading and environmental conditions.

- Coupled Diffusion-Mechanics Models

Modern frameworks incorporate Fickian diffusion coupled with elastoplastic stress analysis. Sofronis and McMeeking (1989) pioneered the coupled deformation-diffusion theory, which accounts for stress-driven hydrogen redistribution. This approach has been extended to include hydrogen trapping at dislocations and grain boundaries, but it often relies on simplified boundary conditions that do not fully capture subsea operational scenarios.

- Fracture Mechanics-Based Approaches

Linear elastic fracture mechanics (LEFM) and cohesive zone models (CZMs) have been applied to predict hydrogen-assisted crack growth. The J-integral approach modified for hydrogen effects (e.g., Gangloff, 2003) provides a useful tool for assessing crack propagation under static and cyclic loading. However, these models typically assume uniform hydrogen distributions, neglecting local microstructural heterogeneities.

- Multiscale and Machine Learning Approaches

Recent advances in atomistic simulations and crystal plasticity finite element models (CPFEM) offer insights into hydrogen-dislocation interactions. Machine learning techniques are also being explored to predict HE susceptibility based on material composition and processing history. However, these methods require extensive computational resources and validation against experimental data.

Despite these advancements, key limitations persist:

- Lack of integration between electrochemical and mechanical models (e.g., the role of cathodic protection in hydrogen ingress is often oversimplified).
- Insufficient treatment of cyclic loading effects, particularly for pipelines subjected to fluctuating pressures.
- Limited validation under subsea conditions, where synergistic effects of corrosion, hydrogen charging, and mechanical stress dominate.

1.4 Specific Scope and Research Objectives

In details this PhD research focuses on developing a robust numerical framework using finite element analysis (FEA) to model hydrogen embrittlement, with particular emphasis on three key aspects:

1. the integration of cohesive zone models (CZMs) to simulate hydrogen-assisted crack initiation and propagation in presence of hydrogen,
2. the dynamic evolution of hydrogen surface coverage and its influence on fracture, and
3. the explicit incorporation of hydrogen trapping effects in the diffusion-fracture coupling.

While previous studies have addressed some of these aspects independently, this work seeks to unify them into a comprehensive modelling approach that captures the synergistic effects of hydrogen transport, trapping, and material degradation.

- Cohesive Zone Modelling of Hydrogen-Assisted Fracture

Cohesive zone modelling has been widely adopted to simulate fracture processes in ductile and brittle materials by introducing a traction-separation law along potential crack paths. In the

context of HE, the cohesive zone approach must account for hydrogen's weakening effect on atomic bonds, as postulated by the HEDE mechanism. Several studies (Serebrinsky et al., 2004; Olden et al., 2008) have incorporated hydrogen-dependent cohesive laws, where the critical separation energy decreases with increasing hydrogen concentration. However, many existing models assume a quasi-static hydrogen distribution, neglecting the dynamic redistribution of hydrogen during crack propagation.

This research advances prior work by implementing a fully coupled diffusion-cohesive framework, where hydrogen diffusion is solved concurrently with mechanical equilibrium, allowing hydrogen to accumulate at the crack tip as the fracture progresses. The model accounts for stress-driven hydrogen transport, as described by Sofronis and McMeeking (1989), where hydrostatic stress gradients influence hydrogen migration towards regions of high triaxiality. Additionally, the cohesive law is modified to reflect the local hydrogen concentration at the crack tip, providing a more realistic representation of hydrogen's role in reducing fracture resistance. This approach builds upon the foundational work of Martínez-Pañeda et al. (2016), who demonstrated the importance of coupling hydrogen diffusion with cohesive failure but extends it to include dynamic hydrogen coverage effects, which have been largely overlooked in previous studies.

- Dynamic Hydrogen Coverage and Its Mechanical Implications

A significant novelty of this research lies in the explicit modelling of hydrogen surface coverage and its transient evolution during crack propagation. Hydrogen adsorption on newly formed fracture surfaces can further accelerate embrittlement by reducing the surface energy required for crack growth, as suggested by the Gibbs adsorption isotherm (Lynch, 1988). While some numerical studies (e.g., Díaz et al., 2016) have considered constant hydrogen coverage, real fracture scenarios involve dynamically changing surfaces where hydrogen adsorption and desorption occur as the crack advances.

To address this gap, the present work introduces a time-dependent hydrogen coverage model integrated within the cohesive zone framework. The adsorption kinetics are governed by the local hydrogen concentration, temperature, and surface energy, following the Langmuir-McLean isotherm (Oriani, 1970). This allows the model to capture scenarios where hydrogen coverage varies along the crack flanks, influencing both the cohesive strength and the rate of crack propagation. The implementation is validated against experimental observations of delayed fracture in notched specimens, where hydrogen coverage plays a decisive role in the transition from slow crack growth to catastrophic failure.

- Incorporation of Hydrogen Trapping in the Diffusion-Fracture Coupling

A critical limitation of many existing HE models is the treatment of hydrogen trapping as a secondary effect, often simplified through effective diffusion coefficients. However, experimental studies (e.g., Turnbull et al., 1989) have demonstrated that microstructural traps—such as dislocations, grain boundaries, and precipitates—significantly alter hydrogen

distribution and availability for embrittlement. Neglecting trapping effects can lead to substantial inaccuracies in predicting hydrogen accumulation at critical locations.

This research advances the state of the art by explicitly incorporating trap dynamics into the coupled diffusion-mechanical model. The formulation distinguishes between reversible (e.g., dislocations) and irreversible traps (e.g., carbides), following the McNabb-Foster kinetics (1963). The trapping model is coupled with the cohesive zone framework such that trapped hydrogen influences both the local hydrogen availability for embrittlement and the mechanical response of the material. This approach provides a more realistic representation of hydrogen transport in complex microstructures, bridging the gap between continuum-scale simulations and atomistic descriptions of trapping (Jothi et al., 2015).

- Integration with Experimental Validation

To ensure the physical relevance of the numerical model, the research incorporates validation against experimental. The model's predictive capabilities are assessed by comparing simulated crack growth rates, fracture toughness reduction, and hydrogen distribution patterns with experimental measurements.

- Broader Contributions and Future Directions

By unifying cohesive zone modelling, dynamic hydrogen coverage, and explicit trapping effects, this research provides a more holistic numerical framework for HE assessment. The developed methodology is not restricted to a specific material system but is adaptable to various high-strength alloys, enabling its application in industrial failure analysis and lifetime prediction. Future extensions could explore multi-scale approaches, linking the current continuum model with atomistic or crystal plasticity simulations to further refine the understanding of hydrogen-dislocation interactions.

In summary, this PhD research advances the numerical modelling of hydrogen embrittlement by addressing key limitations in existing approaches, offering new insights into the interplay between hydrogen transport, trapping, and fracture. The developed framework serves as a valuable tool for both academia and industry, contributing to the safer design of hydrogen-exposed components.

1.5 Summary

This introduction has outlined the critical challenges posed by hydrogen embrittlement in subsea pipelines for example, emphasizing the need for advanced predictive models and material solutions. The increasing use of hydrogen as an energy carrier necessitates a fundamental reassessment of pipeline integrity management strategies.

The remainder of this thesis is structured as follows:

- Chapter 2 | Literature Review and Modelling Approach: reviews the state-of-the-art in hydrogen embrittlement mechanisms and experimental methodology, material susceptibility and characterization, and existing modelling approaches.

- Chapter 3 | Validation/Test Case: details the development of a testing case where the methodology described in Chapter is implemented.

- Chapter 4 | Model with Effect of Elasticity: presents the comparison of experimental results and developed modelling technique without the contribution of plastic component,

- Chapter 5 | Model with Effect of Plasticity: presents the comparison of experimental results and developed modelling technique with the contribution of plastic component to the mechanical part only.

- Chapter 6 | Model with Lattice and Trapping Component: presents the comparison of experimental results and developed modelling technique with the contribution of plastic component.

- Chapter 7 | Conclusions: presents the difficulties, achievements, conclusions and any potential future works.

By bridging the gap between fundamental science and engineering practice, this research aims to enhance the safety and reliability of subsea pipelines in the emerging hydrogen economy.

2 Literature Review and Numerical Modelling Approach

2.1 Introduction to the Literature Review

Current and future hydrogen-based energy systems require the production, transport, storage, and use of gaseous hydrogen, often operating at high pressures above 100 MPa. The safety and durability of these systems are seriously compromised by material degradation in the presence of hydrogen.

Hydrogen embrittlement is a phenomenon that, due to its relevance in industry and many engineering applications, has driven extensive research efforts by the scientific community for over a century. However, the work carried out by scientists has not been sufficiently translated into engineering practice.

One of the major challenges of our time is to shift the debate from the mechanisms responsible for hydrogen-induced damage to the development of quantitative predictive models. To improve their predictive capability, incorporating the effect of plastic strain gradients in the numerical modelling of hydrogen embrittlement appears unavoidable, given experimental results. Additionally, it is necessary to consider the effect of plastic strain gradients not only in cracks but also in notch-like defects that arise in materials during manufacturing and service.

This section provides a comprehensive literature review of the mechanisms responsible for hydrogen-assisted cracking in both cracks and notches, recent advances in predictive numerical models based on cohesive zone formulations, and nonlocal plasticity theories incorporating strain gradients.

2.2 Hydrogen-assisted cracking

Hydrogen embrittlement is a physicochemical-metallurgical phenomenon that leads to a reduction in ductility and toughness in metals and alloys, compromising the structural integrity of components, materials, and structures.

Hydrogen embrittlement was first identified by Johnson [2], who observed that exposure of iron and steel to hydrogen and acidic environments produced significant changes in mechanical behaviour, particularly a reduction in ductility and overall degradation of material performance. This early experimental work involved exposing metallic specimens to hydrogen-generating conditions and assessing the resulting changes in mechanical response, thereby establishing the foundational evidence that hydrogen can adversely affect steel integrity. Building on this initial observation, later experimental studies have focused extensively on ultrahigh-strength steels such as AERMET 100. Thomas et al. [3] investigated internal hydrogen embrittlement in this

material by hydrogen charging specimens using electrochemical or gaseous methods, followed by mechanical testing to compare the behaviour of hydrogen-charged and uncharged samples. Their results demonstrated a marked reduction in fracture resistance due to hydrogen uptake. In a related study, Li et al. [4] examined hydrogen trapping mechanisms in the same steel using thermal desorption analysis combined with microstructural characterization techniques, identifying a range of reversible and irreversible trap sites associated with defects, dislocations, and microstructural interfaces. Complementary work by Ayer and Machmeier [5] employed transmission electron microscopy to characterise the microstructure of AERMET 100, linking dislocation structures and precipitation phenomena to the observed strengthening and providing essential insight into the microstructural features that govern susceptibility to hydrogen damage.

Further research has also explored mitigation strategies, such as the application of sacrificial coatings. Figueroa and Robinson [6] investigated the influence of such coatings on hydrogen embrittlement and re-embrittlement behaviour by exposing coated high-strength steels to corrosive environments and evaluating their mechanical performance and hydrogen uptake. Their findings indicated that while coatings can reduce hydrogen ingress, they may not fully prevent embrittlement under all service conditions. In parallel with experimental developments, significant progress has been made in numerical modelling of hydrogen-assisted cracking. Serebrinsky et al. [7]developed a continuum-scale model informed by quantum-mechanical insights, incorporating hydrogen diffusion, stress-assisted transport, and fracture criteria to bridge atomistic behaviour and macroscopic cracking response. Similarly, Martínez-Paneda et al. [8] proposed a strain gradient plasticity-based framework that enhances the representation of stress localisation near crack tips, coupling mechanical deformation with hydrogen diffusion and trapping to more accurately predict crack initiation and propagation under hydrogen exposure. Finally, the engineering relevance of these phenomena has been demonstrated in practical applications, where Sánchez et al. [9] measured hydrogen content in high-strength steels and correlated it with embrittlement and premature failure, confirming hydrogen-assisted cracking as a critical limitation in structural applications of high-strength steels.

2.2.1 Responsible Mechanisms for hydrogen-assisted cracking

In metals (especially steels), hydrogen traps are microstructural features that can capture and hold hydrogen atoms as they diffuse through the lattice. This is central to understanding Hydrogen embrittlement, where trapped hydrogen reduces ductility and can promote cracking.

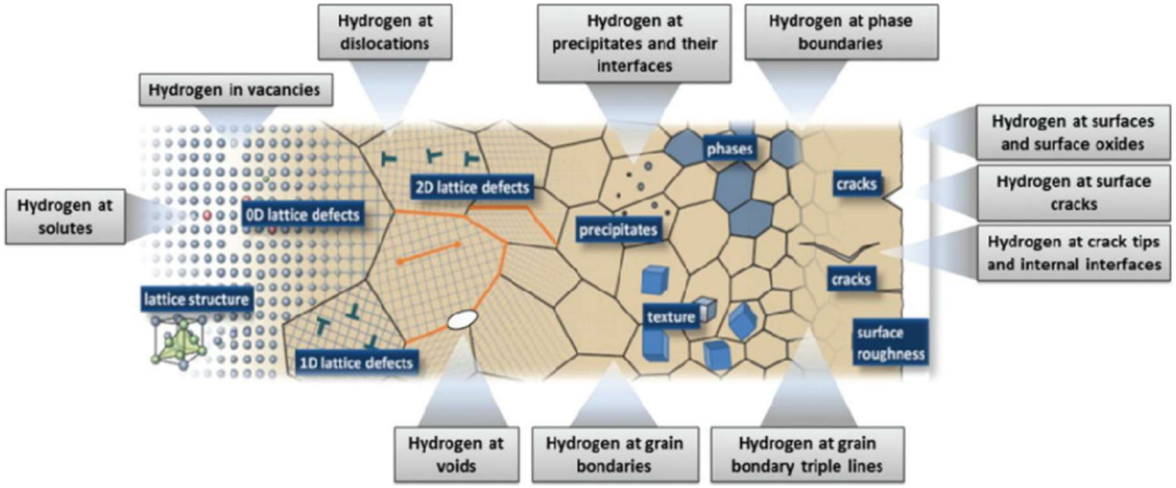

Figure 2-1: Figure Hydrogen Traps [10]

Although there is some controversy regarding the atomistic mechanisms involved in hydrogen embrittlement, there is a certain consensus based on experimental observations about the two basic mechanisms responsible for hydrogen-assisted cracking:

Hydrogen-enhanced decohesion (HEDE): Where interstitial, adsorbed, or grain-boundary-segregated hydrogen weakens interatomic bonds, reducing the cohesive energy of the metal's crystal lattice and thus the energy required for fracture (Figure 2-3) [11].

Hydrogen-enhanced localized plasticity (HELP): Where hydrogen induces localized plastic deformation.

Hydrogen Embrittlement by Decohesion (HEDE), Hydrogen Enhanced Localized Plasticity (HELP), and Adsorption Induced Dislocation Emission (AIDE) differ primarily in how hydrogen interacts with the lattice and affects fracture behaviour. HEDE assumes hydrogen reduces the cohesive strength between atoms, making crack propagation easier through brittle cleavage. In contrast, HELP proposes that hydrogen increases dislocation mobility, leading to highly localized plastic deformation that concentrates strain and accelerates crack growth. AIDE sits somewhat between these ideas: hydrogen adsorbed at crack tips reduces the energy barrier for dislocation emission from the crack surface, promoting plasticity directly at the crack tip and facilitating crack advance. In short, HEDE emphasizes weakened atomic bonds, HELP focuses on enhanced dislocation motion, and AIDE describes hydrogen-assisted dislocation emission at crack fronts.

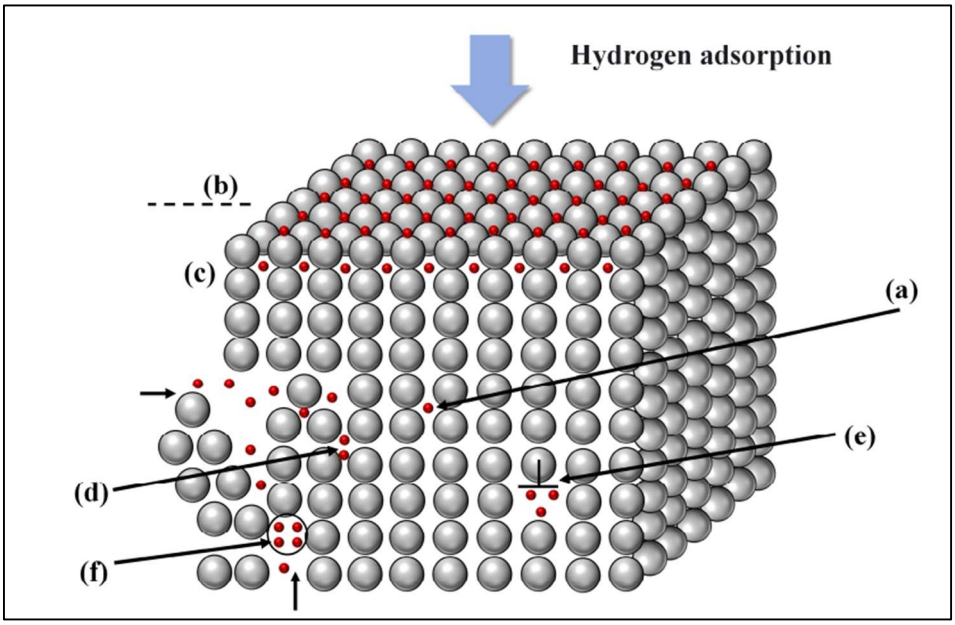

Figure 2-2: Hydrogen traps in the steels: (a) interstitial sites; (b) surface traps; (c) subsurface traps; (d) grain boundary traps; (e) dislocation traps; (f) vacancy traps, from [12].

The Hydrogen-Enhanced Decohesion (HEDE) mechanism is one of the key explanations for Hydrogen embrittlement. It describes how hydrogen reduces the cohesive strength of a solid—especially along interfaces such as grain boundaries—making cracking easier under stress.

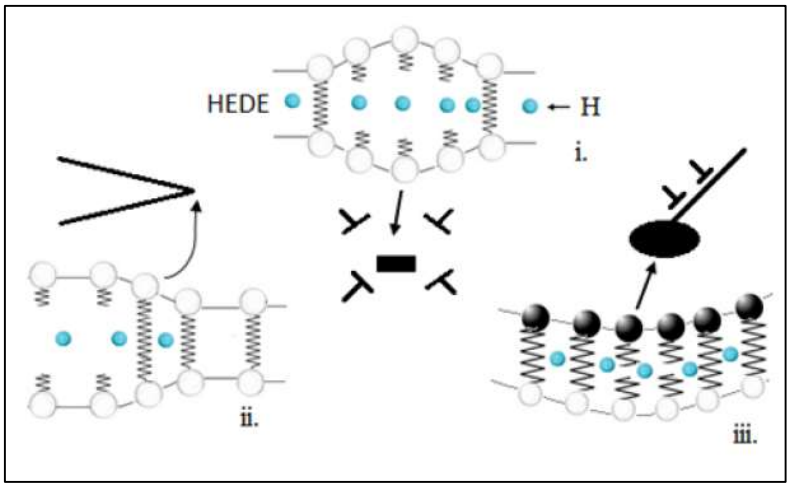

Figure 2-3: Schematic diagram of the HEDE mechanism illustrating the weakening of cohesive strength caused by: (i) interstitial hydrogen, (ii) adsorbed hydrogen, (iii) hydrogen segregated at grain boundaries. Adapted from [[11] and [13]].

At its core, HEDE proposes that hydrogen weakens atomic bonding, lowering the stress required for fracture at specific microstructural sites.

(i) Interstitial hydrogen (inside the lattice):

- Hydrogen atoms occupy interstitial sites between metal atoms.
- They distort the lattice and weaken metallic bonds locally.
- This reduces the energy needed to separate atoms under stress.
- Effect: bulk softening + reduced cohesive strength ahead of cracks
- Think of it as “loosening the atomic spring network” inside the material.

(ii) Adsorbed hydrogen (surface hydrogen):

- Hydrogen accumulates on free surfaces or crack tips.
- It weakens surface atomic bonds directly at the crack front.
- This reduces surface energy (γ), making crack propagation easier.
- Effect: cracks can advance more easily once formed
- This is especially important at freshly created crack surfaces.

(iii) Hydrogen segregated at grain boundaries

- Hydrogen migrates and concentrates at grain boundaries (GBs).
- Grain boundaries are already weaker than the bulk lattice.
- Hydrogen further reduces cohesive strength between grains.
- Effect: intergranular fracture (cracks propagate along GBs)
- This is often the most damaging case in HEDE.

Putting it together (what HEDE predicts), HEDE says fracture occurs when: atomic bonding strength decrease (due to presence of hydrogen) and especially at stress-concentrated regions (crack tips, grain boundaries). So instead of plastic deformation, the material fails by cleavage or intergranular cracking and often with very little warning deformation

The following figures schematically show the main experimental and numerical achievements (respectively) that have led to the acceptance of the HEDE theory by the international scientific community:

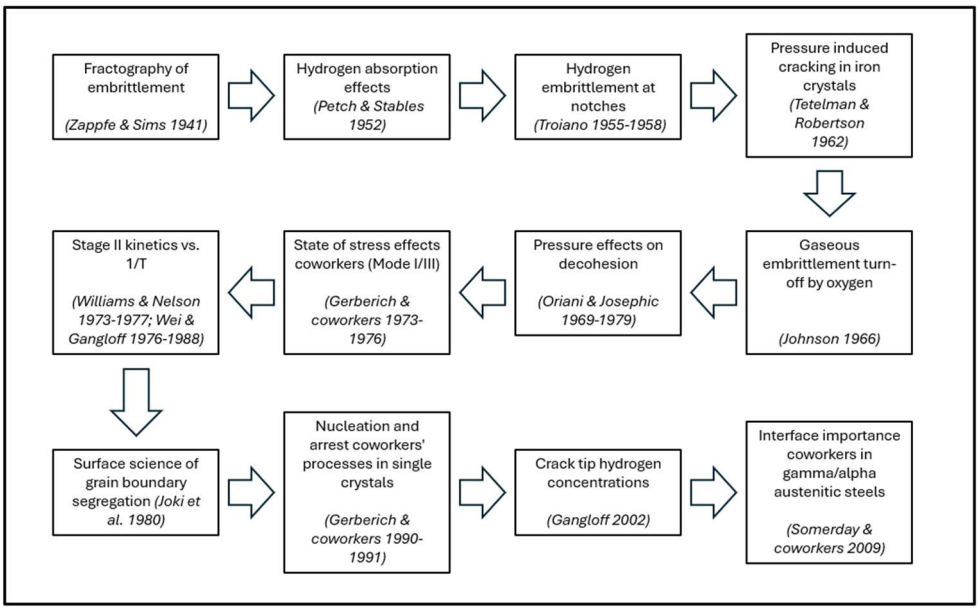

Figure 2-4: Experimental milestones (de-cohesive models) Adapted from [14]

The development of Hydrogen-Enhanced Decohesion (HEDE) theory for hydrogen embrittlement evolved over several decades through a progressive refinement of ideas linking hydrogen presence to reduced atomic cohesion and brittle fracture, beginning with early qualitative observations and culminating in modern mechanistic and engineering frameworks. Zappfe & Sims [13] are often credited with one of the earliest conceptual foundations, proposing that hydrogen could weaken interatomic bonds at crack tips, thereby lowering the cohesive strength required for fracture in metals, especially under tensile stress. Building on this, Petch & Stables related hydrogen-assisted failure to microstructural features such as grain boundaries and cleavage planes, emphasizing how localized weakening could promote intergranular or brittle fracture modes. Troiano [15] advanced the field significantly by integrating hydrogen effects into stress-assisted diffusion concepts, proposing that hydrogen migrates toward regions of high triaxial stress, particularly crack tips, where it reduces cohesive strength and facilitates crack propagation, effectively formalizing early versions of the decohesion hypothesis. Tetelman & Robertson [16] further developed this into a more explicit HEDE framework by connecting hydrogen accumulation at crack tips with fracture mechanics concepts, particularly stress intensity, thereby linking microscopic hydrogen effects with macroscopic crack growth behaviour. Johnson [17] contributed by incorporating fracture mechanics rigor into hydrogen embrittlement analysis, helping to quantify conditions under which hydrogen-assisted cracking becomes energetically favourable. A major theoretical leap was provided by Oriani & Josephic [18], who developed the influential Oriani trapping model, describing reversible and irreversible hydrogen traps in metals and establishing how trapping controls hydrogen transport, local concentration, and thus embrittlement susceptibility at crack tips. During the 1970s, Gerberich & coworkers [19] expanded the HEDE concept by

emphasizing microstructural stress concentrations, dislocation interactions, and localized decohesion processes, showing that hydrogen can significantly reduce cohesive strength at microvoids and grain boundaries under plastic deformation. In parallel, Williams & Nelson (1973–1977) [20] and Wei & Gangloff [21] advanced fracture mechanics-based interpretations of hydrogen-assisted cracking, establishing critical thresholds for stress intensity (K_ISCC) and emphasizing the kinetics of hydrogen-assisted subcritical crack growth in structural alloys exposed to hydrogen or hydrogen-producing environments. Joki et al. (1980) contributed to the understanding of environmental and loading-rate effects on hydrogen embrittlement, helping to clarify time-dependent aspects of crack initiation and propagation under hydrogen exposure. Later, Gerberich & coworkers(1990–1991) [22] refined the HEDE mechanism further using more advanced microstructural and atomistic perspectives, reinforcing the idea that hydrogen reduces cohesive strength directly at crack tips and grain boundaries, often in synergy with localized plasticity and stress concentration.

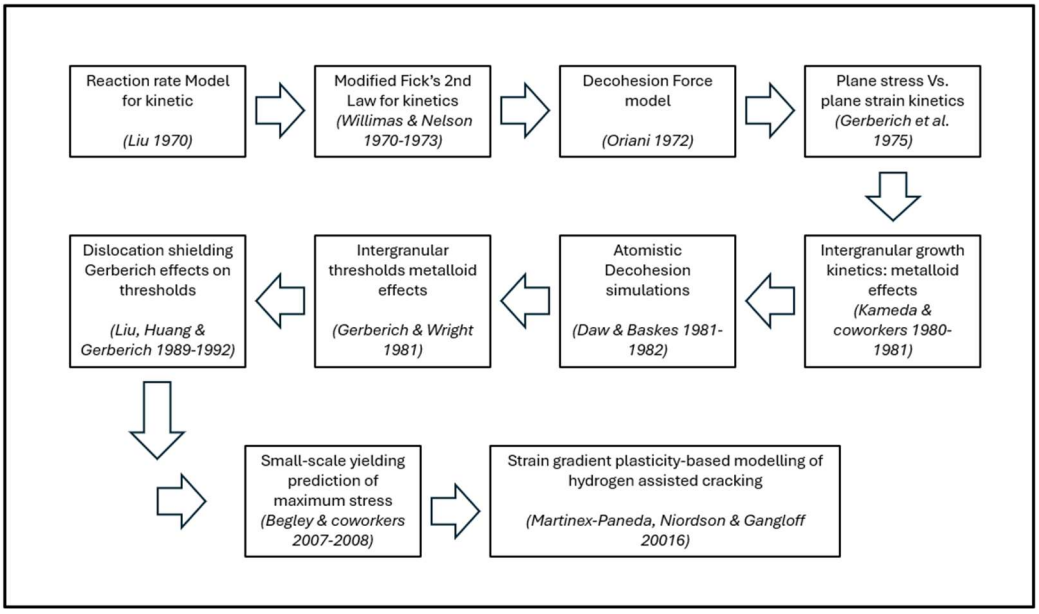

Figure 2-5: Numerical Analysis milestones (de-cohesive models) Adapted from [18]

The historical sequence of the Numerical Analysis to characterise the de-cohesive models can be listed as per below:

- In the early 1980s, Gerberich and Wright [22] developed a model to determine the stress intensity factor threshold in the presence of hydrogen.
- During the 1980s and 1990s, Huang and Gerberich [23] analysed the effects of dislocations on the stress intensity factor threshold in the presence of hydrogen.

- In the 1990s, Daw and Baskes [24] and Foiles et al. [25] conducted atomistic simulations using the embedded atom method, demonstrating that hydrogen could cause a reduction in the cohesive energy at nickel grain boundaries.
- Finally in the 2000s, considering that a high stress level and high hydrogen concentrations are required to break interatomic bonds, Gangloff et al. [26], [27] showed that plastic strain gradients could account for the high stress levels near the crack tip.

Meanwhile, the HELP mechanism (Hydrogen-Enhanced Localized Plasticity) studies the interaction between hydrogen and plasticity [11] (Figure 2-6). Beachem (in 1972), based on fractographic observations, was the first to suggest that solute hydrogen facilitated dislocation movement [28]. Starting in the 1980s, Birnbaum et al. [29], relying on experimental observations via transmission electron microscopy, proposed the HELP mechanism as responsible for the increase in dislocation velocities due to hydrogen presence in the material. Since then, numerous experimental studies have sought to identify the mechanisms related to hydrogen-induced localized plasticity (Figure 2-7).

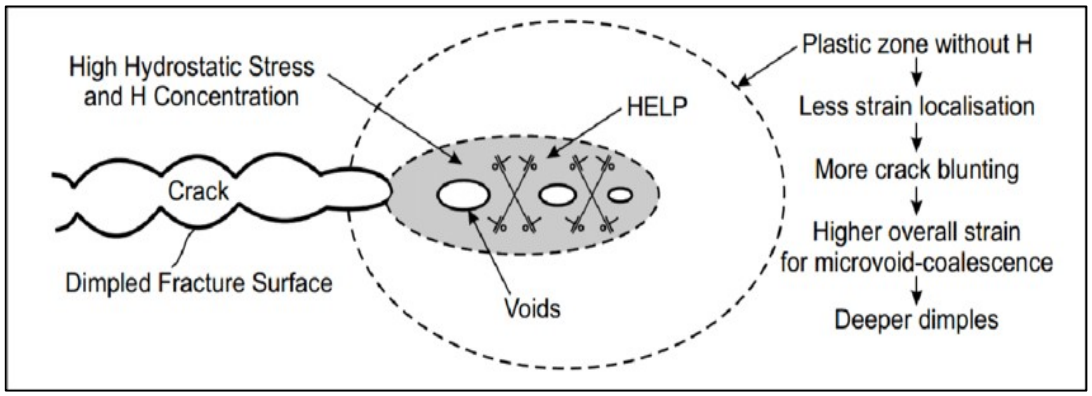

Figure 2-6: Schematic diagram of the HELP mechanism with the process of microvoid coalescence, localized and facilitated plasticity in regions with high hydrogen concentrations [30]

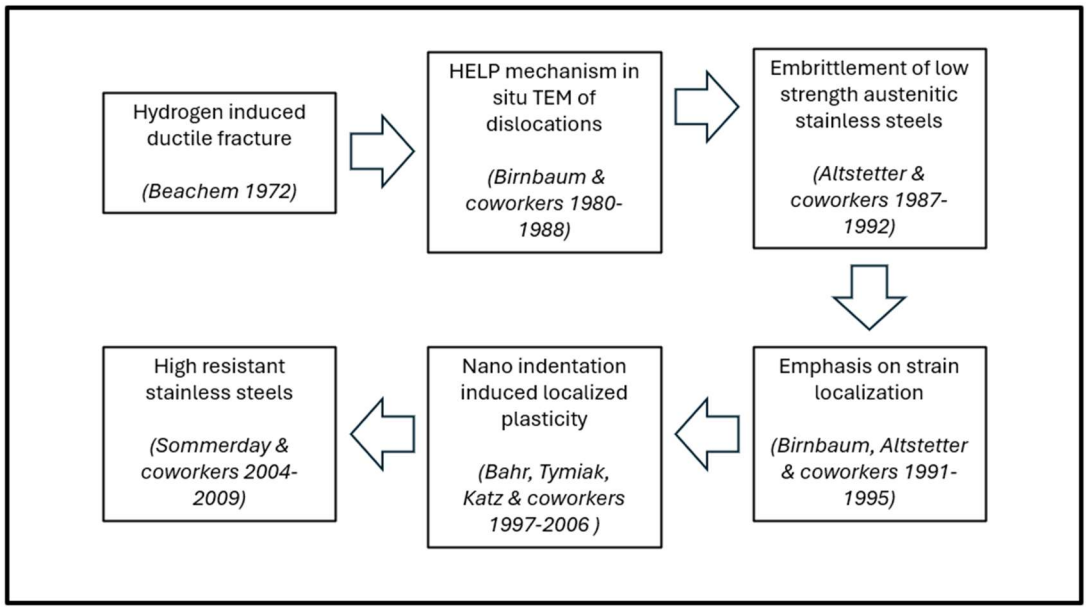

Figure 2-7: Experimental milestones (HELP models) Adapted from [18]

In the 1970s, Tetelman [31] analysed the effect of hydrogen pressure on the nucleation and growth of microvoids and their relationship with ductile fracture. Despite numerous contributions (Figure 2-8), the theoretical foundations for the HELP theory were established in the 2000s. The atomistic simulations carried out by Kaxiras et al. [32] and the numerical modelling of the HELP mechanism performed by Sofronis et al. facilitated the study of hydrogen-assisted embrittlement.

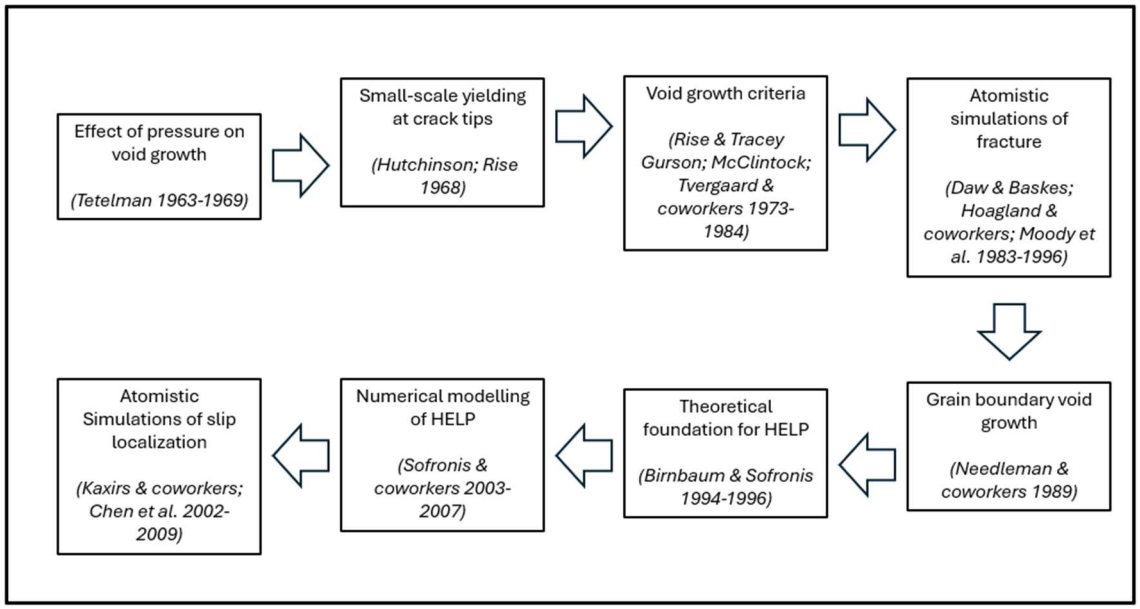

Figure 2-8: Theoretical Analysis milestones (HELP models) Adapted from [18]

There is growing consensus that hydrogen-enhanced atomic decohesion is the dominant mechanism for internal hydrogen-assisted cracking (IHAC) and hydrogen environment-assisted cracking (HEAC) in high-strength alloys [33]. Beachem [28] and Birnbaum et al. [34] found evidence that the hydrogen-induced local plasticity model was the dominant mechanism in austenitic stainless steels and responsible for their low corrosion resistance. Novak, Yuan, Somerday, Sofronis, and Ritchie have suggested that hydrogen embrittlement involves a combination of both mechanisms [35].

2.2.2 Model to characterize hydrogen transportation

After reviewing the main atomistic mechanisms involved in hydrogen embrittlement, we proceed to examine hydrogen transport models. To predict the degradation of a material's mechanical properties, it is essential to accurately assess how hydrogen is distributed within the material.

Atomic hydrogen can occupy interstitial sites in the lattice (NILS, Normal Interstitial Lattice Sites) or accumulate in various microstructural heterogeneities such as dislocations, grain boundaries, inclusions, voids, defects like impurity atoms, or surfaces—all described as hydrogen traps [35]. Among the theoretical advances in capturing the effect of traps on hydrogen transport are the pioneering models proposed by McNabb and Foster [36] and Oriani [37]. Oriani's theory assumes a local equilibrium between hydrogen in reversible traps and hydrogen in the lattice, under the assumption that trap occupation kinetics are very fast [37].

The trap's ability to capture hydrogen is related to its binding energy (E_B), which can be experimentally determined for a specific microstructure using chemical permeation [41] or thermal desorption spectrometry ([38], [39]). Given the wide variety of hydrogen traps, they have been classified based on reversibility to simplify their effects [40]. Traps with binding energies above 60–70 kJ/mol are typically considered irreversible in steel [37]. The high binding energy (E_B) means irreversible traps do not readily release hydrogen [41], suggesting they have no direct impact on hydrogen diffusion.

Although there is a wide variety of traps, it appears that hydrogen traps associated with dislocations play a predominant role in intergranular hydrogen fracture [42]. The density of hydrogen traps due to dislocations depends on the local plastic deformation. To relate the number of traps per unit volume (N_T) to the plastic strain (ε_p), Kumnick and Johnson [43] proposed a phenomenological relationship in accordance with experimental results obtained through permeation tests for iron in a gaseous hydrogen atmosphere, given by:

$$log_{10}N_T = 23.26 - 2.33\exp(-5.5\varepsilon_p) \quad (1)$$

In addition to the empirical relationships obtained from experimental tests, it is possible to determine (N_T) by relating it to dislocation density. Sofronis et al. [44], while maintaining consistency with the experimental results of Thomas [45], correlated the dislocation density (ρ), with the trap density (N_T) as follows:

$$N_T = \sqrt{2} \cdot \frac{\bar{\rho}}{\bar{a}}, \quad (2)$$

where a is the lattice parameter. The dislocation density is considered to vary linearly with the equivalent plastic strain according to:

$$\bar{\rho} = \begin{cases} \bar{\rho}_0 + \gamma\varepsilon_p & for\ \ \varepsilon_p < 0.5 \\ \bar{\rho}_1 & for\ \ \varepsilon_p \geq 0.5' \end{cases} \quad (3)$$

where $\bar{\rho}_0 = 1 \times \frac{10^{10}m}{m^3}$ is the dislocation density for annealed material, $\bar{\rho}_1 = 1 \times \frac{10^{16}m}{m^3}$ is the maximum dislocation density, and $\gamma = 2 \times \frac{10^{16}m}{m^3}$.

The figure compares the different models for the case of uniaxial tension. The same conditions as in the experiments by Kummick and Johnson [43] are assumed. The dislocation density in hydrogen traps in the model by Sofronis et al. ([44], [46]) is noticeably higher than that obtained by Kummick and Johnson [43].

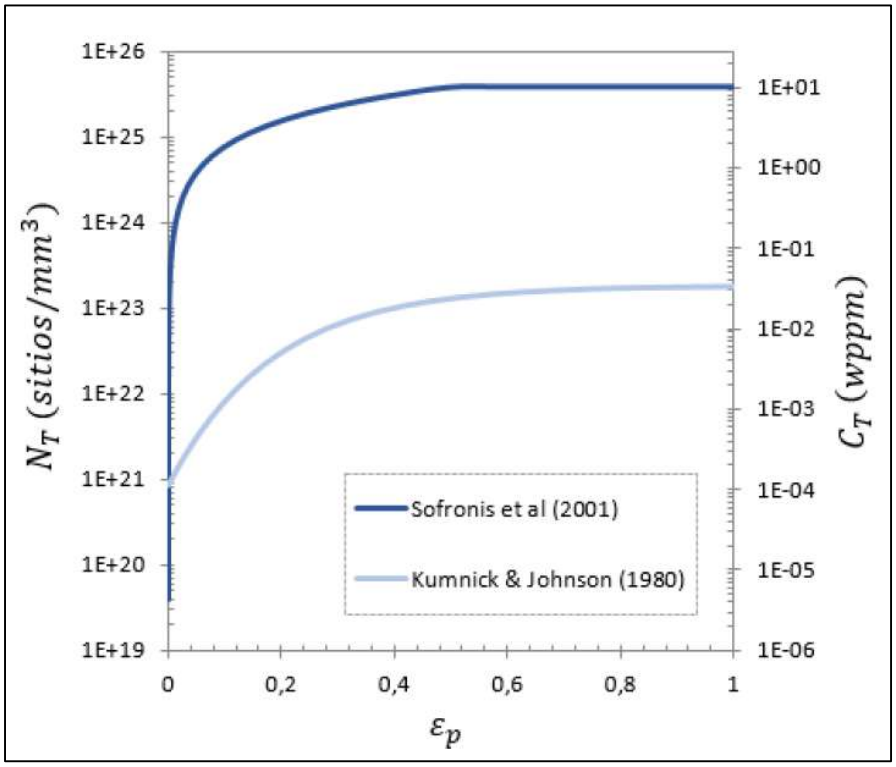

Figure 2-9: Graphical representation of trap densities and hydrogen concentration in the traps according to the work of Kumnick and Johnson [46] and the model by Sofronis et al. [47, 49].

2.2.3 Introduction to Numerical Models to characterize hydrogen diffusion

The equation governing hydrogen diffusion is Fick's law. In terms of chemical potential, Li et al. [47] analysed the influence of hydrostatic stress and thus the fact that Fick's first law is insufficient to describe diffusion flux. Willian and Nelson [20] and Van Leeuwen [38] modelled crack growth kinetics based on a modified second Fick's law. More recently, Sun et al. [48] and Gao et al. [49] found evidence of hydrostatic stress influencing hydrogen distribution near the crack tip.

According to the mass conservation law and following the equilibrium conditions proposed by Oriani [18], Sofronis and McMeeking developed a pioneering model for hydrogen transport under large deformations, assuming a constant hydrogen concentration at the boundary conditions. They modelled the competition between hydrogen trap-induced deformation (due to dislocations) and hydrostatic stress in hydrogen distribution near the crack tip [50]. This model was later modified to include the effects of additional factors.

For instance, Krom et al. [51] incorporated trap dynamics by adding a third term to account for strain rate effects; Turnbull et al. [52] developed a mathematical model based on high trap occupancy, addressing equation nonlinearity; and Novak et al. [35] coupled Sofronis and

McMeeking's model with Krom's modified version, assuming hydrogen embrittlement is linked to dislocation motion.

Recently, Di Leo and Anand [53] established that hydrogen concentration at boundary conditions is not constant. Instead, imposing a constant chemical potential is more appropriate, as lattice hydrogen concentration also depends on hydrostatic stress. This approach is particularly relevant for numerical models incorporating plastic strain gradient theories.

Numerical simulations based on conventional plasticity theory predict crack-tip stresses of only 3 – 5 times σ_0, leading to moderate hydrogen concentrations that seem insufficient to justify brittle fracture in the presence of plastic deformation – since bond breaking would presumably require much higher stresses ($\sim 10\sigma_0$). Experimentally, numerous micro-scale tests ([54], [55] and [56]) have demonstrated the importance of geometrically necessary dislocations (GNDs) and their contribution to hardening, even with small amounts of hydrogen. Consequently, there is growing consensus on incorporating size effects in hydrogen-assisted fracture modelling using strain gradient plasticity (SGP) theories in numerical simulations [3]. There is also a need to better define conditions within 0.1–5μm of the crack tip, where dislocations, chemistry, and microstructure dominate material behaviour [57].

The most up-to-date numerical models for hydrogen embrittlement include:

- Multiple trap types [58];
- Hydrogen's effect on trap density and dislocation velocity as an additional transport mechanism toward the crack tip [59];
- The influence of GNDs on predicting the threshold stress intensity factor (K_{th}) and subcritical crack growth rates in hydrogen-containing corrosive environments [8].

Numerical studies on hydrogen-assisted cracking often employ cohesive zone models (see [60]). Particularly notable are hydrogen-dependent cohesive zone formulations under the HEDE (Hydrogen-Enhanced Decohesion) mechanism, proposed by Serebrinsky et al. [7], Scheider et al. [14], and Álvaro et al. [61]. For crack initiation and fatigue propagation, the work of Gilbert Hénaff et al. [62] stands out.

2.3 Numerical Modeling approach

In the study of mass transport phenomena, a well-established analogy exists between hydrogen diffusion in solids and thermal diffusion (heat conduction). This analogy is not merely conceptual but extends to the mathematical and computational treatment of both processes. At their core, both hydrogen diffusion and heat conduction are governed by similar

types of partial differential equations that describe how a quantity – whether hydrogen concentration or temperature – changes in space and time.

Because of this similarity, many of the numerical techniques originally developed for heat transfer problems can be directly applied to the modelling of hydrogen diffusion. Finite difference, finite volume, and finite element methods, for example, are equally suited to simulate both phenomena. These methods rely on discretizing the problem domain and solving the governing equations over time, making use of similar boundary and initial conditions. For instance, a fixed surface concentration in hydrogen diffusion mirrors a fixed surface temperature in thermal conduction, and a constant hydrogen flux resembles a constant heat flux.

This modelling analogy provides an efficient and robust framework, particularly in engineering applications where software like ABAQUS developed for thermal analysis can be adapted for hydrogen transport simulations. However, the analogy is not exact. Hydrogen diffusion often involves additional complexities such as trapping, concentration-dependent diffusivity, and interactions with microstructural defects or chemical species. These phenomena require modifications to the base model or the inclusion of supplementary equations, which have no direct equivalent in thermal diffusion.

Nevertheless, the analogy remains a valuable tool in simplifying the conceptual understanding and numerical modelling of hydrogen behaviour in materials. It provides a foundation upon which more advanced, material-specific models can be constructed, ultimately aiding in the design of safer and more efficient hydrogen-based systems.

2.4 Heat Transfer Analogy (with ABAQUS Software)

Numerical modelling of mechanical problems in presence of hydrogen diffusion environment is achieved utilising the analogy with heat transfer equations. In particular, fully coupled implementation relies on the analogy between heat transfer and mass diffusion equations.

The hydrogen content continuity equation can be written as:

$$\frac{\partial C}{\partial t} + \nabla \cdot J_m = S \tag{4}$$

where:

- C: is the total hydrogen concentration;
- J_m: is the hydrogen flux;
- S: is the hydrogen source term.

The Source of hydrogen can be linked for example to subsea pipeline exposed to presence of seawater, transported hydrogen or a combination of both

Similarly, the continuity equation for heat transfer implemented in ABAQUS reads:

$$\rho \frac{\partial U_q}{\partial t} + \nabla \cdot J_q + r_q = 0 \quad (5)$$

where:

- ρ: is the mass density;
- U_q: is the internal thermal energy per unit mass;
- J_q: is the heat flux;
- r_q: is the heat source;

Considering for simplicity the mass density $\rho = 1$, the first basic set of analogies can be established as per following: $U_q \equiv C$ (6), $J_q \equiv J_m$ (7) and $r_q \equiv S$ (8)

To further progress our modelling in ABAQUS, it is now necessary to find an expression for total concentration of hydrogen C and the mass flux J_m to be implemented.

2.4.1 Numerical Formulation for the Hydrogen Concentration

As mentioned in previous studies [63], the total hydrogen concentration C, includes two contributions: the diffusible hydrogen, C_L, and the trapped hydrogen, C_T: $C = C_L + C_T$ (9).

According to the Oriani Theory [18], the trapped hydrogen concentration, C_T, can be written (please also refer to Section 6.1.3) as a function of the diffusible concentration, C_L, as:

$$C_T = \frac{N_T K_T C_L}{K_T C_L + N_L} \quad (10)$$

where:

N_L is the lattice site density, and for $\alpha - Fe$ based material N_L can be expressed as per [51]:

$$N_L = \frac{N_A \beta \rho}{A_r} \quad (11)$$

The Avogadro constant N_A is a fundamental physical constant representing the number of particles per mole of a substance. In this context, the number β of interstitial lattice sites per iron (Fe) atom is 6, assuming hydrogen atoms occupy the tetrahedral sites at room temperature. Additionally, ρ denotes the density of iron (7.87×103 kg/m3 at 293 K [51]), and A_r is the molar mass of Fe (55.8×10-3 kg/mol3 at 293 K) [64].

K_T is the equilibrium constant evaluated as a function of the binding enthalpy ΔW_B [18] with the following formula:

$$K_T = \exp\frac{-\Delta W_B}{RT} \tag{12}$$

where the binding enthalpy ΔW_B is set equal to -60kJ/mol in accordance to [65].

Several methods can be used to estimate the number of trapping sites N_T, including the one based on the experimental data [65].

From this [50] and [51] proposed the following exponential law, evaluating the density of dislocation trap sites from the equivalent plastic strain:

$$C_T = log_{10}N_T = 23.26 - 2.33\exp\left(-5.5\varepsilon_p\right) \tag{13}$$

Other methods include the one proposed by Sofronis [44] as:

$$N_T = \sqrt{2}\cdot\frac{\bar{\rho}}{\bar{a}}, \tag{14}$$

where $\bar{a} = 2.86 \times 10^{10}m$ is the lattice parameter of BBC iron and $\bar{\rho}$ is the density of dislocation which is a function of the equivalent plastic strain:

$$\bar{\rho} = \begin{cases} \bar{\rho}_0 + \gamma\varepsilon_p & for\ \ \varepsilon_p < 0.5 \\ \bar{\rho}_1 & for\ \ \varepsilon_p \geq 0.5' \end{cases} \tag{15}$$

where $\bar{\rho}_0 = 1 \times \frac{10^{10}m}{m^3}$ is the dislocation density for annealed material with $\varepsilon_p = 0$, $\bar{\rho}_1 = 1 \times \frac{10^{16}m}{m^3}$ is the maximum dislocation density, and $\gamma = 2 \times \frac{10^{16}m}{m^3}$.

ABAQUS has no built-in unit system and expects all numerical inputs to be dimensionally consistent. The user shall select a base system (such as SI or mm-tonne-s) and use it exclusively for all geometry, material properties, and loads. The software treats all inputs as raw numbers, meaning you are responsible for maintaining consistency to avoid errors.

Table 2-1: ABAQUS consistent units' table

Physical Quantity	SI Unit	SI (mm) Unit	US Unit
Length	Meter (m)	Millimeter (mm)	Inch (in)
Time	Second (s)	Second (s)	Second (s)
Mass	Kilogram (kg)	Ton ($tonne = 10^3 kg$)	Pound-mass (lbm)
Force	Newton (N)	Newton (N)	Pound-force (lbf)
Density	$kg \cdot m^{-3}$	$tonne \cdot mm^{-3}$	$lbf \cdot s^2 \cdot in^{-4}$
Temperature	Kelvin (K) or $^\circ C$	Kelvin (K) or $^\circ C$	Rankine ($^\circ R$) or $^\circ F$
Conductivity (k)	$W \cdot m^{-1} \cdot K^{-1}$	$mW \cdot mm^{-1} \cdot K^{-1}$	$lbf \cdot s^{-1} \cdot ^\circ F^{-1}$
Specific Heat (c_p)	$J \cdot kg^{-1} \cdot K^{-1}$	$mJ \cdot tonne^{-1} \cdot K^{-1}$	$in^2 \cdot s^{-2} \cdot ^\circ F^{-1}$
Heat Flux (q)	$W \cdot m^{-2}$	$mW \cdot mm^{-2}$	$lbf \cdot in^{-1} \cdot s^{-1}$

2.4.2 Numerical Formulation for the Hydrogen Flux

The hydrogen flux can be expressed as a vector dependent on these factors and the hydrogen flux vector can be rewritten as (please refer also to Section 6.1.4):

$$J = -D_L \nabla C_L + \frac{D_L C_L V_H}{RT} \nabla \sigma_H \tag{16}$$

where:

- D_L: is the effective diffusivity of interstitial concentration (lattice part);
- C_L: is the hydrogen concentration in lattice part;
- V_H is the partial molar volume;
- R: is the universal gas constant;
- T is the thermodynamic temperature; and
- σ_H is the hydrostatic stress.

2.4.3 Numerical Formulation – Final Consideration

By analysing (16), it can be observed that the forces driving the mass flux J are ∇C_L and $\nabla \sigma_H$. While $\nabla \sigma_H$can be obtained from coupled stress analysis (please refer to Section 6), ∇C_L has to be solved along (4). It is therefore natural to assume C_L as the primary unknown and compute C_T from(10).

Consequently, the mass diffusion-thermal analogy, first introduced in: $U_q \equiv C$ and $J_q \equiv J_m$, can be completed by this last statement: $T \equiv C_L$ (17).

Further analogies unfortunately are not possible. While ABAQUS employs Fourier's law as its foundational thermal model, this approach is insufficient for capturing the intricate behaviour defined by the above equations. To address this limitation, a more sophisticated thermal material model must be integrated using the user subroutine UMATHT (please refer to Section 6).

In particular, the UMATHT subroutine in ABAQUS is required to model hydrogen embrittlement because standard built-in diffusion formulations cannot adequately represent the complex, coupled transport behaviour of hydrogen in metallic materials, particularly the interaction between lattice hydrogen and microstructural trapping sites. Hydrogen embrittlement is governed not only by the diffusion of hydrogen through the lattice but also by its reversible and irreversible trapping at defects such as dislocations, grain boundaries, inclusions, and voids. These trapping sites significantly alter the effective hydrogen concentration available for diffusion and damage initiation. UMATHT allows the user to define a custom heat transfer–analogue diffusion formulation in which the governing equations can be modified to incorporate trap occupancy kinetics, binding energies, and site densities. This is essential because the total hydrogen concentration is partitioned into mobile lattice hydrogen and trapped hydrogen, with only the lattice component contributing directly to flux, while the trapped concentration evolves based on local thermodynamic equilibrium or kinetic trapping–detrapping laws. Without UMATHT, ABAQUS assumes simplified diffusion behaviour that cannot capture concentration-dependent trapping saturation or the delayed release of hydrogen from deep traps under stress gradients. By explicitly modelling trap site concentration and occupancy, UMATHT enables accurate prediction of local hydrogen accumulation, which is critical for simulating embrittlement initiation, crack nucleation, and subcritical crack growth in susceptible alloys under mechanical loading.

2.4.4 Cohesive Element Implementation - Introduction

The concept of the cohesive zone was introduced by [66] and [67] in the 1960s with the aim of approximating the nonlinear process occurring in the fracture process zone (FPZ), thereby avoiding the need to rely on the stress singularity of linear elastic fracture mechanics in the continuum medium.

The damaged zone or cohesive zone is represented by a fictitious crack where the cohesive force acting on both surfaces prevents crack propagation. The behaviour of the cohesive zone is described through a constitutive relationship – a traction-separation law (TSL) – that relates the tractions acting on the cohesive interface and the displacement jump between the faces of the cohesive interface, referred to as separation [68]

As shown in Figure 2-10, the stress singularity characteristic of linear elastic fracture mechanics is replaced by a more realistic stress distribution along the fracture process zone or cohesive zone.

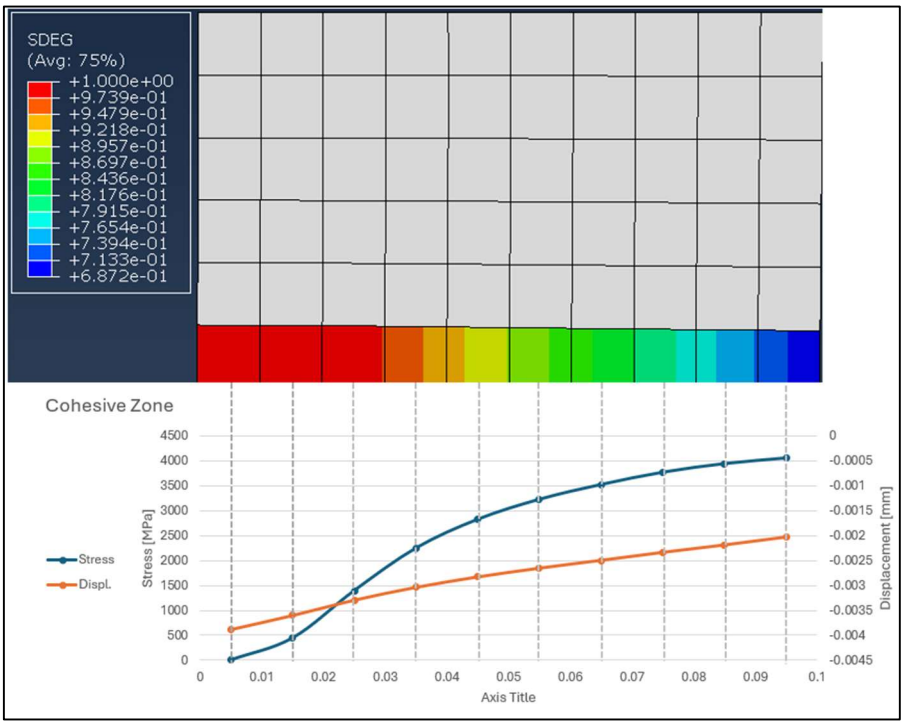

Figure 2-10: Numerical simulation of cohesive material behaviour under Mode I loading (tension, maximum cohesive stress and corresponding separation)

As it can been Figure 2-10 the first cohesive element on the left has been fully degraded (there is vertical displacement and the element is not able to provide anymore resistance – stress

is nil), and the more we move on the right between cohesive elements, the "resistance" stress to fracture is increasing because the elements are not fully degraded.

In cohesive crack models, the softening curve is a material property that represents the relationship between the stress transmitted across the crack faces and the separation once damage initiation occurs. The most relevant properties of the softening function are the material's tensile strength ($\sigma_{max,0}$) and the cohesive fracture energy (Γ_0). The peak of the softening curve is governed by the material's cohesive strength ($\sigma_{max,0}$) which represents the stress at which the crack forms and begins to open. The cohesive fracture energy (Γ_0) is a constant that represents the external work required to create a unit area of cracked surface [69].

The ability to describe the fracture process using only two experimentally derived parameters makes cohesive zone models a highly valuable tool [70]. To determine cohesive parameters, experimental tests and micromechanical models are used. However, due to the inherent challenges in defining the softening curve, parametric fitting of experimental results is sometimes employed. Cornec and Scheider [70] proposed different methods for the experimental determination of cohesive material parameters namely, cohesive strength ($\sigma_{max,0}$) and cohesive energy (Γ_0), which corresponds to the area under the traction-separation law.

Inherent challenges in obtaining a softening curve include experimental instability after peak load, strain localization into narrow cracks, size effects, and strong sensitivity to boundary conditions and specimen heterogeneity. These issues make post-peak measurements noisy and often non-unique. Parametric fitting is commonly used to regularize the response by assuming a functional form, such as exponential or bilinear decay, calibrated to test data. While this approach is practical, its accuracy depends on data quality and model choice. For example, an exponential damage model fitted to concrete test data may yield an R^2 of 0.97, indicating good but not perfect agreement with experiments.

Another important parameter is the material's characteristic length (l_{ch}) [71]. Since this length is related to the size of the fracture process zone, it restricts the maximum finite element size when working with cohesive elements. It depends on the material's elastic modulus (E) cohesive fracture energy (Γ_0), and tensile strength ($\sigma_{max,0}$).

$$l_{ch} = \frac{E \cdot \Gamma_0}{\sigma_{max,0}^2} \tag{18}$$

The formulation of cohesive models under monotonic loading conditions is well-documented by Brocks et al. [72]. Once the cohesive parameters have been determined, the choice of the material behaviour law in the cohesive zone is key when applying cohesive crack models.

The influence of the shape of the traction-separation law on the material's fracture behaviour is not without some controversy. Scheider and Brocks [73] found a significant influence on the results, contrary to Tvergaard and Hutchinson [74].

Over the years, various cohesive laws have been used depending on the material or application being analysed—bilinear, trapezoidal, polynomial, exponential, among others [71], [73], [74], [75], [76] and [77] (see Figure 2-11).

Among the most popular cohesive laws for metals are the one proposed by Tvergaard and Hutchinson [74] and the exponential law by Xu and Needleman [75] later applied to ductile materials by Siegmund and Brocks [78]

Since polynomial and exponential cohesive laws are preferred for numerical reasons due to their continuity and differentiability, the exponential law by Xu and Needleman [75] gained significant popularity. The fact that the normal and tangential cohesive stresses are obtained by deriving the cohesive potential function—which is continuous and differentiable—facilitated the study of crack propagation under dynamic conditions conducted by Ortiz and Pandolfi [79].

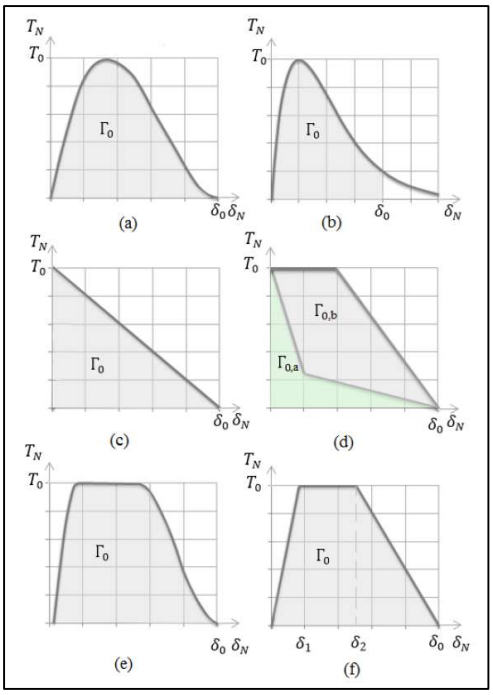

Figure 2-11: The most popular traction-separation laws: (a) Needleman, (b) Xu and Needleman, (c) Hillerborg, (d) Bazant, (e) Scheider and Brocks, (f) Tvergaard and Hutchinson. [80]

The shape of the traction–separation law strongly influences how cracks initiate and propagate in cohesive zone models. It defines how traction (stress) varies with increasing separation between surfaces. A steeper initial slope represents higher stiffness and smaller elastic opening before damage begins. A peak traction controls the maximum load the interface

can sustain. The softening branch shape (linear, exponential, or bilinear) governs energy dissipation and crack growth stability. A gradual softening leads to stable crack propagation, while abrupt drop promotes brittle failure. The total area under the curve equals fracture energy, so different shapes with same area can still produce different fracture behaviour.

It is important to note that the presence of a finite slope in the cohesive law before damage initiation has no physical meaning and is established based on numerical criteria with the ultimate goal of facilitating implementation in a finite element code. However, the damage initiation values and the softening curve are purely phenomenological parameters and must be analysed for each material and corresponding phenomenon.

Cohesive crack models allow the simulation of crack initiation and propagation without requiring the element to be pre-cracked, as well as the fracture of materials without the need for an explicit fracture criterion [81]. However, the widespread use of cohesive crack models for analysing material fracture behaviour emerged from their implementation via the finite element method by Hillerborg et al. for quasi-brittle materials like concrete [71]. It was precisely with concrete that cohesive crack models gained popularity as predictive tools for crack initiation and propagation, thanks to the work of Elices et al. [81] , Planas et al. [82] and Bazant [77].

The application of cohesive crack models to metallic materials was carried out by Needleman [83] [84], Tvergaard and Hutchinson [74] [85] [86] and Tvergaard [87]. Lin, Cornec et al. [88] applied the model to crack propagation analysis. The idea of introducing a potential to capture material decohesion was proposed by Xu and Needleman [75], becoming a reference for the numerical implementation of cohesive zone models.

The use of cohesive crack models extended to other damage processes to study a wide variety of physical phenomena. Thus, Xu and Needleman [76] and Zavattieri and Espinosa [89] conducted studies on dynamic fracture. Rosa et al. introduced a time-dependent cohesive model [90], Allen and Searcy applied the cohesive crack model to the study of viscoelastic materials [91], and Tijssens analysed the "crazing" phenomenon in polymers using the cohesive fracture surface methodology [92], among others. A compilation of cohesive models under monotonic loading can be found in the practical guide for applying cohesive models by K.-H. Schwalbe et al. [93], while Park and Paulino [94] conducted a critical review of the different traction-separation laws referenced in the literature, with special emphasis on the PPR (Park-Paulino-Roesler polynomial-based potential) crack model developed by the authors for mixed-mode loading conditions.

2.4.4.1 Cyclic loading for the Cohesive Zone

A review of cyclic cohesive zone models for simulating fatigue crack growth can be found in [95]. An important aspect to consider in all of them is what happens after damage initiation. The literature presents different models for material behaviour during unloading, as seen in Figure 2-12. For quasi-brittle materials, unloading is assumed to occur toward the coordinate

origin [96] [97] [98] [99] [100] [101] as shown in Figure 2-12(a), while other authors consider a certain residual separation [102] [103] as depicted in Figure 2-12(b). The unloading segment can be assumed to be linear [96] [100] [101] [102, 104, 105, 61, 106] [103] or nonlinear [98] [99] as presented in Figure 2-12(c) and Figure 2-12(d).

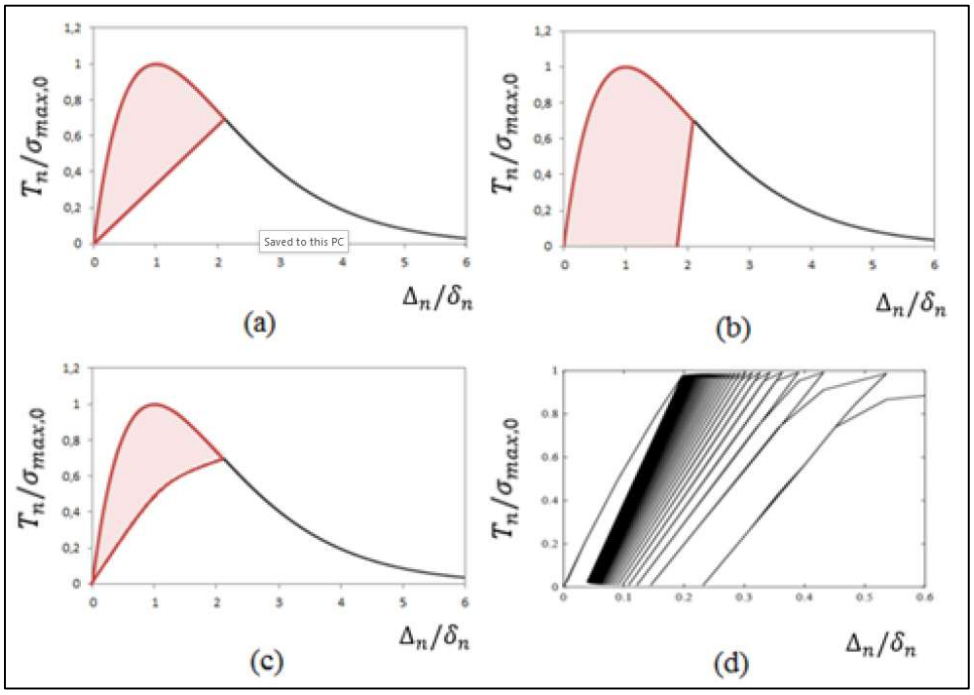

Figure 2-12: Cohesive laws with damage accumulation during fatigue loading:(a) Linear unloading to the coordinate origin [107], (b) Linear unloading with residual separation [103], (c) Nonlinear unloading to the coordinate origin [99], (d) Cyclic traction-separation law under load control [103].

Similar to monotonic cohesive zone models for which the damage state is defined by the maximum separation, in fatigue the damage evolution law also considers the material's strength limit and other additional material parameters incorporated using the Heaviside step function [103]. Different approaches to the damage variable can be found in the literature [100] [103] [108].

Previous studies by Cleveringa et al. [109] and Deshpande et al. [110] [111] [112] demonstrated the significant role of dislocations in the fatigue crack growth process. Riemelmoser and Pippan [113] showed the importance of geometrically necessary dislocations (GNDs) in fatigue crack growth and, consequently, the need to incorporate plastic strain gradient theories (SGP) to compute dislocation densities as the sum of statistically stored dislocations (SSDs) and geometrically necessary dislocations (GNDs). Taking all these factors into account, along with Brickmann's earlier model of dislocation density as a function of plastic strain gradients [112], Brickmann and Siegmund [104] proposed a pioneering fatigue

cohesive zone model based on dislocation micromechanisms (DDSG, Dislocation Density-Based Strain Gradient model). With this model, they successfully incorporated the influence of dislocations on material separation, thereby overcoming the limitations in cycle number and the restriction of the domain region to a few micrometers found in discrete dislocation models [109], [110] and [111].

Although fatigue crack growth, including the effects of overloads during constant amplitude loading, has been extensively studied [96] [100] [102], beyond these loading conditions, there are no studies clarifying the interdependence between crack propagation rates and cohesive zone model properties [95].

It is important to reference the methods documented in the literature to address the convergence problems inherent to crack models attributed to softening. One way to improve convergence is the use of control algorithms, where loading is applied by prescribing a variable that increases monotonically during the loading history, such as crack opening [105]. However, the control algorithm cannot be used in cases of cyclic loading. In these cases, it is more appropriate to facilitate numerical convergence using the viscous regularization coefficient technique proposed by Gao and Bower [114], keeping in mind that for optimal results, the viscosity coefficient must be sufficiently small [106].

2.4.4.2 Cohesive Element modelling in presence of Hydrogen

The ability of cohesive crack models to accurately predict the consequences of hydrogen embrittlement in components, materials, and structures is of vital importance for facilitating the use of high-strength steels in the energy sector and thus contributing to the development of storage and distribution infrastructure for future energy systems. While most studies reliably reproduce experimental results, certain limitations still exist [61] [62].

Álvaro et al. [61] and Olden et al. [115] developed a cohesive crack model for monotonic loading conditions, primarily accounting for the HEDE (Hydrogen-Enhanced Decohesion) mechanism. Brocks et al. [116] also included surface kinetics in hydrogen absorption.

The traction-separation law in the presence of hydrogen can be reformulated using the relationship proposed by Serebrinsky et al. [7] where: k is defined as the cohesive energy scaling factor and it is used in the model to reduce the area below TSL curve, $\sigma_{max,0}$ is the cohesive stress in the absence of hydrogen, θ_H is the hydrogen coverage, and σ_{max,θ_H} is the critical cohesive stress dependent on the latter.

$$k = \frac{\sigma_{max,\theta_H}}{\sigma_{max,0}} = 1 - 1.0467\psi + 0.1687\psi^2 \tag{19}$$

where ψ represents the ratio between the hydrogen concentration and the concentration of hydrogen at saturation level

$$\psi = \frac{\theta_H}{\overline{\theta_H}} \tag{20}$$

Figure 2-13 shows the traction-separation law as a function of hydrogen concentration. A gradual decrease in fracture energy is observed as the hydrogen content increases, following the exponential cohesive law by Xu and Needleman [75].

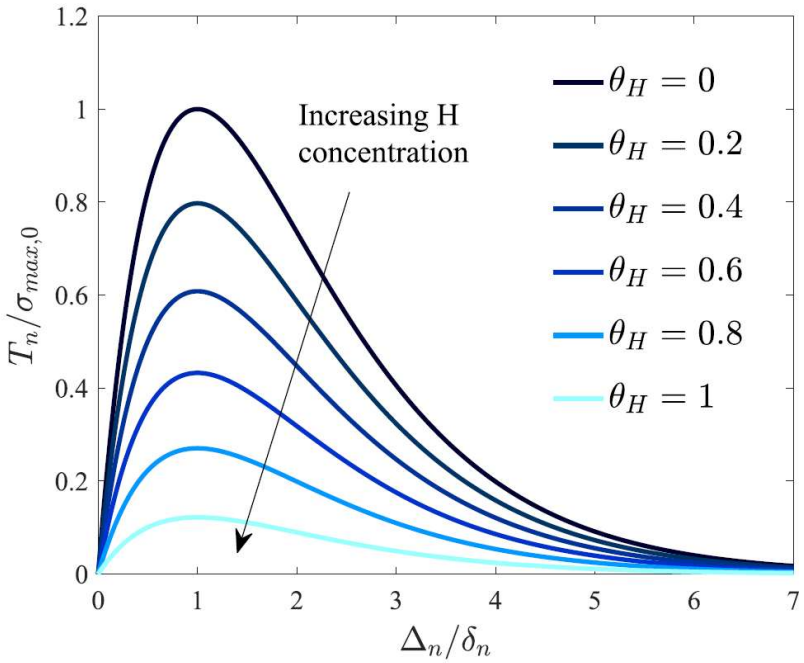

Figure 2-13: Effect of hydrogen coverage θ_H on the traction-separation law characterizing the cohesive response.

Most attempts to model hydrogen-induced embrittlement using cohesive zone models have been applied to monotonic loading. However, many structural components in industry operate under fatigue conditions. The pioneering work of Moriconi et al. [62] presents a series of experiments and numerical simulations within the framework of conventional plasticity theory, aiming to investigate the role of hydrogen in martensitic 15-5PH steel used for gaseous hydrogen storage under fatigue conditions. The numerical predictions agree well with experimental data for low hydrogen pressures but fail to capture the detrimental effect of hydrogen on fatigue crack propagation at high hydrogen pressures.

Another key factor is the so-called plastic strain gradient effect, associated with plastic strain gradients. Martínez-Pañeda et al. [117] demonstrated a significant influence of plastic strain gradients across a wide range of fracture problems, which is particularly important in the

numerical modelling of hydrogen-assisted cracking – where hydrostatic stress plays a central role in interface decohesion and hydrogen diffusion.

2.4.4.3 Cohesive Zone Models for Damage Modelling in Notches

Catastrophic failures originating from small defects in structural components have motivated numerous theoretical and experimental studies to evaluate brittle fracture in the presence of notches (see, for example, the review by Ayatollahi et al. [110]). The application of cohesive zone models for damage modelling in notches, with the aim of developing a fracture criterion for notched specimens, was investigated by Gómez and Elices [118] [119]. This study was later extended to linear elastic materials [120]. Olden et al. [121] studied hydrogen embrittlement in notched specimens using a cohesive formulation dependent on hydrogen content. More recently, Cendón et al. [122] evaluated the capability of the embedded cohesive crack model to predict critical loads in U-notched and V-notched specimens with different notch root radii, made of coarse-grained polycrystalline graphite. However, all studies conducted so far are limited to the use of conventional models.

2.4.4.4 Dynamic Hydrogen Coverage

As previously mentioned, the proposed approach simulates how an aqueous solution infiltrates the material as the crack extends. This methodology has already been introduced in previous peridynamic studies [123] and the proposed FEA approach shows the peculiar importance of capturing the mentioned phenomena as part of the analysis. As shown in the following sections, neglecting the implementation of hydrogen dynamic penetration may lead to substantial under-estimate of the crack propagation velocity.

In particular, when the computation code evaluates that a specific cohesive element is fully degraded, a new text file is generated including the input script for a new analysis and terminate the specific step and analysis. As mentioned, the new ABAQUS input file is generated as output by a FORTRAN subroutine in ABAQUS and includes the entire script for a new analysis step. In the analysis step the boundary conditions will reflect the hydrogen coverage to the newly formed crack surfaces. The new input file is then executed by ABAQUS as restart file, and will initiate the analysis from the last step and iteration from the previous analysis.

3 Validation/Test Case

The first numerical example is a validation case to test the proposed approach by considering a two-dimensional plate with dimensions of 0.1x0.11m. The FEM is presented in Figure 3-1. The model consists of Bidimensional 4-node cohesive elements (COH2D4T) with displacement and temperature degrees-of-freedom (DOF) in conjunction with 4-node plane strain thermally coupled quadrilateral elements (CPE4T) with displacement and temperature DOF. The cohesive elements are placed horizontally in the location of a possible crack (horizontally in the middle of the sample). Cohesive elements have 2(two) integration (Gauss) points whereas the 4-node plane strain continuum elements have 4(four) integration (Gauss) points.

The finite element model consists of ten cohesive elements (series 5000 in Figure 3-1) and one hundred continuum elements placed symmetrically on both sides of the ten cohesive elements (series 100, 200, 300, …, 1000 in Figure 1). For simplicity the cohesive and continuum elements have the same dimensions.

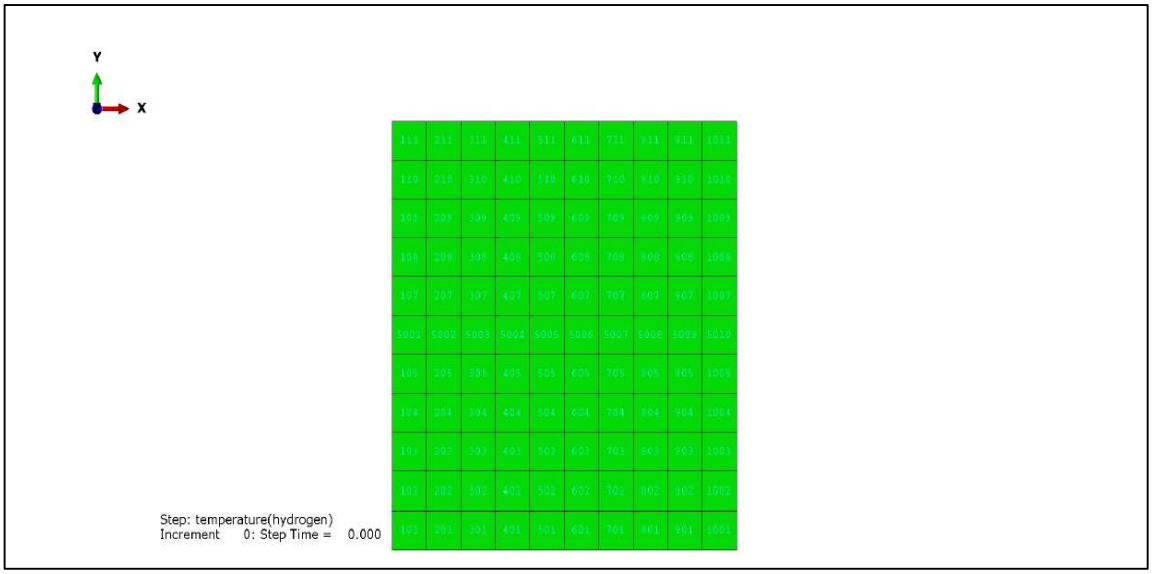

Figure 3-1: Finite element model of the validation case

The applied load is constant and uni-axial (mode I test). The simulation is run under displacement control, applying the same displacement u_y to the upper and bottom nodes of the continuum elements. The material of the continuum elements is a linear elastic material with Young's Modulus E of 205,000MPa, Poisson's Ratio ϑ of 0.3 and Diffusivity D_L of 0.00084mm^2/s. The constitutive law of the cohesive element is defined as elastic for the initial

slope of the TSL, maximum stress for the damage initiation criterion, and displacement type linear softening behaviour for damage evolution. All TSL parameters have been defined as a function of the concentration of hydrogen, which is the temperature variable in ABAQUS based on the analogy between the thermal diffusion and hydrogen diffusion considered in this study.

3.1 Cohesive elements performance in the presence of hydrogen

In this test case, the sample is pre-charged for a specific value of hydrogen concentration for which the corresponding value of ψ and k have been calculated. The analysis then runs only one step for which the following boundary conditions are applied:

- 1st step: displacement u_y (0.006mm) is applied to the upper and bottom nodes of the continuum elements.

Figure 3-2 summarises the results for four tests performed for different hydrogen concentrations for which the corresponding value of ψ and k have been calculated. For clarity, all four tests were carried out without and with the presence of hydrogen, $k = 1.00, 0.67, 0.37$ and 0.12 (which corresponds to sample charged to saturated level of hydrogen) and TSL curves were reconstructed from the analysis. As can be seen in this figure, TSL curves are different for different concentrations of hydrogen which are degrading as the hydrogen concentration changes.

Figure 3-2: TSL curves for different hydrogen concentration values

These results demonstrate that our model/methodology can accurately reproduce the TSLs in accordance with the input data which describe the presence of hydrogen at various concentration levels within the sample.

As can be seen Figure 3-2, for each concentration level, degradation occurs after the elements exceed the displacement value corresponding to the maximum stress values. The selected concentrations of hydrogen are arbitrary, and they are a fraction of the saturation concentration of hydrogen (2.650x10-11mol/mm2), instead the selected value of displacement is sufficient to make sure that all the cohesive elements are fully degraded once the hydrogen get diffused within the entire specimen (and there is not an upper limit).

3.2 Sample charged with hydrogen without dynamic coverage

In this case, the initial condition of the sample is without presence of hydrogen. The analysis is then performed with 2(two) steps in which the following boundary conditions are applied:

- 1st step: displacement u_y (0.0017mm) is applied to the upper and bottom nodes of the continuum elements.
- 2nd step: the saturation concentration of hydrogen ($2.650x10^{-11}mol/mm^2$) is applied to the four nodes of Element ID 5001 (please refer to Figure 4-1)

The following figures (Figure 4-3 to Figure 4-10) show results for the hydrogen concentration and cohesive degradation at various time intervals. As it can be seen in the figures, the hydrogen saturation concentration is applied only to the four nodes of Element ID 5001 (please refer to Figure 1), and while the hydrogen gets diffused within the sample, at constant load, various cohesive elements reach full degraded status, i.e. SDEG parameter reaches 1.00 for a growing number of cohesive elements. Note that hydrogen boundary conditions do not change regardless of the degradation of the CZM.

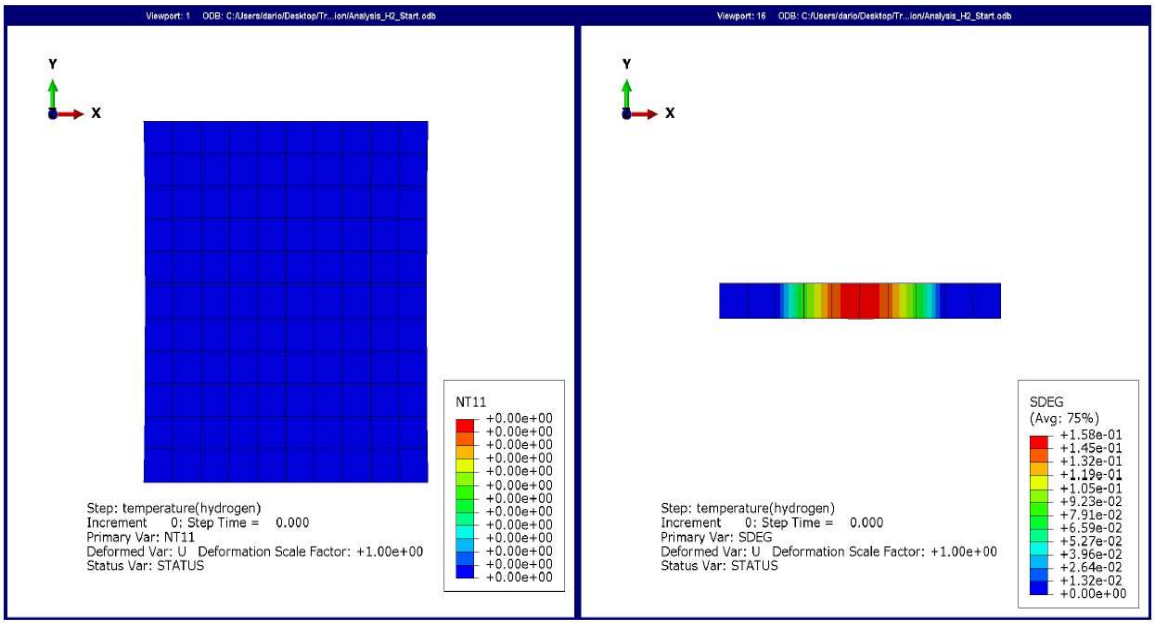

Figure 3-3: Simulation without Dynamic Hydrogen Coverage: Hydrogen concentration (NT11), cohesive element degradation (SDEG) at step time 0.000sec. (before applying hydrogen)

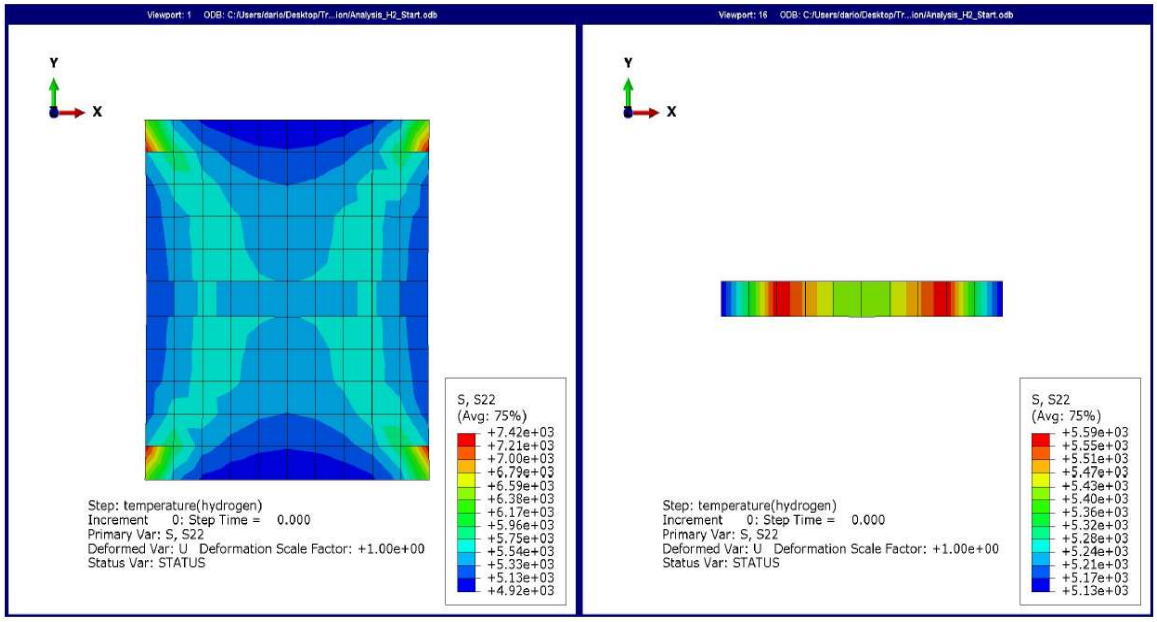

Figure 3-4: Simulation without Dynamic Hydrogen Coverage: Uniaxial stress value (S22) and Uniaxial stress value for the cohesive elements only at step time 0.000sec. (before applying hydrogen)

The above figures Figure 3-3 and Figure 3-4 give a graphical representation of the numerical analysis results once Step1 is completed (displacement only is applied and no hydrogen is present). As it can be seen in all the above figures, the cohesive elements in the middle (ID

5005 and 5006) are partially degraded having a SDEG of approx. 0.16 and associated value of stress S22 is of approx. 5400MPa (smaller than the $\sigma_{max,0}$ = 5600MPa). This means that the point representing the status of the cohesive elements on the stress-strain curve is in descending part of the TSL representing absence of hydrogen (ψ = 0 and k = 1) (descending part of the yellow TSL in Figure 3-2). As expected, the above figures also show that hydrogen is not diffused NT11 = 0.

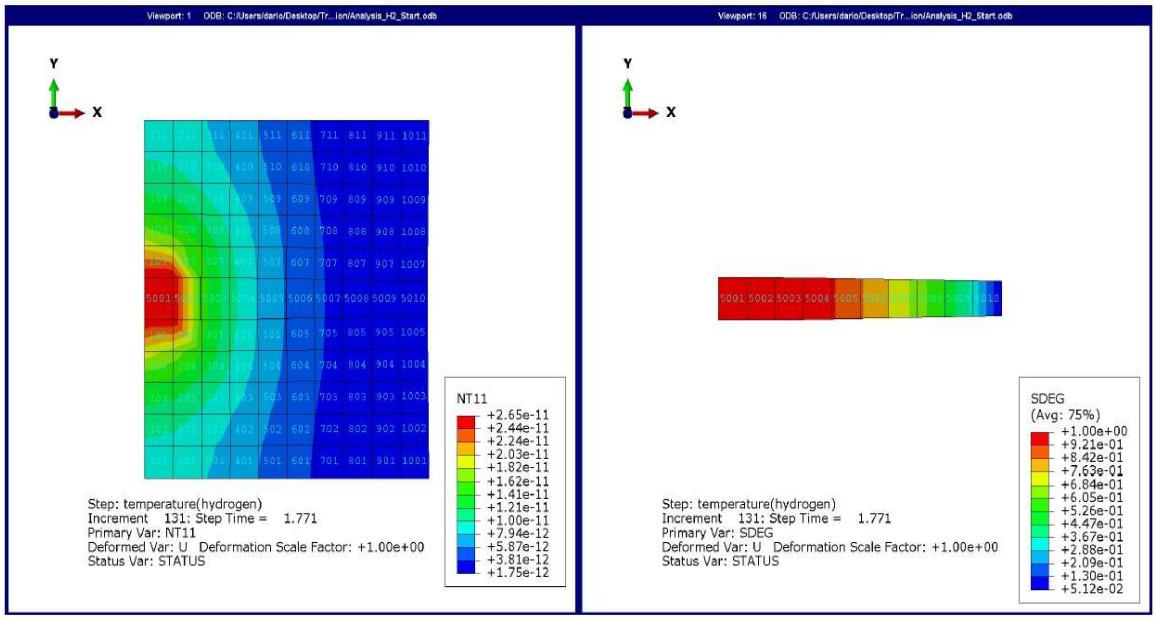

Figure 3-5: Simulation without Dynamic Hydrogen Coverage: Hydrogen concentration (NT11), cohesive element degradation (SDEG) at step time 1.771sec. (Element 5003 is fully degraded)

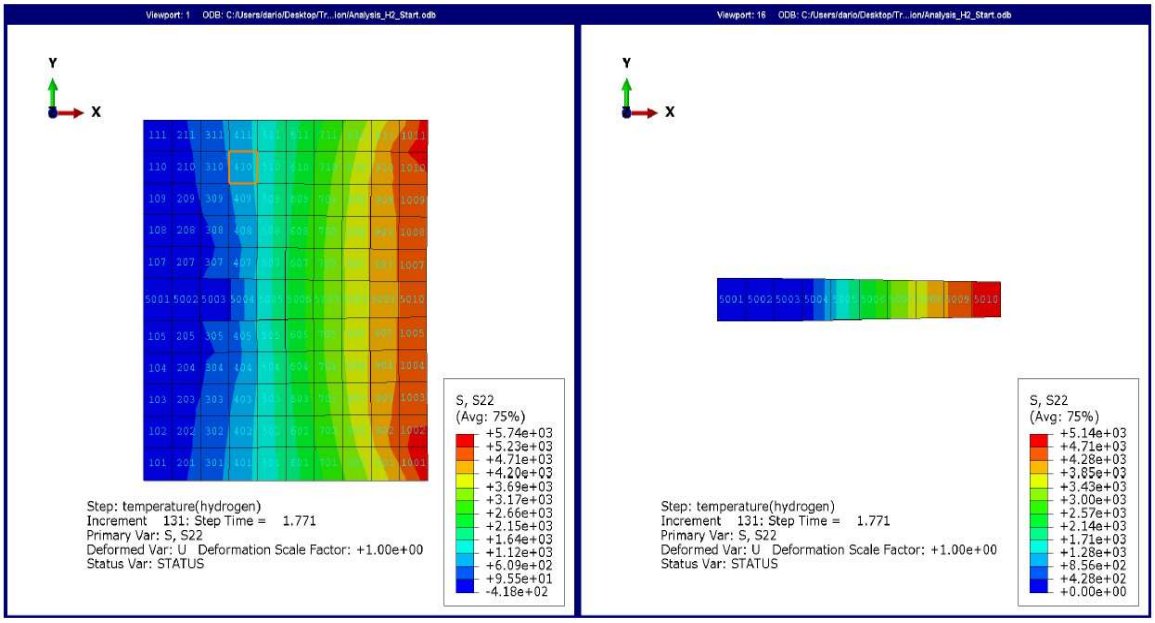

Figure 3-6: Simulation without Dynamic Hydrogen Coverage: Uniaxial stress value (S22) and Uniaxial stress value for the cohesive elements only at step time 1.771sec. (Element 5003 is fully degraded)

Figure 3-5 and Figure 3-6 give a graphical representation of the numerical analysis results once Step1 is completed, hydrogen has been applied to the 4 nodes of the cohesive element having ID 5001, hydrogen is getting diffused within the specimen and cohesive element with ID 5001, 5002 and 5003 are fully degraded (1.771sec.). As it can be seen in all the above figures, the cohesive elements having ID5001, 5002 and 5003 are fully degraded having a SDEG of 1.0 and the cohesive elements do not contribute to resistance (S22 = 0MPa). This means that the point representing the status of elements having ID5001, 5002 and 5003 in the stress-strain curve (Figure 3-2) is beyond the point where the grey curve (representative of the cohesive elements saturated of hydrogen $\psi = 1$ and $k = 0.12$) intersect the X-axis. As expected, the above figures also show that saturated concentration of hydrogen is applied to the 4 nodes of the cohesive element having ID 5001 and hydrogen is diffusing in the specimen.

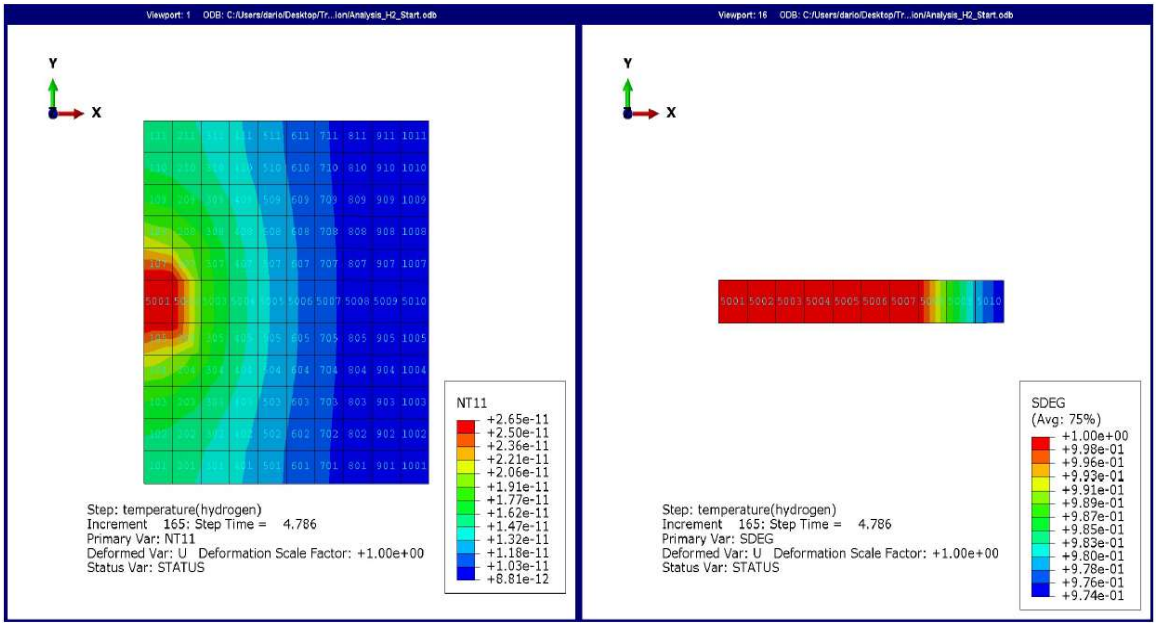

Figure 3-7: Simulation without Dynamic Hydrogen Coverage: Hydrogen concentration (NT11), cohesive element degradation (SDEG) at step time 4.786sec. (Element 5007 is fully degraded)

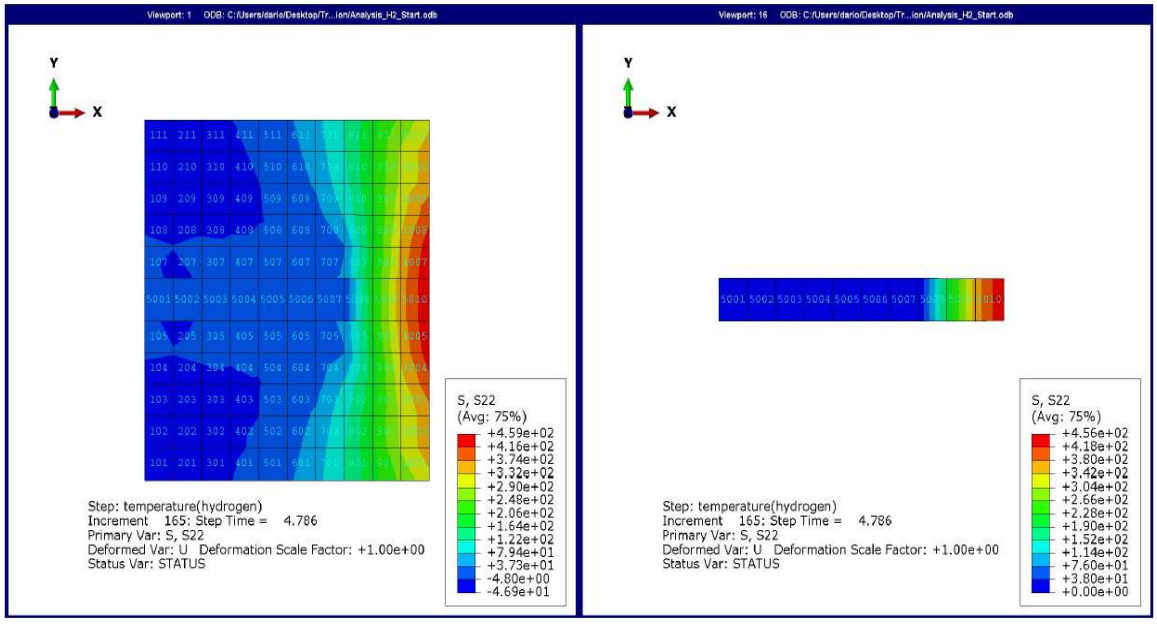

Figure 3-8: Simulation without Dynamic Hydrogen Coverage: Uniaxial stress value (S22) and Uniaxial stress value for the cohesive elements only at step time 4.786sec. (Element 5007is fully degraded)

Again Figure 3-7and Figure 3-8 give a graphical representation of the numerical analysis results once Step1 is completed, hydrogen has been applied to the 4 nodes of the cohesive element with ID 5001, hydrogen is getting diffused within the specimen and the majority of

the cohesive elements are fully degraded (4.786sec.). As it can be seen in all the above figures, the majority of the cohesive elements having are fully degraded having a SDEG of 1.0 and they do not contribute to resistance (S22 = 0MPa). This means that the point representing the status of the majority of the cohesive elements in the stress-strain curve (Figure 3-2) is beyond the point where the grey curve (representative of the cohesive elements saturated of hydrogen ψ = 1 and k = 0.12) intersect the X-axis. As expected, the above figures also show that saturated concentration of hydrogen is applied to the 4 nodes of the cohesive element having ID 5001 and hydrogen is diffusing in the specimen.

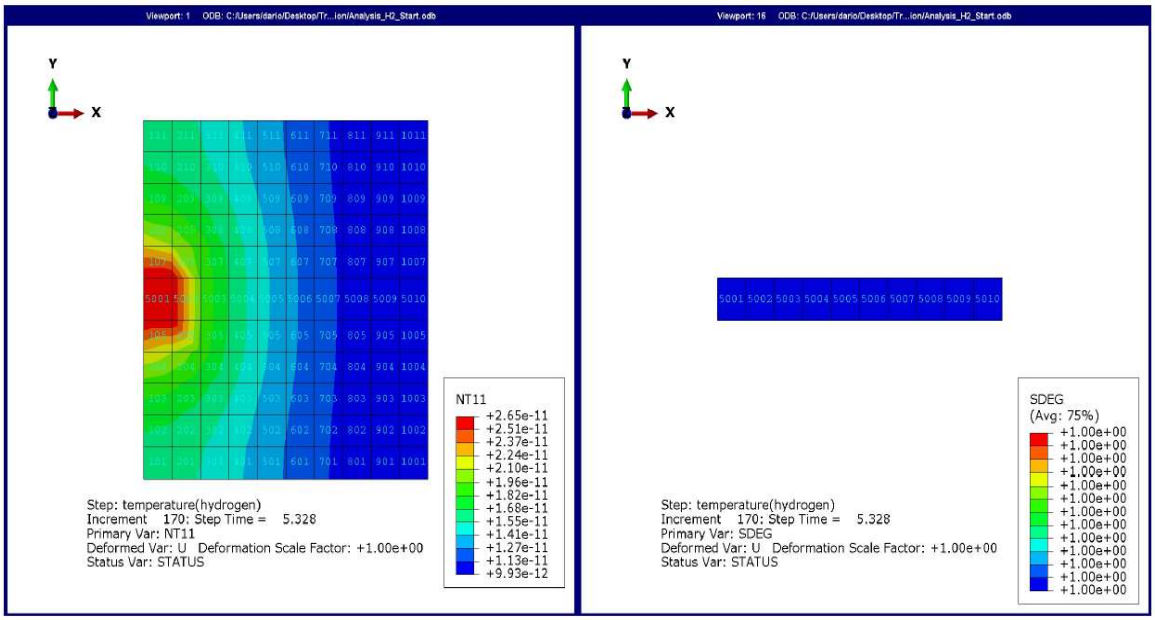

Figure 3-9: Simulation without Dynamic Hydrogen Coverage: Hydrogen concentration (NT11), cohesive element degradation (SDEG) at step time 5.328sec. (All Cohesive Elements are fully degraded)

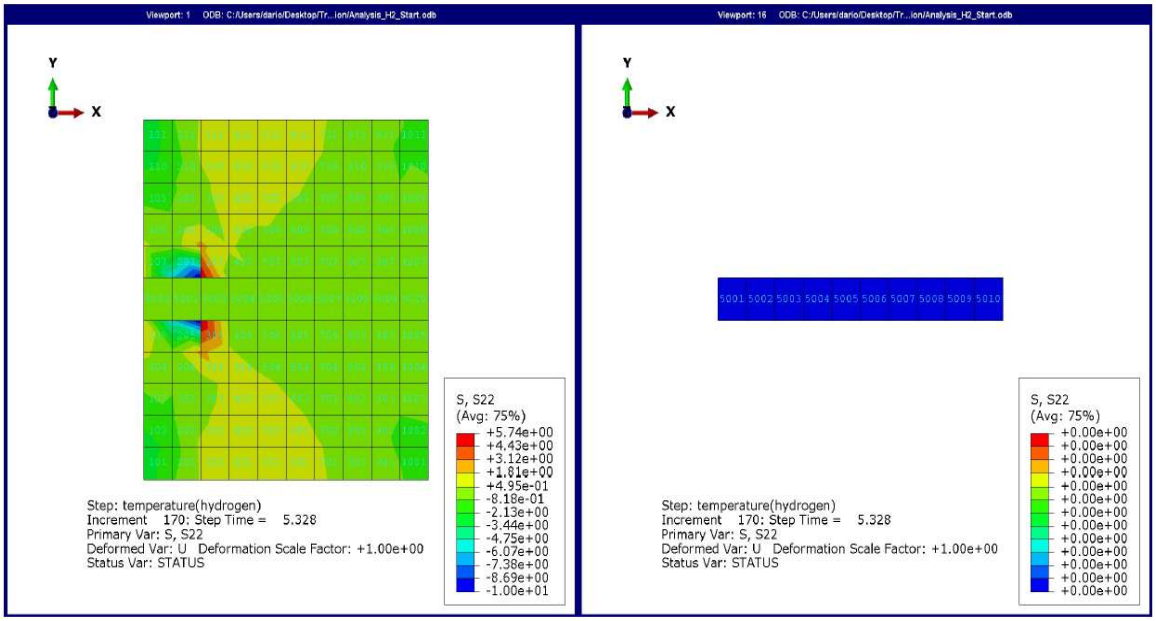

Figure 3-10: Simulation without Dynamic Hydrogen Coverage: Uniaxial stress value (S22) and Uniaxial stress value for the cohesive elements only at step time 5.328sec. (All Cohesive Elements are fully degraded)

In conclusion and as indicated in Figure 3-9 and Figure 3-10 the hydrogen is getting diffused completely with the specimen and all the cohesive elements are fully degraded (5.328sec.). As it can be seen in all the above figures, all the cohesive elements are fully degraded having a SDEG of 1.0 and they do not contribute to resistance (S22 = 0MPa). This means that the point representing the status of all the cohesive elements in the stress-strain curve (Figure 3-2) is beyond the point where the grey curve (representative of the cohesive elements saturated of hydrogen $\psi = 1$ and $k = 0.12$) intersect the X-axis. As expected, the above figures also show that saturated concentration of hydrogen is applied to the 4 nodes of the cohesive element having ID 5001 and saturated concentration of hydrogen is almost present in the entire specimen.

3.3 Sample charged with hydrogen by considering dynamic coverage

This study investigates the dynamic effects of hydrogen coverage during crack propagation. Specifically, a novel algorithm is designed to:

- identify the updated crack tip location, and
- assign a unit hydrogen coverage value to the newly formed crack surfaces.

The approach simulates how an aqueous solution infiltrates the material as the crack extends. For clarity, the sample having the same geometrical and loading characteristics as in the previous case has been considered in this case. As shown in the following figures (Figure 4-11 to Figure 4-18), the hydrogen saturation concentration is penetrating within the sample, and while the hydrogen gets diffused within the sample at constant load, various cohesive elements reach a full degraded status (SDEG parameter reaches 1.00 for a growing number of cohesive elements).

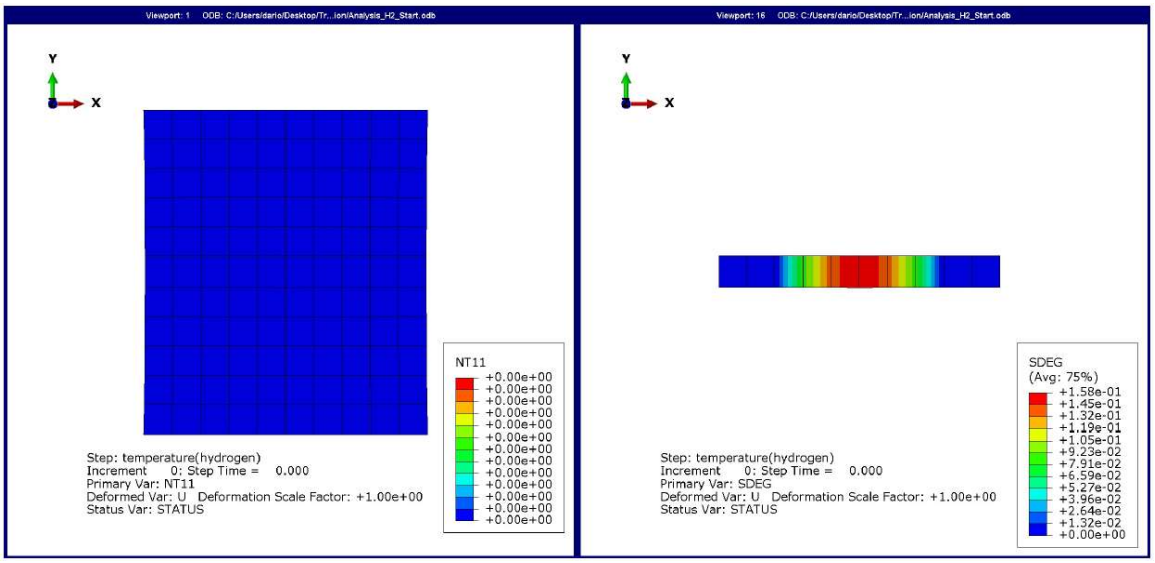

Figure 3-11: Simulation with Dynamic Hydrogen Coverage: Hydrogen concentration (NT11), cohesive element degradation (SDEG) at step time 0.000sec. (before applying hydrogen)

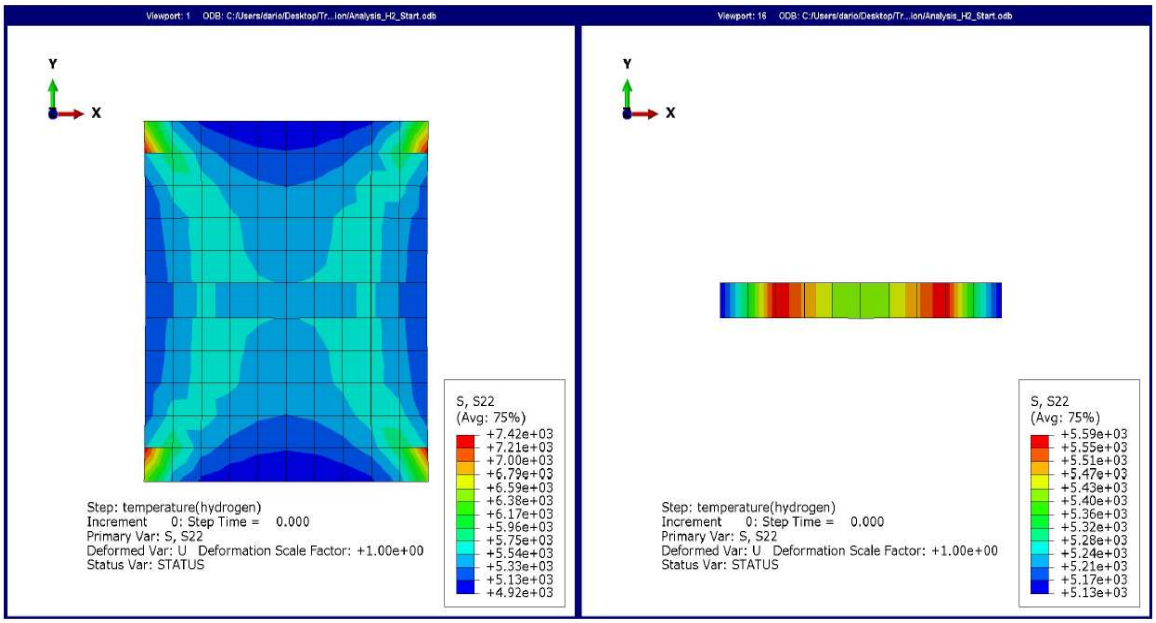

Figure 3-12: Simulation with Dynamic Hydrogen Coverage: Uniaxial stress value (S22) and Uniaxial stress value for the cohesive elements only at step time 0.000sec. (before applying hydrogen)

The above figures Figure 3-11 and Figure 3-12 give a graphical representation of the numerical analysis results once Step1 is completed (displacement only is applied and no hydrogen is present). As it can be seen in all the above figures, the cohesive elements in the middle (ID 5005 and 5006) are partially degraded having a SDEG of approx. 0.16 and associated value of stress S22 is of approx. 5400MPa (smaller than the $\sigma_{max,0}$ = 5600MPa). This means that the point representing the status of the cohesive elements on the stress-strain curve is in descending part of the TSL representing absence of hydrogen ($\psi = 0$ and $k = 1$) (descending part of the yellow TSL in Figure 3-2). As expected, the above figures also show that hydrogen is not diffused NT11 = 0, and the results correspond to the previous presented results as per Figure 3-3 and Figure 3-4 (which is an additional proof of the correctness of the methodology adopted in this study).

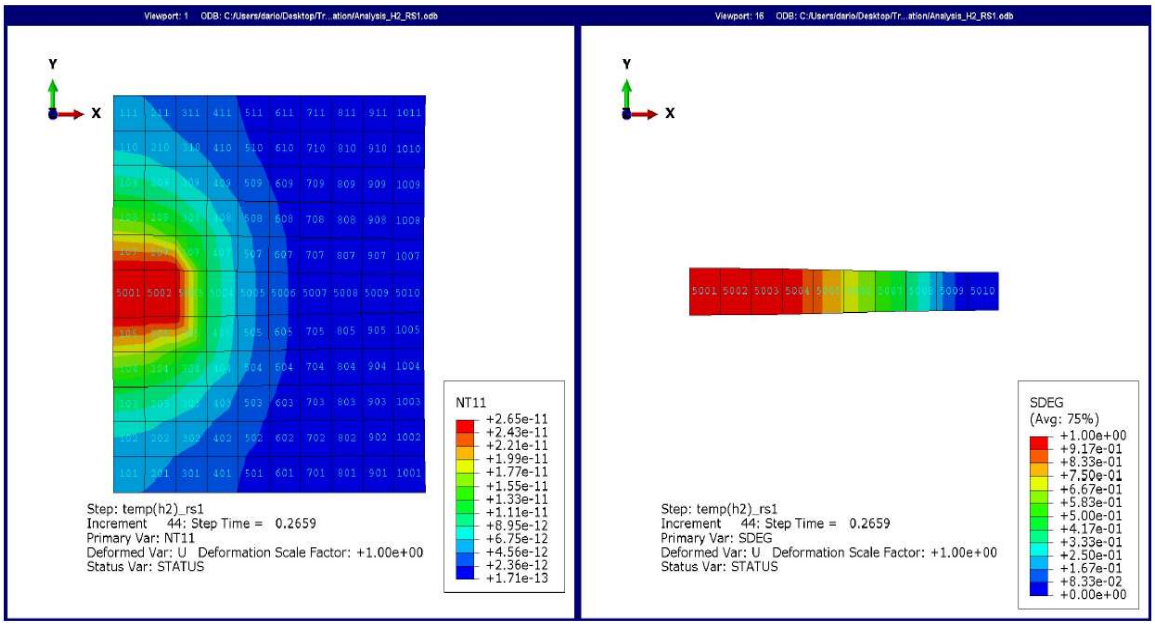

Figure 3-13: Simulation with Dynamic Hydrogen Coverage: Hydrogen concentration (NT11), cohesive element degradation (SDEG) when Element 5003 is fully degraded

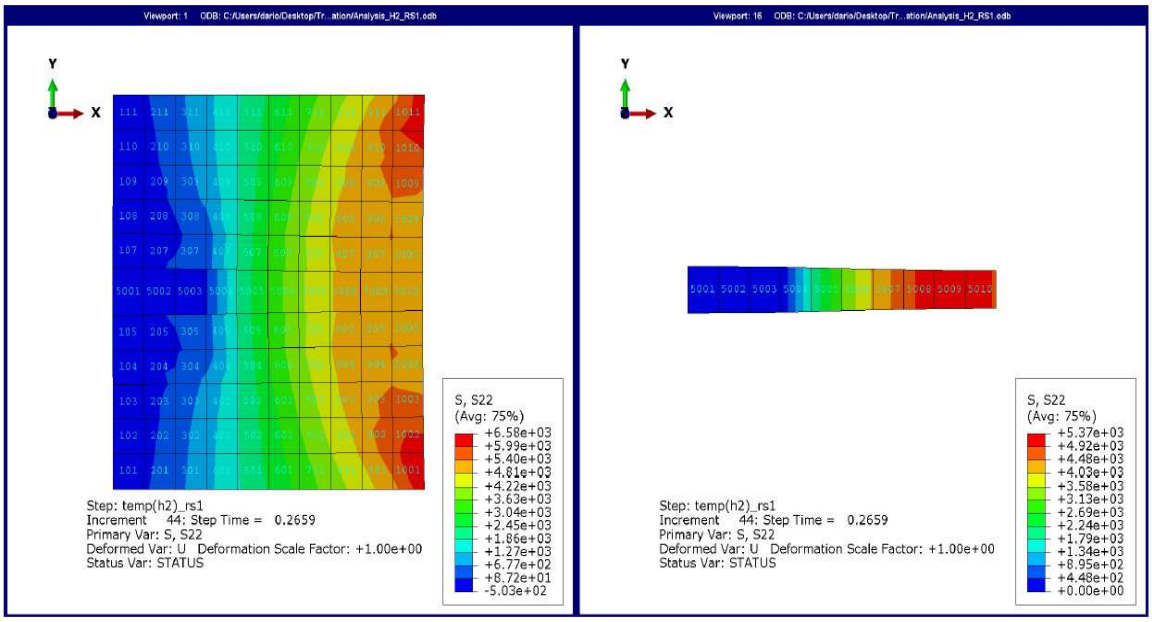

Figure 3-14: Simulation with Dynamic Hydrogen Coverage: Uniaxial stress value (S22) and Uniaxial stress value for the cohesive elements when Element 5003 is fully degraded

Figure 3-13 and Figure 3-14 provides an analogue representation as per Figure 3-5 and Figure 3-6. The difference between the two analysis is associated to the application of the hydrogen to the cohesive elements (BCs). In particular for the analysis represented in Figure

3-5 and Figure 3-6, the saturated level hydrogen is applied only to the 4 nodes of the cohesive element having ID 5001; instead for the analysis represented Figure 3-13 and Figure 3-14, the saturated level hydrogen is applied to the 4 nodes of the cohesive element having ID 5001 but also to the 4 nodes of the cohesive element having ID 5002. This is representative of the hydrogen dynamic coverage process, where the introduced algorithm changes the hydrogen BCs representing to the new opened surface where hydrogen can penetrate (4 nodes of cohesive element having ID 5001 and 5002).

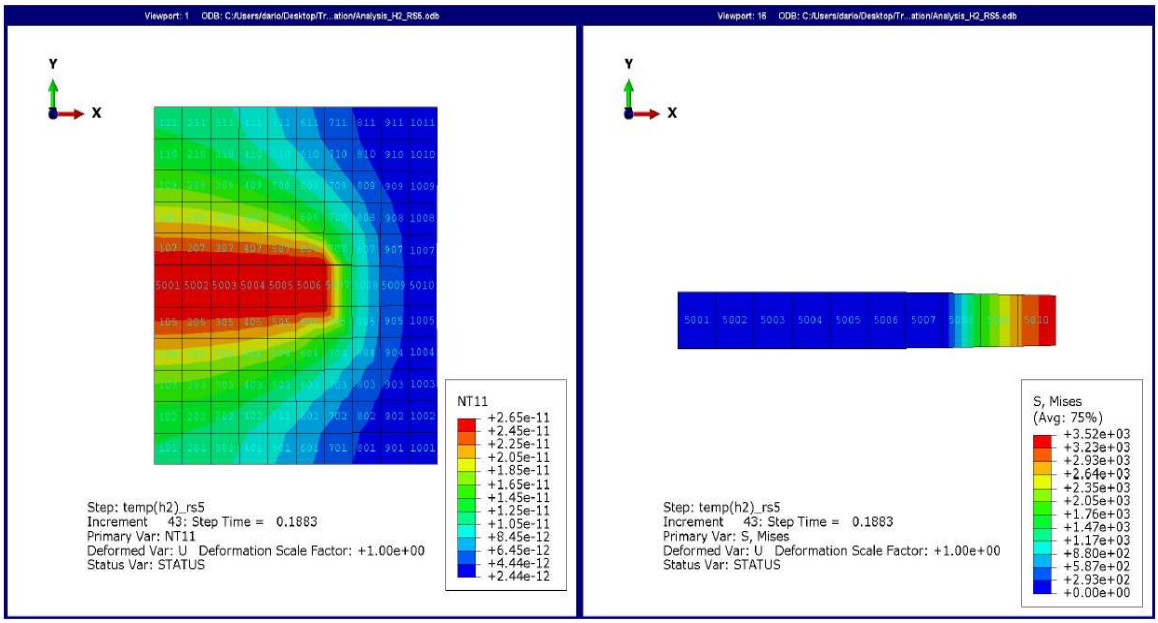

Figure 3-15: Simulation with Dynamic Hydrogen Coverage: Hydrogen concentration (NT11), cohesive element degradation (SDEG) when Element 5007 is fully degraded

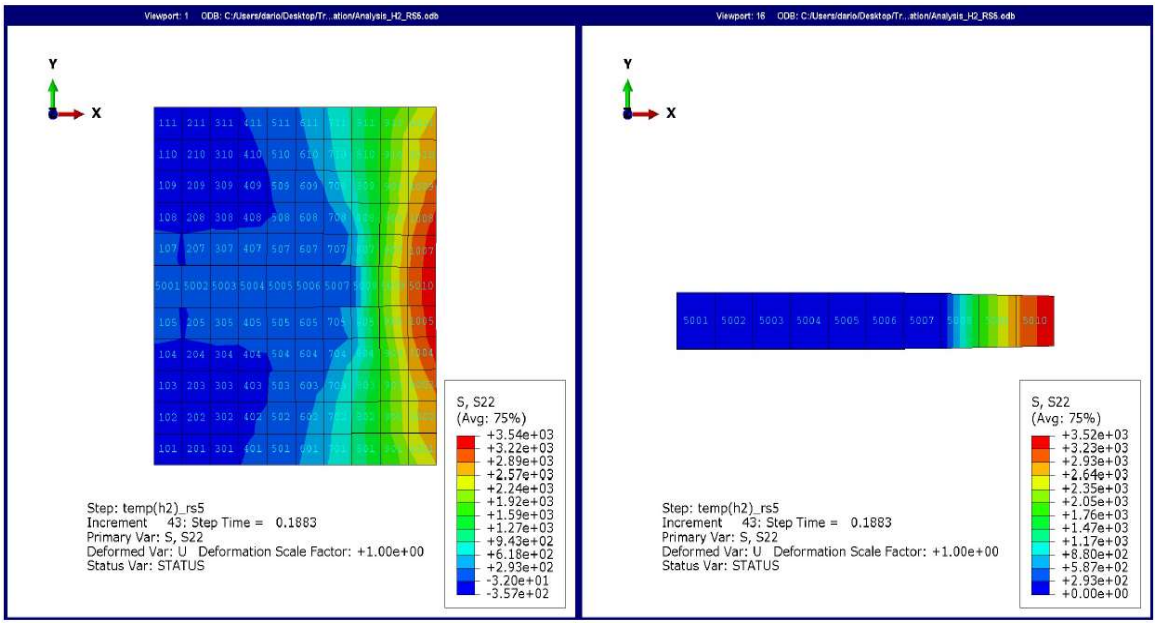

Figure 3-16: Simulation with Dynamic Hydrogen Coverage: Uniaxial stress value (S22) and Uniaxial stress value for the cohesive elements when Element 5007 is fully degraded

Figure 3-15 and Figure 3-16 provides again an analogue representation of the analysis as per Figure 3-7 and Figure 3-8. As explained above, the analysis represented by Figure 3-15 and Figure 3-16, introduce the dynamic hydrogen coverage algorithm where the saturated concentration of hydrogen is applied to the nodes associated to the cohesive elements having ID 5001, 5002, 5003, 5004, 5005 and 5006 (cohesive elements which are fully degraded).

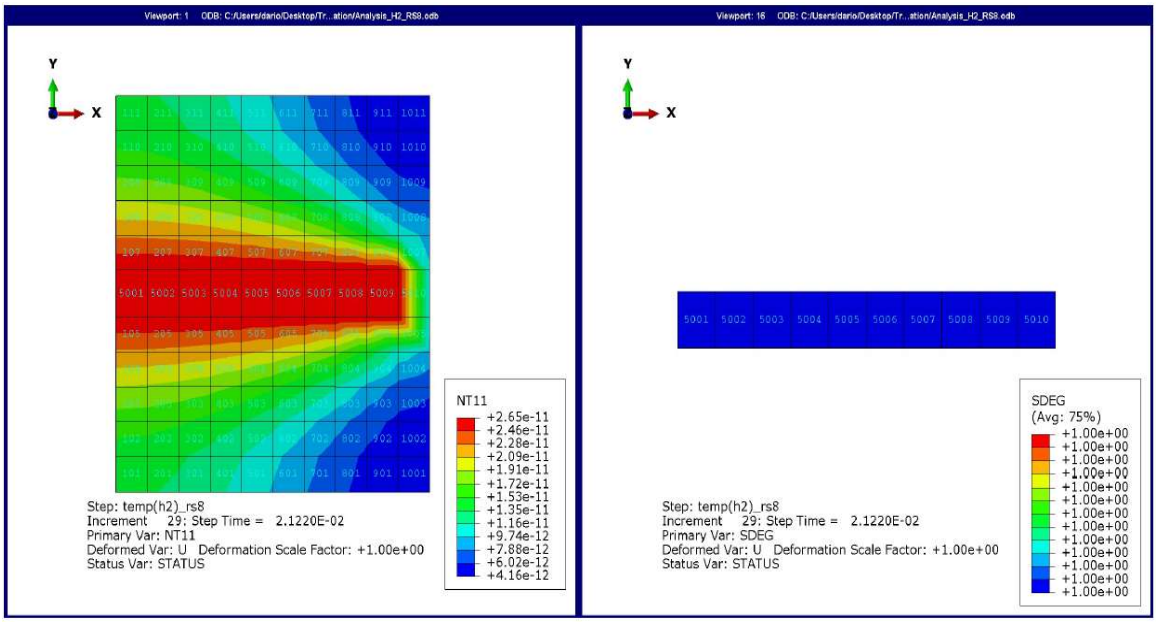

Figure 3-17: Simulation with Dynamic Hydrogen Coverage: Hydrogen concentration (NT11), cohesive element degradation (SDEG) when all Cohesive Elements are fully degraded

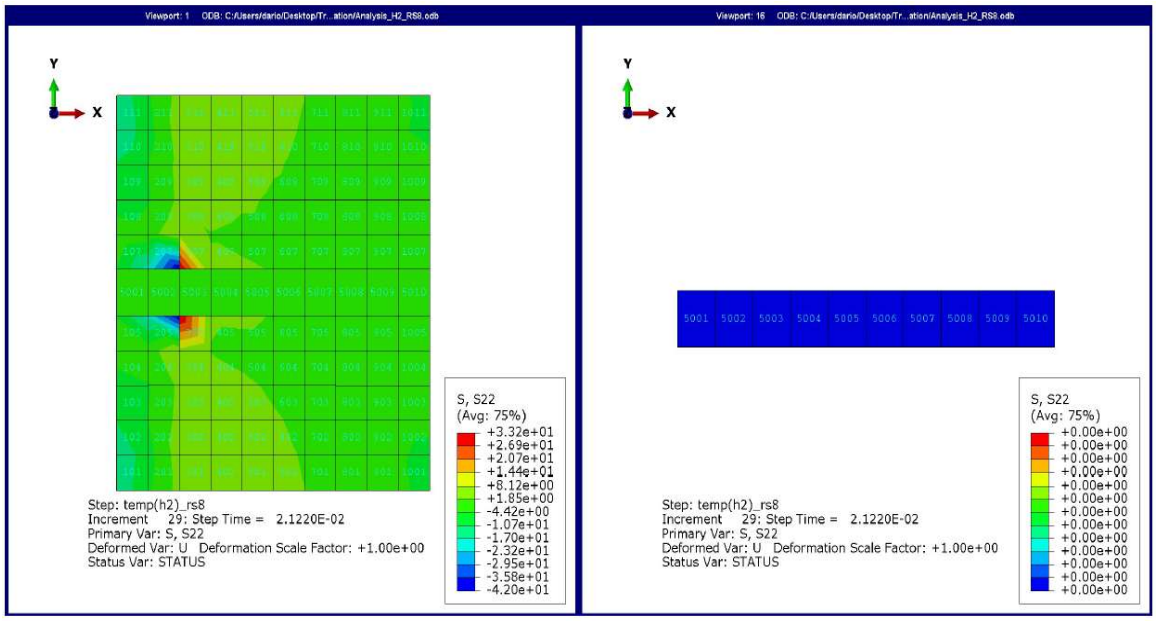

Figure 3-18: Simulation with Dynamic Hydrogen Coverage: Uniaxial stress value (S22) and Uniaxial stress value for the cohesive elements when all Cohesive Elements are fully degraded

In conclusion and as indicated in Figure 3-17 and Figure 3-18 the hydrogen is getting diffused completely with the specimen and all the cohesive elements are fully degraded (5.328sec.). As it can be seen in all the above figures, all the cohesive elements are fully degraded having a SDEG of 1.0 and they do not contribute to resistance (S22 = 0MPa). This means that the point representing the status of all the cohesive elements in the stress-strain curve (Figure 3-2) is beyond the point where the grey curve (representative of the cohesive elements saturated of hydrogen $\psi = 1$ and $k = 0.12$) intersect the X-axis. As expected, the above figures also show that saturated concentration of hydrogen is applied to the all the nodes of the cohesive elements showing the correct implementation of the dynamic hydrogen algorithm.

3.4 Dynamic hydrogen coverage modelling and effect

As previously mentioned, the approach simulates the HE problem but also extends to capture and simulate how an aqueous solution infiltrates the material as the crack extends.

In this section, the effect of dynamic hydrogen coverage will be investigated by comparing results obtained in previous cases. The results presented in Figure 3-19 show the difference in

crack propagation behaviours with and without considering dynamic hydrogen coverage. In particular, the degradation of the sample in the second numerical case is estimated to fully develop in approximately 5.5sec. On the other hand, considering the dynamic hydrogen coverage approach the phenomena happens only in less than 2.0 sec. with a difference of more than 150%.

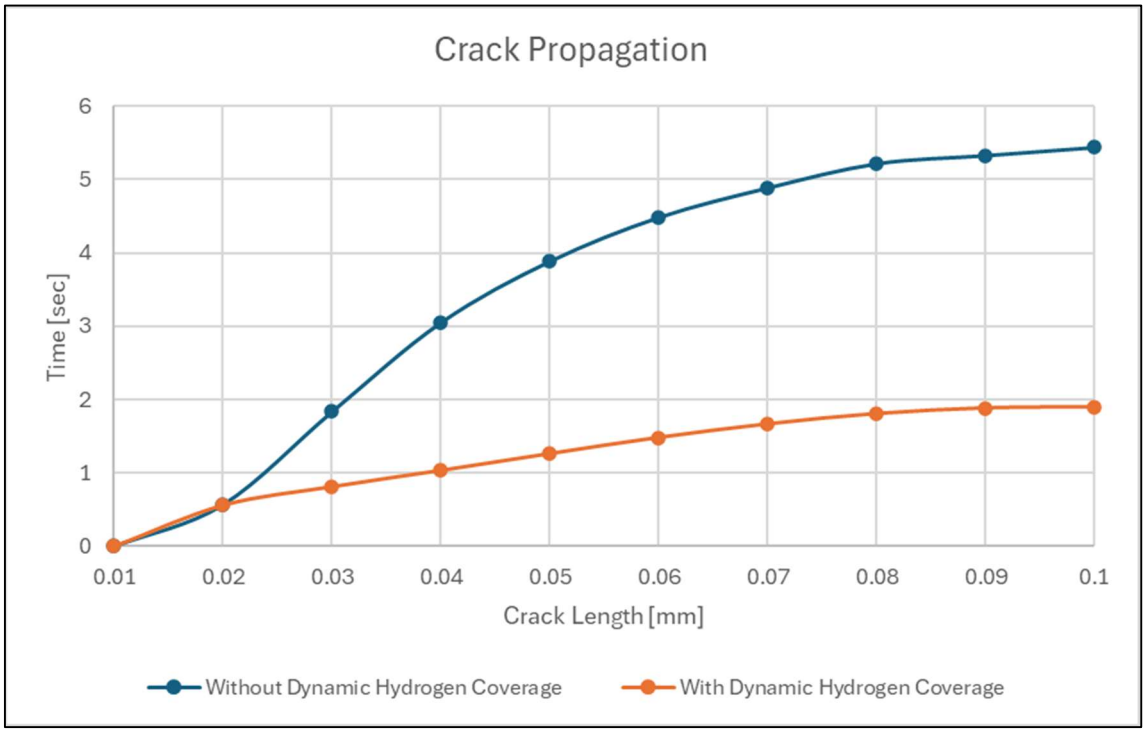

Figure 3-19: Comparison of crack propagation with (red curve) and without (blue curve) dynamic hydrogen coverage approaches

The following considerations can be made:

a) The shape of the curve in absence of dynamic hydrogen coverage is driven and governed by the type of equation representing a typical heat transfer phenomenon (Laplacian formulation).
b) The shape of the curve in presence of dynamic hydrogen coverage is linear, and the slope is almost constant. This is associated to the BC reallocation and the fact the diffusivity parameter (which is constant value) is the main parameter driving the degradation of cohesive elements and most probability characterizing the slope of degradation velocity.

Validity of the proposed approach can be justified by the following: as per above point b.) the crack propagation speed is kept constant by the fact that the BC is changing dynamically and the hydrogen concentration is "following" the next cohesive element (each two consecutive

cohesive elements have the same configuration and distance), diffusivity is a constant value and hence the crack propagation speed should be constant; another proof of validity of the proposed approach is the fact that cohesive element having ID 5002 is degraded at the same time between the 2(two) analysis.

Generically quantify (generalize) the difference between the crack propagation speed between the two approaches may be quite difficult, because this depends on diffusivity coefficient adopted and was not the target for this study. In particular, it is expected that the higher will be the diffusivity coefficient, both curves Figure 3-19 should be lower and the crack propagation phenomenon should develop more rapidly. The interest for this validation case was to prove that the introduced numerical algorithm provides results correct from numerical perspective.

In the next chapters, numerical studies and comparison with experimental data are presented, those studies will confirm validity of the proposed approach.

4 Model with Effect of Elasticity

4.1 Model Definition

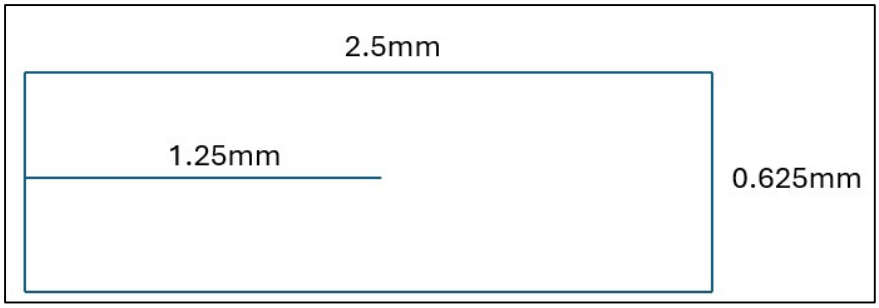

Figure 4-1: Considered Specimen Geometry

The 2-Dimensional (2D) numerical model shown in Figure 4-1 has been utilised to conduct simulations of hydrogen embrittlement in AISI 4340 steel and compared the outcomes with experimental findings from initiation time tests and crack-growth-rate tests as per [124] and [125]. As presented in the above Figure 4-1 and in accordance with [126], the 2D plate dimensions are specified as length (L) = 2.5mm, height (h) = 0.625mm and crack length (L_{crack}) = 1.25mm.

The vertical displacement-controlled load is applied at a designed magnitude to produce a specific, constant stress intensity factor (SIF) at the crack tip. This initial SIF is kept below the material's fracture toughness to ensure the specimen deforms without initiating crack propagation. Table 4-1 provides the five predefined SIF values along with their corresponding displacement loads (u) to be applied and the specimen extremities (bottom and top nodes).

Table 4-1: Relationship between: SIF [$MPa\sqrt{m}$] vs. u [mm] as per Ref. [126]

SIF [$MPa\sqrt{m}$]	u [mm]
13.7	1.148×10^{-3}
20.6	1.725×10^{-3}
27.5	2.303×10^{-3}
34.3	2.873×10^{-3}
41.2	3.451×10^{-3}

It is important to note that, along with the vertical enforced displacement, a consistent saturated layer of hydrogen coverage is maintained at the crack tip only. In accordance to [126], the material AISI 4340 has been considered by assuming a perfect elastic behaviour having a Young's Modulus E of 210,000 MPa, Poisson's Ratio ϑ of 0.3, diffusivity D_L of 0.00253mm^2/s, and fracture toughness of K_{IC} = 58.4$MPa\sqrt{m}$. The specimen has been modelled adopting a uniform rectangular mesh of 0.005x0.005mm across both directions of the entire specimen. In this study the TSL curves which describe the degradation of the CZM due to increase in hydrogen concentration have been calculated in accordance to [126], and specific curves are shown in Figure 3-2 (please refer to above Section 3.1) and relevant parameters have been implemented.

In this first example, due to steel material being assumed as having a perfect elastic behaviour, the component associated with the plastic deformation is considered to be negligible ($\varepsilon_p = 0$), and hence, $C_T = 0$, and $C = C_L$.

4.2 Analysis of Hydrogen Embrittlement Without Considering Dynamic Coverage Contribution

The numerical analysis of the hydrogen embrittlement process begins with a purely mechanical step. As expected, no crack propagation occurs during this stage. In the second step, a saturated hydrogen concentration is applied at the crack tip, and this concentration remains constant throughout the remainder of the analysis.

Figure 4-2 and Figure 4-3 are related to the Step2 only and present typical distributions of the hydrogen concentration field, along with other key mechanical parameters that indicate the system's response during the simulation. Furthermore, as shown in Figure 4-4, the initial crack

does not propagate following the application of the displacement boundary conditions (BC). Instead, hydrogen must first diffuse through the specimen and influence the behaviour of the cohesive elements before crack initiation and subsequent propagation can occur.

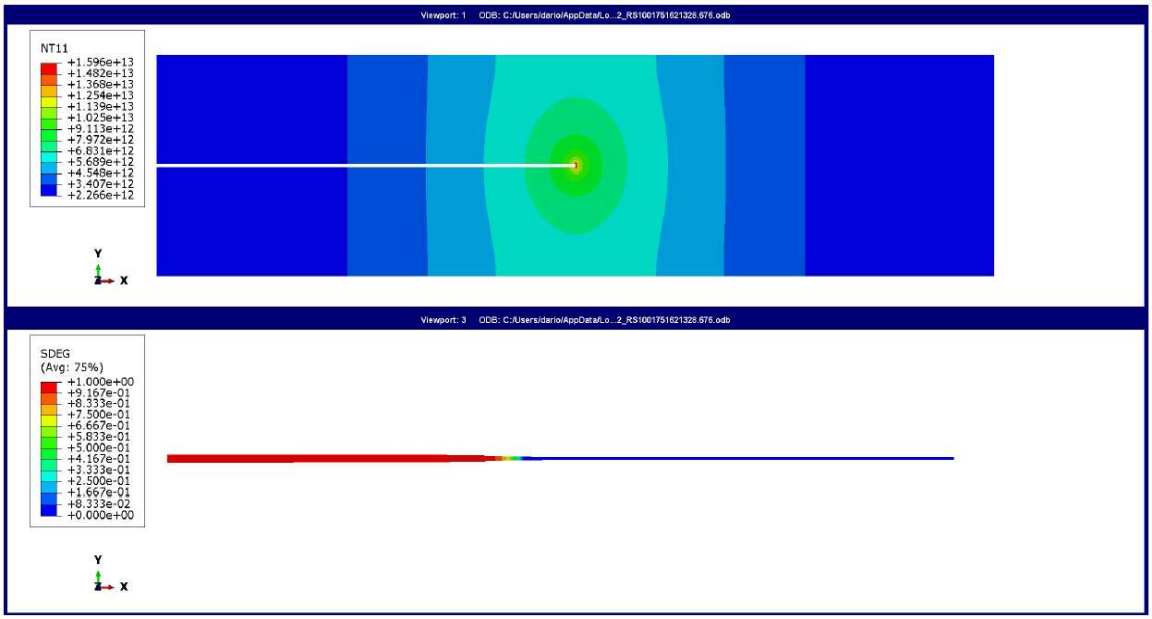

Figure 4-2: Simulation without Dynamic Hydrogen Coverage (SIF41.2): Hydrogen concentration (NT11), cohesive element degradation (SDEG) at approximately 200sec.

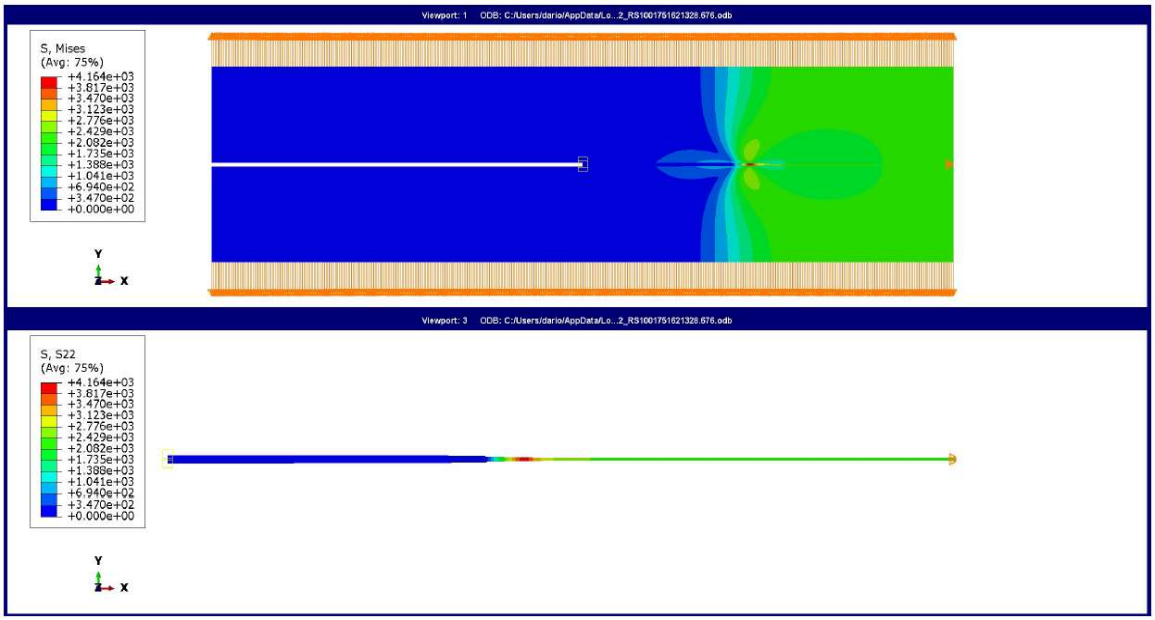

Figure 4-3: Simulation without Dynamic Hydrogen Coverage (SIF41.2): Von Mises Stress (S, Mises), cohesive element stress Y axis direction (S22) at approximately 200sec.

Therefore, the analysis requires degradation in CZM (due to increase in hydrogen concentration) to obtain crack propagation and extension. Figure 4-4 shows the crack length evolution function of the SIF.

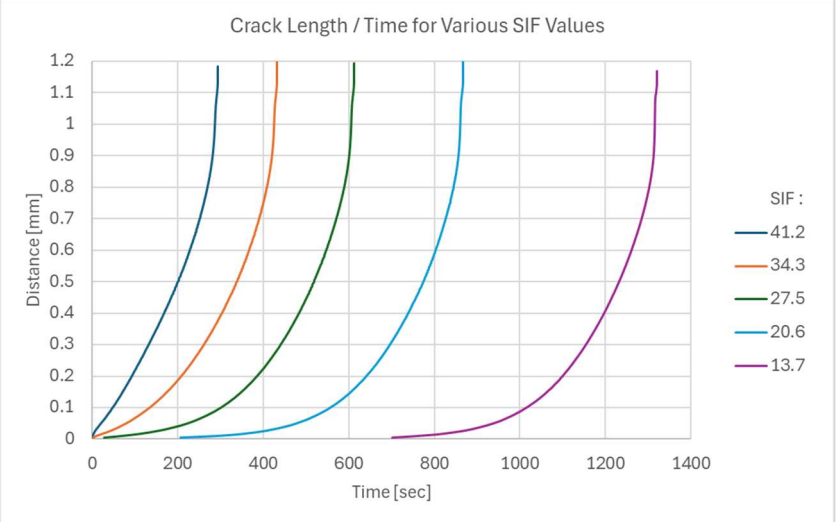

Figure 4-4: Crack length evolution as the time progresses for the applied loading and corresponding SIF

Several simulations have been carried out also to validate the correct applicability of the boundary conditions (BCs), the cohesive elements viscosity parameters and the influence of the TSL shape in the overall behaviour of the analysis.

To substantiate the above statement, the numerical convergence of fracture problems in presence of cohesive elements can result a challenging exercise due to numerical instability associated to the solution of the differential equation in presence of a crack propagation problem. To overcome the above-mentioned problem the utilisation of viscous regularization has been implemented. It is important to clarify that a small value of the viscosity parameter (small compared to the characteristic time increment) has been introduced. This small viscosity usually helps improve the rate of convergence of the model in the softening regime without compromising results and has been calculated through a trial error process. In relation to the TSL shape a comparison analysis has been performed by considering a trapezoidal TSL as shown in Figure 4-5:

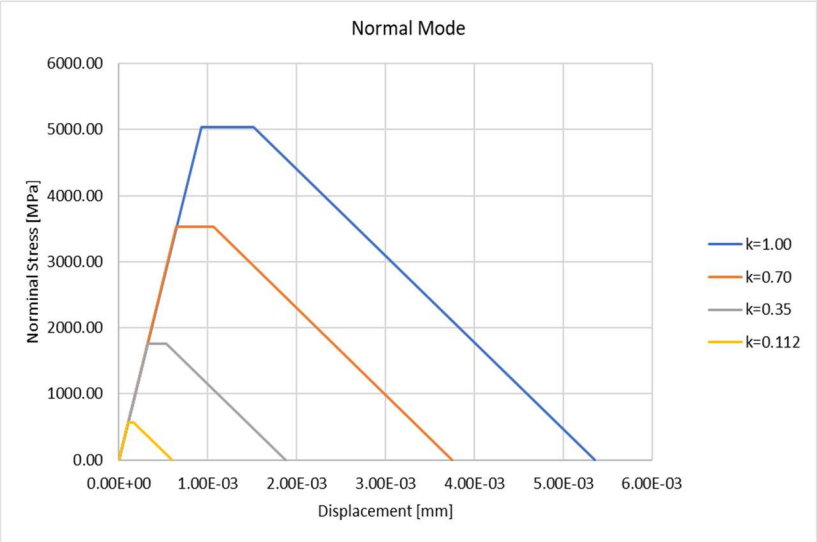

Figure 4-5: Trapezoidal TSL curves for different hydrogen concentration values

As it can be seen in Figure 4-6, for a specific SIF of 41.2, the following different analysis have been performed: CaseA – Yellow (base case analysis), CaseB – Green (Numerical Viscosity to the cohesive elements of 0.001), CaseC – Green (X-Axis BCs applied at cohesive elements), CaseD – Brown (Trapezoidal TSL as per Figure 4-5). All the analyses show similar crack propagation which indicates the correct implementation of the numerical viscosity and BCs, and also the independency of the mechanical problem from the specific adopted TSL curve.

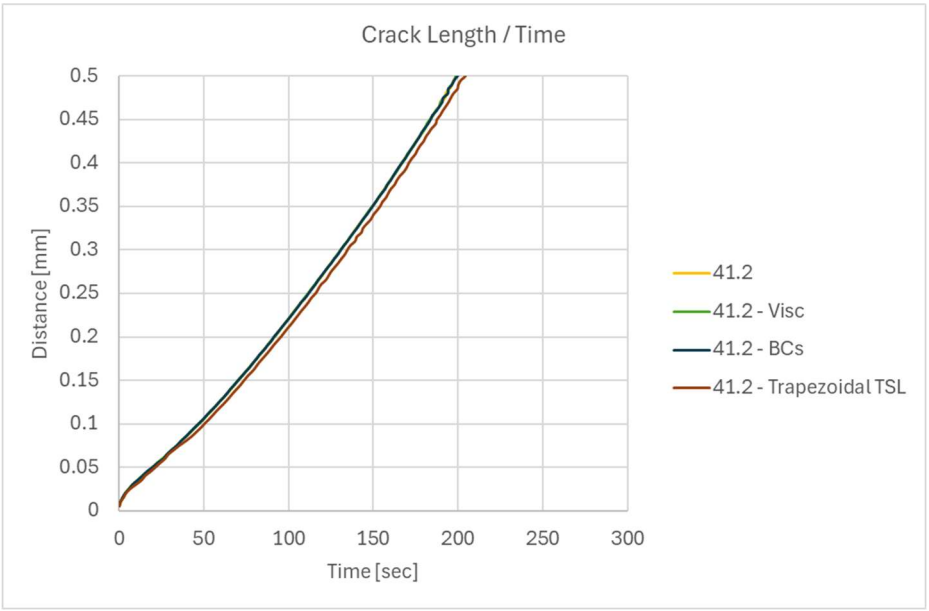

Figure 4-6: Crack length evolution as the time progresses for an SIF of 41.2 and in presence of Numerical Viscosity parameter of 0.001, different BCs and considering the Trapezoidal TSL as Figure 4-5.

In conclusion, the selected viscosity parameter for the cohesive elements (0.001 as identified in [127]), the applied BCs and the triangular shaped TSL do not provide any significant influence of the overall system.

4.3 Analysis of Hydrogen Embrittlement Considering Dynamic Coverage Contribution

This section examines the effect of hydrogen diffusion within the specimen by considering dynamic hydrogen coverage conditions.

As per [128], one of main novelties introduced in this study is the introduction of a numerical procedure for ABAQUS which proposes to simulate the impact associated to an aqueous solution infiltrates the material as the crack extends.

In particular, when the computation code ABAQUS evaluates that a specific cohesive element (type COH2D4T) is fully degraded (SDEG = 1.0 for both integration points), writes externally a new text file which includes the input script for a new analysis and terminate the specific step and analysis. As mentioned, the new ABAQUS input file is generated as output by a FORTRAN subroutine in ABAQUS and includes the entire script for a new analysis step, in the analysis step the Boundary conditions will reflect the hydrogen coverage to the newly formed crack surfaces. The new input file is then executed by ABAQUS as restart file, and will initiate the analysis from the last step and iteration from the previous analysis.

In Figure 4-7, an example of the Hydrogen Dynamic Coverage Numerical Procedure is illustrated. The hydrogen saturated concentration value is initially applied to nodes identified as Node11 and Node21 of Cohesive Element 5001. The hydrogen is than getting diffused within the specimen and the cohesive elements fracture toughness reduced due to the presence of "diffusing" hydrogen. Once the cohesive element degradation SDEG reaches a value of 1.0 for both the integration points IP11 and IP12 of Cohesive Element 5001, then the cohesive element itself (5001) is fully degraded, and the ABAQUS software is required to update the BC associated hydrogen saturated concentration. To this extent and to automate the process, the created FORTRAN Subroutine calls ABAQUS software to exit the FEA analysis, however before exiting the analysis a new ABAQUS input file is generated (automatically by the FORTARN script). This new generated file includes the entire script for a new analysis step, in the analysis step the Boundary conditions will reflect the hydrogen coverage to the newly formed crack surfaces (in this example Node11 and Node21 but also Node12 and Node22). The analysis is then re-launched by a batch file.

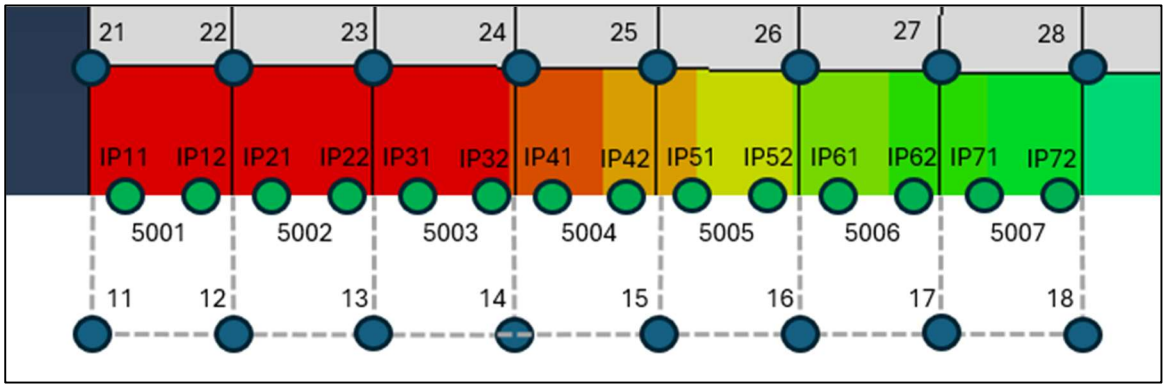

Figure 4-7: Hydrogen Dynamic Coverage Numerical Procedure Example

The physical relevance for to the proposed boundary condition is associated to the real-life condition when a possible internal/external protective coating layer is damaged and cannot act as barrier for hydrogen (this can happen for subsea pipeline when the base line pipe material is left for several years in environment reach of hydrogen like seawater). In this case the hydrogen will become in contact with base line pipe material triggering a hydrogen embrittlement phenomenon.

Figure 4-8 and Figure 4-9 provide a representation of the Finite Element Analysis model, the hydrogen concentration, the Von Mises stress field, the transverse stress (s22), and the degradation of cohesive elements. As mentioned earlier, the initial crack does not tend to propagate after the application of the displacement Boundary Conditions (BCs). Instead it is necessary for the hydrogen to diffuse within the specimen and impact the performance of the cohesive element for crack to initiate and propagate within the specimen.

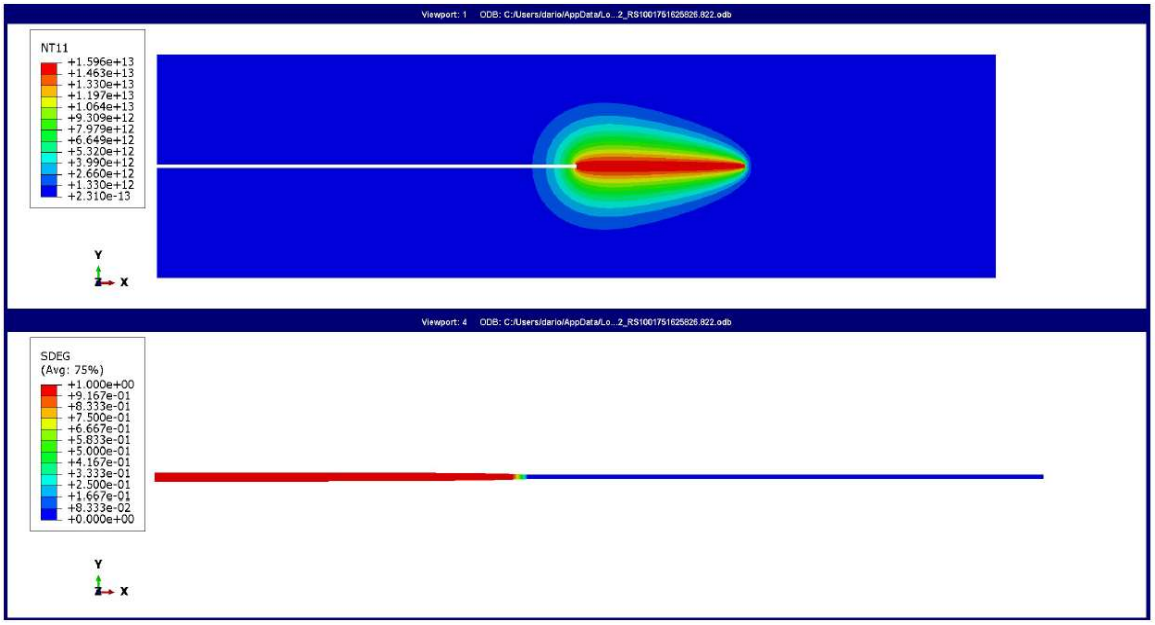

Figure 4-8: Simulation with Dynamic Hydrogen Coverage (SIF41.2): Hydrogen concentration (NT11), cohesive element degradation (SDEG) at approximately 3sec.

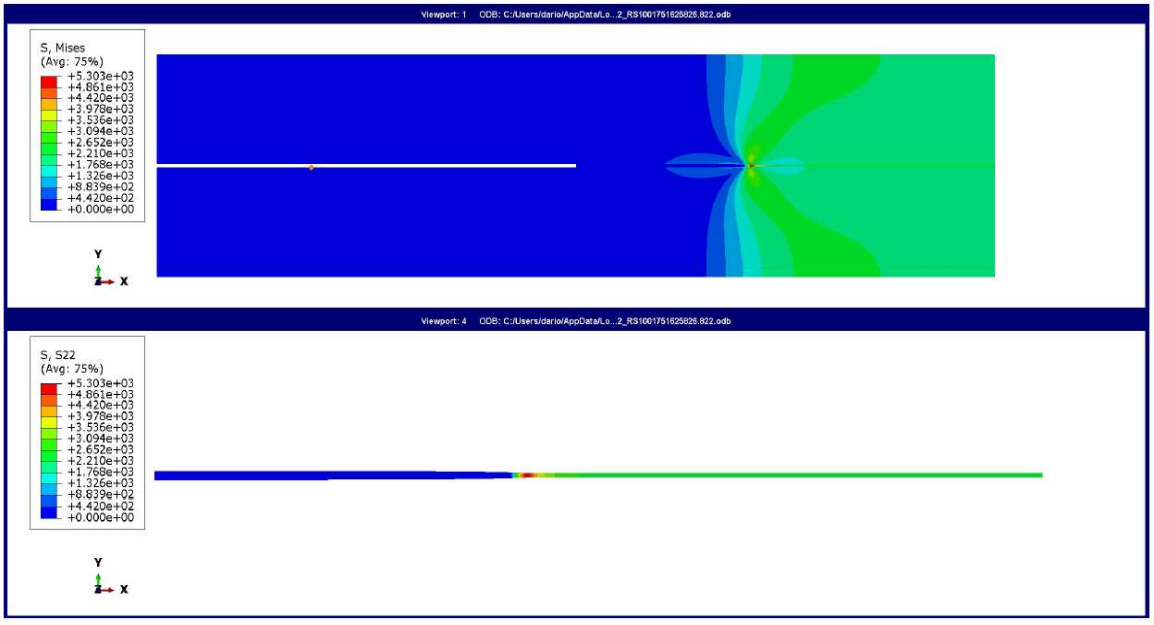

Figure 4-9: Simulation with Dynamic Hydrogen Coverage (SIF41.2): Von Mises Stress (S, Mises), cohesive element stress Y axis direction (S22) at approximately 3sec.

As it can been seen in Figure 4-8 the boundary condition for hydrogen coverage shifts dynamically as the crack propagates and saturated hydrogen concentration (1.596×10^{13} atoms/mm²) is applied where cohesive elements have completely degraded (SDEG = 1.00) and no longer contribute to the specimen's resistance. This gives a clear indication regarding how the cohesive elements degraded and simulate the crack opening, once the cohesive element has been degraded, the BC are reapplied to new opening surface. Unlike the previous scenario, hydrogen spreads inward from the crack tip, causing cohesive zone model (CZM) degradation at a varying rate (depending from the SIF). Additionally, hydrogen migration follows the crack path, diffusing predominantly toward the rear of the sample rather than the front.

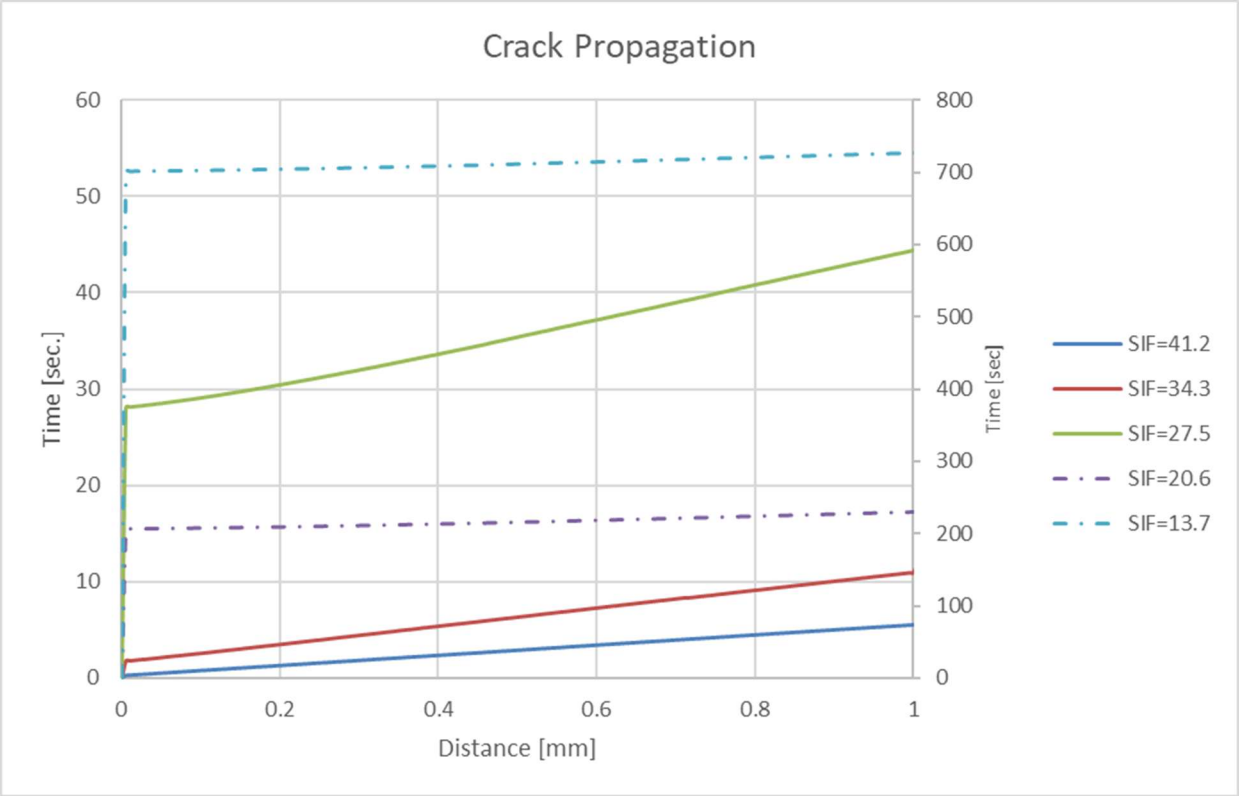

Figure 4-10: Simulation with Dynamic Hydrogen Coverage: Crack propagation length Vs Time. Results with SIF 13.7 and 20.6 are referred to Y-Axis on the right

Figure 4-10 shows the crack length evolution function of the SIF in presence of dynamic hydrogen coverage. To help the reader understanding the phenomenon, results with SIF 13.7 and 20.6 are referred to Y-Axis on the right. It is important to note that the present study is not interested in assessing the intake of hydrogen and crack initiation, the study is intended to address the influence of SIF and hydrogen into the change of slope, and the effect of hydrogen concentration to be able to initiate and propagate of crack at constant applied displacement.

As per comparison with Figure 4-4, Figure 4-10 shows the crack length evolution function of the SIF in presence of dynamic hydrogen coverage. It is clear that the fracture propagation behaviour is strictly associated to the implementation (or not) of the dynamic hydrogen coverage. In particular, without the implementation of dynamic hydrogen coverage the fracture propagation phenomena can be represented by a quadratic/parabolic function. On the other hand, in presence of dynamic coverage and as per Figure 4-10 crack propagation can be represented as a linear function of the fracture length vs. the time (after the crack has been initiated).

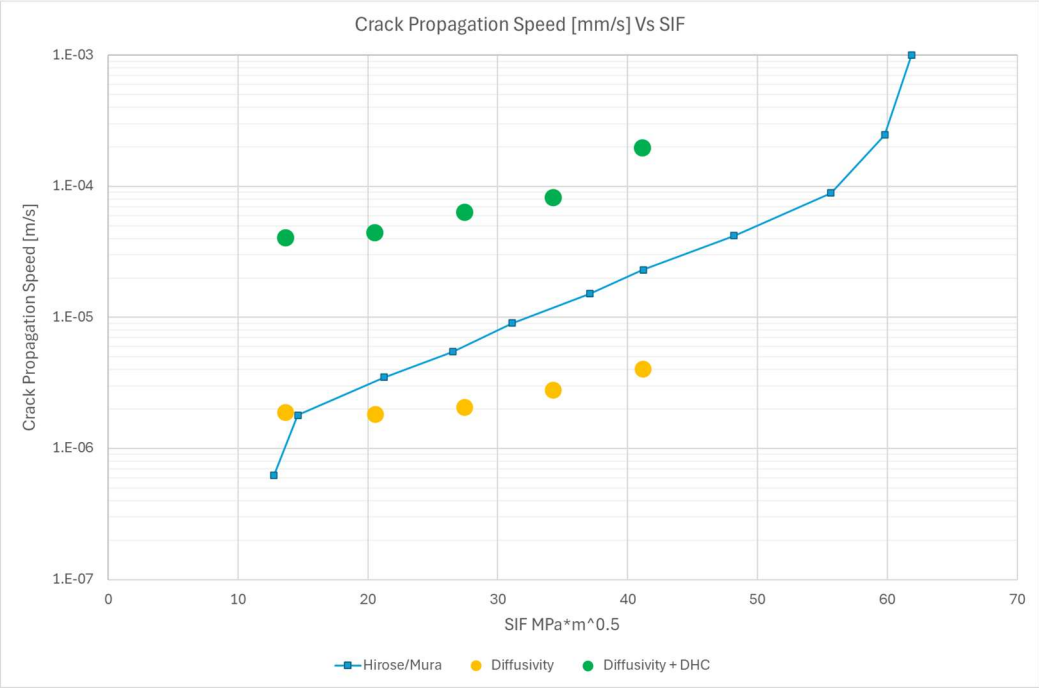

Figure 4-11: Crack Propagation Speed: Comparison of calculated crack-growth rates from numerical simulations [without considering dynamic hydrogen coverage (yellow circles) vs. considering dynamic coverage (green circles)] and experimental data of Hirose and Mura [[124] and [125]] over a range of applied stress-intensity factors.

Above Figure 4-11 shows the comparison between the present model with and without dynamic hydrogen coverage and experiments in [[124] and [125]] concerning the relationship between the crack propagation speed (logarithmic scale) and the stress intensity factor for all five loading conditions (SIFs). The speed of the crack is calculated for every simulation as the ratio of the crack's total propagation length to its propagation time.

As discussed in previous sections, the proposed model can simulate crack propagation in hydrogen-rich environments using both standard elements and elements with dynamic

hydrogen coverage. In both cases with or without dynamic hydrogen coverage, crack propagation primarily depends on the material's fracture toughness value rather than the Traction Separation Law's shape.

Figure 4-11 highlights the key advantage of incorporating dynamic hydrogen coverage. Specifically, the results clearly indicate the constant risk of underestimating the crack propagation speed if the hydrogen dynamic coverage is excluded in the analysis as expected. For the analysis which include the hydrogen dynamic coverage the numerical results tend to have a conservative approximation of the experimental data. However, some differences may be associated to different reasons such as variation in material properties, the mechanism of the hydrogen trapping, and the granular microstructure.

5 Model with the Effect of Plasticity

In general terms, the mechanical behavior and in particular the material work hardening associated to materials utilized in presence of hydrogen can be characterized by means of an isotropic hardening power law as:

$$\sigma_f = \sigma_y \left(1 + \frac{E\varepsilon^p}{\sigma_y}\right)^N \tag{21}$$

where E is Young's Modulus, $0 \leq N \leq 1$, is the coefficient of hardening, ε^p is the material plastic strain, and σ_y is the yield stress of the material. Note that for a coefficient of hardening equal to 0 (zero) the material behaviour can be defined as linear elastoplastic (or linear elastic-perfectly plastic). In this case the material behaves linearly in the elastic range, and the inelastic region of the stress-strain diagram is idealized as a straight line.

5.1 Model Definition

To assess the impact of the plasticity only on the numerical analysis, the same geometry described in the Section 4.1 has been considered and shown in Figure 5-1

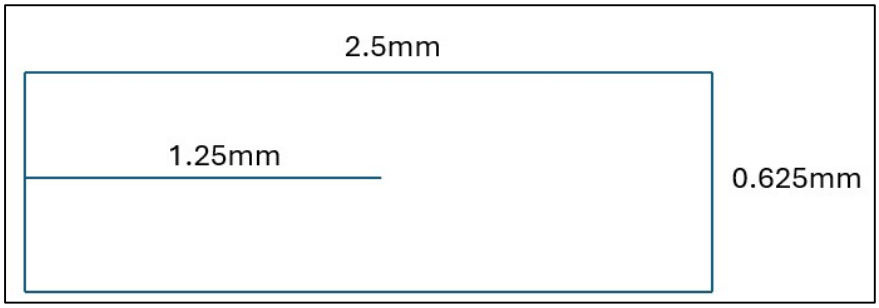

Figure 5-1: Considered Specimen Geometry

Sensitivities have been performed considering the same mechanical properties proposed in Section 4.1 and the following parameters are specified as yield stress, σ_y= 1000MPa, elastic modulus, E = 210,000 MPa, and hardening parameter, N as 0.80 and 0.60.

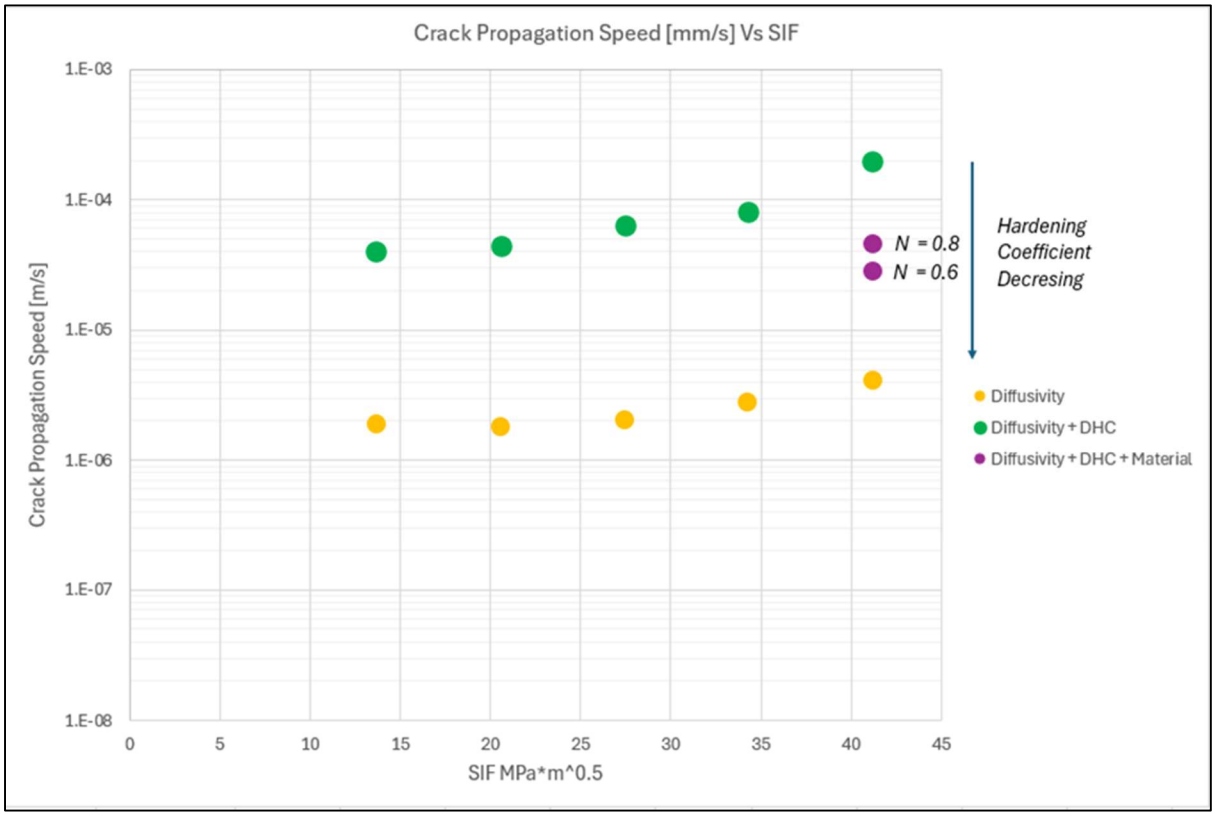

Figure 5-2: Crack Propagation Speed: Comparison of calculated crack-growth rates from numerical simulations [without considering dynamic hydrogen coverage (yellow circles), considering dynamic coverage (green circles)] and hardening coefficients (N = 0.6 and 0.8) for an SIF of 41.2.

Figure 5-2 provides evidence that the implementation of the correct material hardening law has a significant influence on the crack propagation speed. In particular, for a loading corresponding to a particular SIF, a higher hardening coefficient leads higher crack propagation rate and vice versa. This can be justified by considering that for a fixed value of displacement applied to both sample extremities, the material characterised by a more elevated plastic behaviour (smaller hardening coefficient N) will deform largely transmitting a smaller stress component to the cohesive elements. This will inevitably lead to a slower crack propagation speed.

5.2 Numerical Analysis

5.2.1 Calibration

To compare the outcomes with experimental findings from initiation time tests and crack-growth-rate tests as per [124] and [125] [48], a further refinement of the numerical simulations presented in Section 4 has been performed implementing the finding of experimental stress-tensile curves.

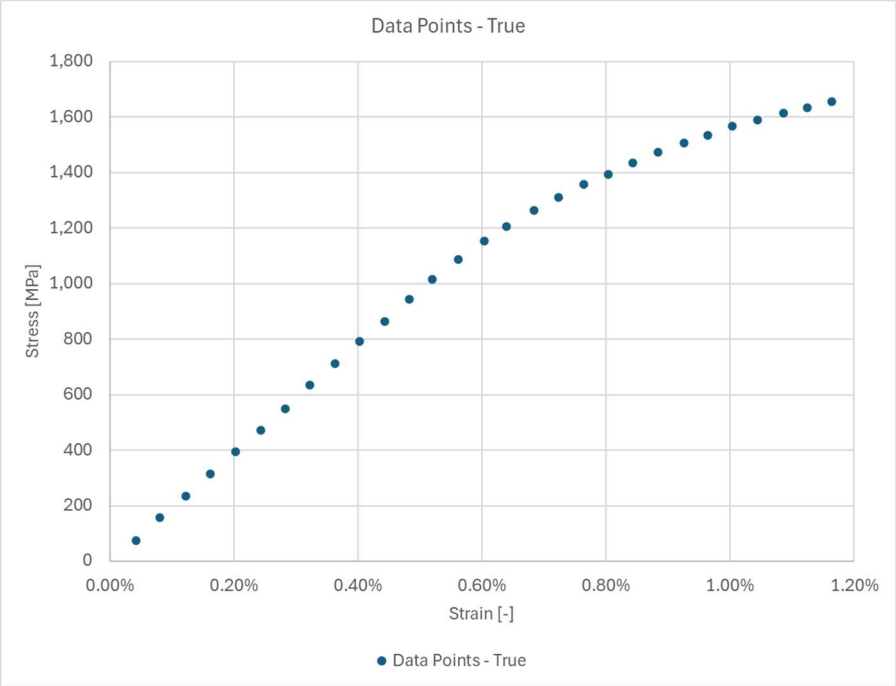

Figure 5-3: Experimental values associated to AISI 4340 alloy steel stress-strain tensile curve for a Specified Ultimate Tensile Strength - Ftu = 1800 MPa [129].

In accordance to [129], Figure 5-3 provides the stress-strain tensile experimental points related to AISI 4340 alloy steel having a Specified Ultimate Tensile Strength - Ftu = 1800 MPa. A calibration exercise has been conducted to derive the various isotropic hardening power law coefficients associated to (21) and has derived the following coefficients:

- σ_y equals to 950MPa
- N is the coefficient of hardening equals to 0.95; and
- Young's Modulus E of 175,000 MPa

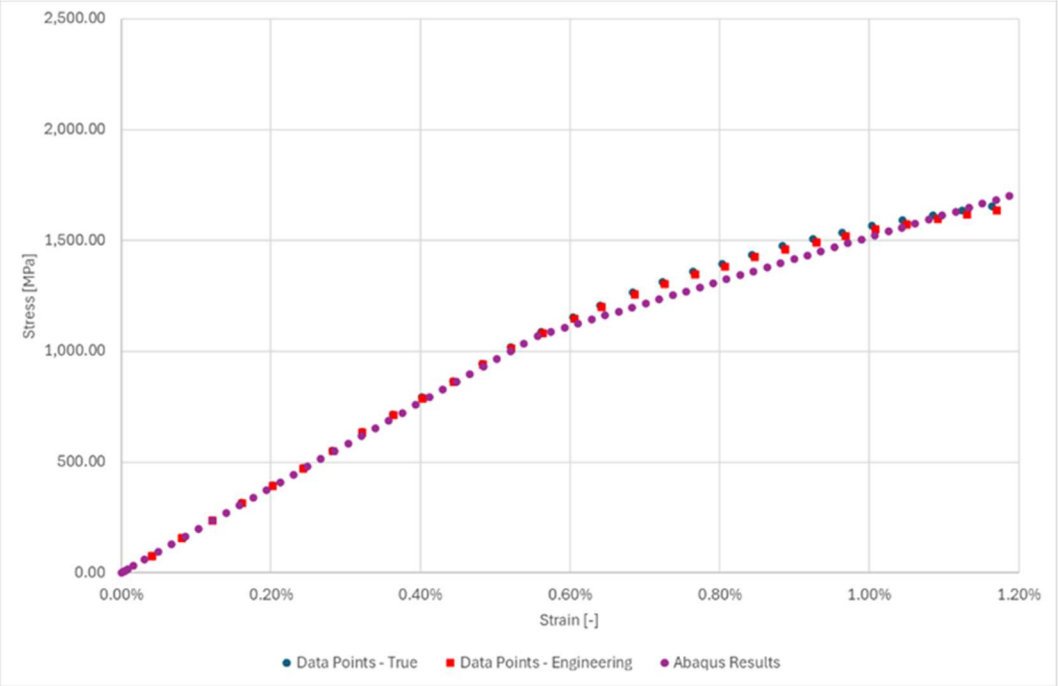

Figure 5-4: Calibration of AISI 4340 alloy steel stress-strain tensile curve for a Specified Ultimate Tensile Strength - Ftu = 1800 MPa [129].

Figure 5-4 shows the good approximation between the ABAQUS Stress Output and the experimental results reported within [129].

5.2.2 Results, Consideration and Conclusions

Figure 5-5 shows the comparison between the model with and without dynamic hydrogen coverage including implementation of characteristic AISI 4340 alloy steel stress-strain tensile curve and experiments data in [[124] and [125]] . In particular, the relationship between the crack propagation speed (logarithmic scale) and the stress intensity factor for all five loading conditions (SIFs) is presented in Figure 5-5 and the speed of the crack is calculated for every simulation as the ratio of the crack's total propagation length to its propagation time.

Comparison between the results reported within Figure 5-5 highlights not only the key advantage of incorporating dynamic hydrogen coverage, but also the importance of the current implementation of characteristic AISI 4340 alloy steel stress-strain tensile curve. Specifically, the results clearly indicate the constant risk of overestimating the crack propagation speed if the characteristic AISI 4340 alloy steel stress-strain tensile curve is excluded from the analysis as expected.

However as already described with Section 4, for the analysis which includes the hydrogen dynamic coverage, and independently from implementation of the specific AISI 4340 alloy

steel stress-strain tensile curve, the numerical results tend to have a conservative approximation of the experimental data. However, some differences again may be associated to different reasons such as the mechanism of the hydrogen trapping and the granular microstructure which will be discussed in the following sections.

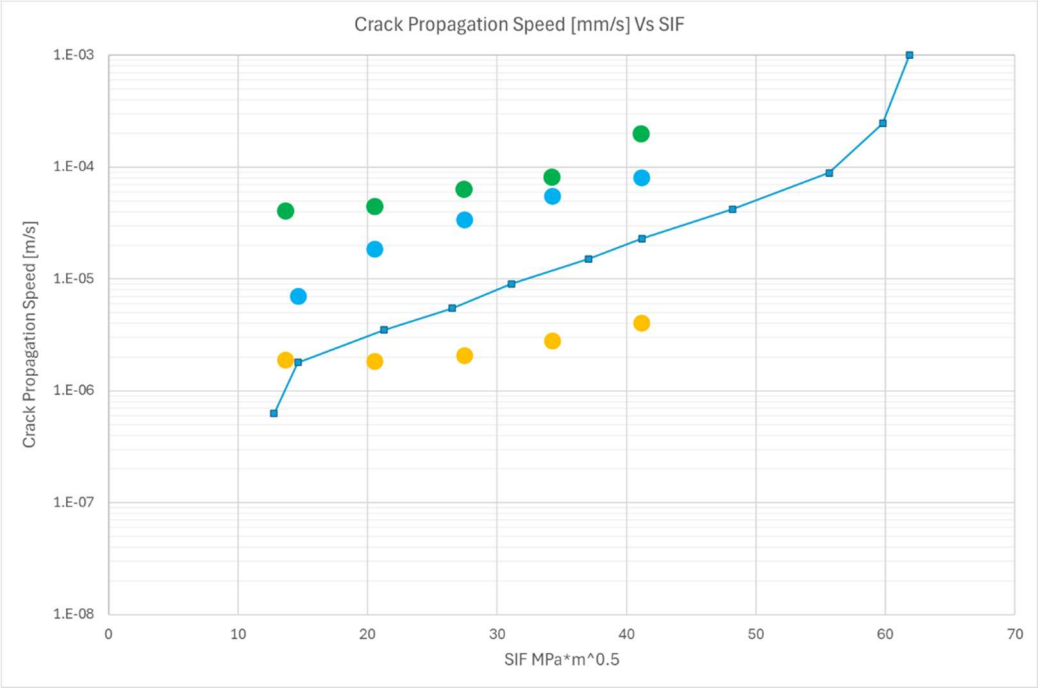

Figure 5-5: Crack Propagation Speed: Comparison of calculated crack-growth rates from numerical simulations [without considering dynamic hydrogen coverage (yellow circles), considering dynamic coverage (green circles)], considering specific AISI 4340 alloy steel stress-strain tensile curve] and experimental data of Hirose and Mura [[124] and [125]] over a range of applied stress-intensity factors.

Note that the current analysis does not include the possibility of modelling the trapping concentration of hydrogen. The present analysis is only intended to provide an indication of the impact of the steel material plasticity on the crack propagation speed without implementing the contribution due to hydrogen trapping.

6 Model with Lattice and Trapping Component

6.1 Hydrogen transportation

We deal with transport of diluted species; that is, the concentration of hydrogen is small compared to the concentration of the metal solvent. As a rule of thumb, a mixture containing several species can be considered dilute when the concentration of the solvent is more than 90% mol. Hydrogen atoms occupy normal interstitial lattice sites (NILS) and additionally can reside at trapping sites such as interfaces or dislocations. It is assumed that traps are isolated (i.e., do not form an extended network). Hence, hydrogen transport between trap sites is by lattice diffusion.

6.1.1 Hydrogen lattice solubility

In the literature two different but equivalent definitions of the lattice hydrogen concentration C_L can be found and these are described below.

6.1.1.1 Approach 1: N_L is the density of solvent atoms

In accordance to [50] the hydrogen concentration in normal interstitial lattice sites could be defined as:

$$C_L = N_L \beta \theta_L \tag{22}$$

where N_L denotes the density of the host metal lattice measured in solvent atoms per unit volume, β is the number of hydrogen atoms that can reside in each lattice site/atom, and θ_L is the lattice occupancy fraction ($0 < \theta_L < 1$).

In simple terms, N_L (units of atoms Fe/m^3 in steel) is the amount of metal atoms per unit volume, β (units of atoms H/atoms Fe) is the amount of hydrogen atoms that correspond to each metal atom, and θ_L (dimensionless) denotes the amount of these hydrogen sites that have been actually occupied by hydrogen atoms (which is small, $\theta_L << 1$, as we are dealing with diluted species). Consequently, the concentration is given in atoms H/m^3 (other typical units are wppm or mol H/m^3). Thus, both β and N_L are material properties (related to the metal solvent) and θ_L (and consequently C_L) depends on the environment and the diffusion of hydrogen. If V_M is the molar volume of the host lattice expressed in units of volume per lattice mole, one can write:

$$N_L = \frac{N_A}{V_M} = \frac{N_A}{M_M/\rho_M} = \frac{N_A \rho_M}{M_M} \tag{23}$$

where $N_A = 6.022 \times 10^{23}$ atoms per mole is Avogadro's number. As depicted in (23), the molar volume is equal to the molar mass/atomic weight divided by the density $V_M = M_M/\rho_M$. In the case of iron at 293 K, the density is equal to $\rho_M = 7.87 \times 10^3$ kg/m^3 and the atomic weight is $M_M = 55.8 \times 10^{-3}$ kg/mol. This necessarily implies

$$N_L = \frac{N_A \rho_M}{M_M} = 8.46 \times 10^{28} \ [\mathrm{at/m^3}] \tag{24}$$

and one should note that β is typically taken to be equal to 6, as indirect evidence indicates tetrahedral site occupancy rather than octahedral site occupancy at room temperature in α-iron. For FCC iron, β = 1 is usually assumed, resulting from the more favourable octahedral site occupancy (β = 2 for tetrahedral).

6.1.1.2 Approach 2: N_L is the density of lattice sites

Alternatively, as per [51], the lattice hydrogen concentration can be defined as:

$$C_L = N_L \theta_L \tag{25}$$

where N_L denotes the number of lattice sites per unit volume. Accordingly, in BCC (body centered cubic) iron where β = 6, it can be evaluated as:

$$N_L = \frac{\beta N_A \rho_M}{M_M} = 5.1 \times 10^{29} \ [\mathrm{sites/m^3}] \tag{26}$$

In the present numerical implementation, we follow the second approach.

6.1.2 Trapped hydrogen concentration

We have seen that hydrogen dissolved in metals can be divided into two groups: the lattice hydrogen, which moves freely through the lattice, or the trapping hydrogen, which is trapped in microstructural defects such as dislocations, grain boundaries, voids, carbides and interfaces. These traps can be reversible or irreversible, and can also be classified as saturable or unsaturable. Reversible traps are those that can immobilize and release hydrogen while irreversible traps are those that absorb hydrogen and prevent it from escaping. However, one should note that the term irreversible is not fundamentally correct but rather pragmatic, as leakage can always take place for a sufficiently long timescale or a sufficiently high temperature. Assuming Oriani's equilibrium (see below), there is a relationship between the occupancy of traps and the lattice hydrogen concentration based on the trap binding energy, W_B.

We will consider the case of multiple traps. Thus, the hydrogen concentration in the *i*th type of trapping site can be defined as:

$$C_T^{(i)} = \theta_T^{(i)} \alpha^{(i)} N_T^{(i)} \tag{27}$$

where N_T is the number of traps per unit volume, α is the number of atom sites per trap, and θ_T is the trap occupancy (again, $0 < \theta_T < 1$). Hence, αN_T is the number of trapping sites per unit volume. In some studies, [51], α is specified as 1 (one hydrogen site per trap) while others consider larger values (e.g., $\alpha = 6$). These differences are related to the concept of atom/site and the binding energy. If α denotes the number of sites per trap, then unequivocally $\alpha = 1$ (and N_T tells us how many sites exist). However, α may also denote the number of hydrogen atoms that can be stored in each trap (e.g., in a dislocation $\alpha = 30$). However, not all of those atoms will have the same binding energy, so we choose here to adopt $\alpha = 1$ and consider apparent/average binding energies (e.g., $W_B. = -20.2$ kJ/mol for a dislocation). It is also quite common to provide the magnitude of the group αN_T and not each individual component. Accordingly, we re-formulate (27) as:

$$C_T^{(i)} = \theta_T^{(i)} N_T^{(i)} \tag{28}$$

where $N_T = N_T \alpha$ is the trap density (trapping sites per unit volume). The total concentration of hydrogen for a system with n traps then reads:

$$C = C_L + C_T^{(1)} + C_T^{(2)} + \cdots + C_T^{(n)} = C_L + \sum_1^n C_T^{(i)} \tag{29}$$

and accordingly:

$$\frac{\partial C}{\partial t} = \frac{\partial C}{\partial C_L}\frac{\partial C_L}{\partial t} + \sum_i^n \frac{\partial C}{\partial C_T^{(i)}}\frac{\partial C_T^{(i)}}{\partial t} \tag{30}$$

6.1.3 Oriani's equilibrium theory

Oriani's equilibrium theory [18] results in a Fermi-Dirac relation between the occupancy of the *i*th type of trapping sites and the fraction of occupied lattice sites

$$\frac{\theta_T^{(i)}}{1-\theta_T^{(i)}} = \frac{\theta_L}{1-\theta_L} K^{(i)} \tag{31}$$

with $K^{(i)}$ being the equilibrium constant for the *i*th type of trap with binding energy $W_B^{(i)}$ given by:

$$K^{(i)} = \exp\frac{-\Delta W_B^{(i)}}{RT} \tag{32}$$

where the trap binding energy W_B,i.e., the energy required for a hydrogen atom to escape a trap site and move into a lattice site, is inherently negative. And the parameters *R* and *T* respectively represent the gas constant, 8.3144 J mol^{-1} K^{-1}, and the absolute temperature. Oriani's equilibrium theory can be used when the trap filling kinetics are very rapid, which is usually the case. In other words, this equilibrium argument is realistic when the lattice diffusion relaxation times are relatively long compared to the time required to replenish or deplete the traps.

The implications of Oriani's equilibrium can be readily quantified. First, note that (31) can be rewritten as,

$$\frac{1}{\theta_L} = \left(\frac{1}{\theta_T^{(i)}} - 1\right) K^{(i)} + 1 \tag{33}$$

which implies that larger values of K lead to smaller lattice occupancies θ_L, and consequently, a smaller amount of C_L relative to C_T for a fixed total hydrogen concentration C. As shown in (32), the equilibrium constant K increases with (the absolute value of) the binding energy W_B. Hence, deep traps (strong, irreversible) with larger $|W_B|$ will absorb more lattice hydrogen and act as sinks that will slow diffusion. Secondly, note that one can merge (25), (31) and (32) which leads to:

$$\frac{N_L}{C_L} = \left(\frac{1}{\theta_T^{(i)}} - 1\right) \exp\frac{-\Delta W_B^{(i)}}{RT} + 1 \tag{34}$$

and one can accordingly choose representative values of θ_T , and plot C_L versus W_B. We do so in Figure 6-1 by adopting N_L = 5.1 × 10^{29} sites/m^3, which is an appropriate choice for BCC iron, as discussed before.

It is observed that deep traps (high $|W_B|$)

- increase the weight of C_T relative to C_L (i.e., absorb more C than weak traps), and
- get filled at low C_L levels (i.e., if C_L is high, then $\theta_T \approx 1$).

So, as soon as there is hydrogen in the system, the hydrogen atoms will occupy the deep traps, as this is more energetically favourable. These deep traps will get full soon, and the hydrogen will then distribute through the lattice. Examples of deep traps with high binding energies include carbides of alloying elements (W_B = −72 kJ/mol) or grain boundaries (W_B = −48 kJ/mol). In contrast, weaker traps are dislocations, where $|W_B|$ is on the order of 20 kJ/mol. As evident from Figure 6-1, these shallow traps with binding energies larger than −20 kJ/mol are effectively empty then ($\theta_T \approx 0$) unless C_L is very high, on the order of 10 wt ppm (4.68 × 10^{25} at H/m^3) or higher.

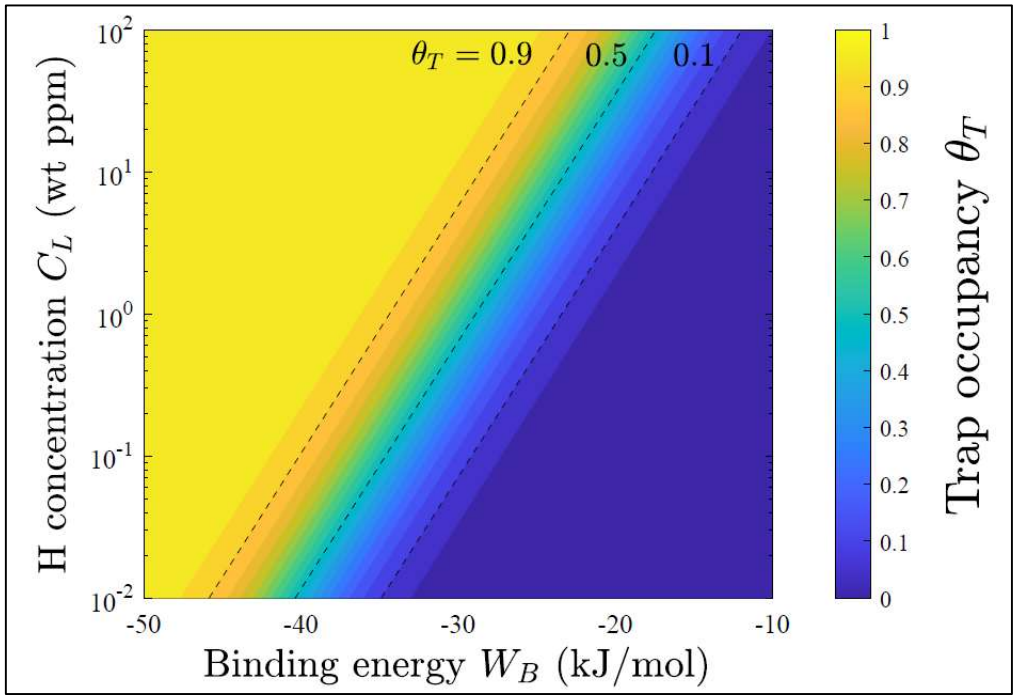

Figure 6-1: Implications of Oriani's equilibrium; sensitivity of the trap occupancy θ_T to the lattice hydrogen concentration C_L and the trap binding energy W_B. Taken from [130].

In many alloys, especially in BCC lattices, conditions of low occupancy $\theta_L << 1$ are usually assumed, because $N_L >> C_L$, such that:

$$\frac{\theta_L}{1-\theta_L} \approx \theta_L \tag{35}$$

and consequently, by considering (25), (27) and (31)

$$C_T^{(i)} = \frac{K^{(i)} C_L N_T^{(i)}/N_L}{1 + C_L K^{(i)}/N_L} = \frac{K^{(i)} C_L N_T^{(i)}}{N_L + C_L K^{(i)}} \tag{36}$$

which characterizes the equilibrium relationship between C_L and C_T in terms of material parameters. Thus, as the temperature increases and C_L decreases, the concentration of hydrogen in traps will decrease for a fixed C_L. Finally, some insight into the process of equilibrium trap-filling at fixed temperature and N_T can be obtained by differentiating the previous equation:

$$\frac{\partial C_T^{(i)}}{\partial C_L} = \frac{C_T^{(i)}\left(1-\theta_T^{(i)}\right)}{C_L} = \frac{K^{(i)} N_L N_T^{(i)}}{(C_L K^{(i)} + N_L)^2} \tag{37}$$

6.1.4 Hydrogen Diffusion

Even though mass concentration is the sought variable, the thermodynamic driving force for diffusion is the chemical potential gradient $\nabla\mu$. The mass flux is related to $\nabla\mu$ via Onsager coefficients L_{ij}, which denote the action of force j on component i; a negative sign indicates that the net movement of i-type hydrogen atoms, i.e. hydrogen flux J_i, occurs from high to low chemical potential regions:

$$J_i = \sum_{j=1}^{n} L_{ij} \nabla \mu_j \tag{38}$$

Considering the lattice sites:

$$J_L = L_{LL} \nabla \mu_L \tag{39}$$

one can develop a generalised model accounting for both lattice and trapping fluxes (see [131]. Here, we follow the common assumption that the mobility between trapping sites is considered close to zero: $D_{TT} \approx 0$, because traps are not connected or because their deep potential energy well prevents hydrogen from diffusing. Hence, only the lattice flux is considered: $J = J_L$ and $\mu = \mu_L$. The Onsager coefficient is related to Einstein's equation of diffusion, such that:

$$L_{LL} = \frac{D_L}{RT} C_L \tag{40}$$

where D_L is the lattice diffusivity, which is understood to be independent of the hydrostatic stress. The chemical potential is given by,

$$\mu = \mu^0 + RTln\frac{\theta_L}{1-\theta_L} - \bar{V}_H\sigma_H \tag{41}$$

where μ_i^0 denotes the chemical potential in the standard state, $\bar{V}_H$ is the partial molar volume of hydrogen in solid solution (an overbar usually denotes a partial molar quantity), and σ_H is the hydrostatic stress.

Substituting (40), (41) into (39) gives:

$$\boldsymbol{J} = -D_L\frac{C_L}{(1-\theta_L)}\left(\frac{\nabla C_L}{C_L} - \frac{\nabla N_L}{N_L}\right) + \frac{D_L}{RT}C_L\bar{V}_H\sigma_H \tag{42}$$

This expression can be simplified by taking into consideration that the interstitial sites concentration is usually assumed to be constant: $\nabla N_L = 0$. Thus,

$$\boldsymbol{J} = -D_L\nabla C_L + \frac{D_L}{RT}C_L\bar{V}_H\sigma_H \tag{43}$$

By analysing (43), it can be observed that the forces driving the mass flux J are ∇C_L and $\nabla\sigma_H$. While $\nabla\sigma_H$can be obtained from coupled stress analysis, ∇C_L has to be solved along (4). It is therefore natural to assume C_L as the primary unknown and compute C_T from (10). The derivative of the flux with respect to the lattice hydrogen concentration can be expressed as:

$$\frac{\partial \boldsymbol{J}}{\partial C_L} = \frac{D_L}{RT}\bar{V}_H\sigma_H \tag{44}$$

6.1.5 Mass Balance

Fluxes, due to the chemical potential gradient, and hydrogen concentrations are related through the requirement of mass conservation. Thus, in a volume V of surface S and outward normal n, the following relationship can be established:

$$\frac{\mathrm{d}}{\mathrm{d}t}\int_V C\mathrm{d}V + \int_S \boldsymbol{J}\cdot\boldsymbol{n}\,\mathrm{d}S = 0 \qquad 1\ (45)$$

where $\mathrm{d}/\mathrm{d}t$ is the time derivative. For simplicity, let us define the total hydrogen concentration in traps as,

$$C_T = C_T^{(1)} + C_T^{(2)} + \cdots + C_T^{(n)} = \sum_1^n C_T^{(i)} \qquad (46)$$

Considering the total concentration as $C = C_L + C_T$, the strong form can be readily obtained by making use of the divergence theorem and noting that 1 (45) must hold for any arbitrary volume,

$$\frac{dC_L}{dt} + \frac{dC_T}{dt} = -\nabla\cdot\boldsymbol{J} \qquad (47)$$

By considering (42) one reaches:

$$\frac{dC_L}{dt} + \frac{dC_T}{dt} = -D_L\nabla^2 C_L + \frac{D_L\bar{V}_H}{RT}\nabla(C_L\nabla\sigma_H) \qquad (48)$$

Using Oriani's equilibrium, an effective diffusion coefficient can be defined as:

$$D_e = D_L\frac{C_L}{C_L + \sum_i C_T^{(i)}\left(1-\theta_T^{(i)}\right)} \qquad (49)$$

and the hydrogen transport equation reads

$$\frac{D_L}{D_e}\frac{\partial C_L}{\partial t} = D_L\nabla^2 C_L - \nabla\left(\frac{D_L C_L}{RT}\bar{V}_H\nabla\sigma_H\right) \tag{50}$$

6.1.6 Dislocation Trapping Schemes

We have assumed so far that the trap density is a material property that remains constant throughout the analysis. This is appropriate for most trap types but not dislocation trapping sites, as the dislocation density evolves with the applied load. Several schemes have been proposed throughout the years to capture how the density of dislocation trap sites, $N_T^{(d)}$, evolves with mechanical straining. Laws have been proposed from a purely phenomenological perspective, relating $N_T^{(d)}$ to macroscopic quantities such as the equivalent plastic strain ε_p, and also from a more mechanistic viewpoint, based on dislocation densities ρ. Relating dislocation trapping schemes to macroscopic quantities is important because microscopic defects strongly influence the overall mechanical behaviour of materials. Dislocation trapping describes how impurities, precipitates, or interfaces hinder the movement of dislocations within a crystal lattice. By connecting these interactions to macroscopic quantities such as strength, hardness, ductility, and fatigue resistance, researchers can predict material performance under real engineering conditions. This relationship also helps in designing alloys with improved reliability and efficiency. Understanding the link between atomic-scale trapping mechanisms and large-scale properties enables scientists to optimize manufacturing processes, reduce material failure, and develop materials for industrial and technological applications.

By assuming one trap site per atomic plane threaded by a dislocation, the following relationship between the dislocation density ρ and the trap site density $N_T^{(d)}$ can be identified:

$$N_T^{(d)} = \frac{1}{b}\,\rho \tag{51}$$

where the pre-factor is the inverse of the Burgers vector. In the case of FCC metals it can be expressed as,

$$N_T^{(d)} = \frac{\sqrt{2}}{a}\,\rho \tag{52}$$

with a being the lattice parameter.

In crystalline materials, plastic deformation occurs mainly through the movement of dislocations along specific crystallographic planes and directions known as slip systems. A slip plane is the plane with the highest atomic density, where atoms are most closely packed and dislocation motion requires the least energy. The slip direction is the direction within that plane along which atoms move most easily. In crystallography, special bracket notations are used to describe these planes and directions. Curly braces such as $\{111\}$ represent a family of equivalent crystallographic planes. For example, in a face-centered cubic (FCC) crystal, the $\{111\}$ planes are the close-packed planes and are the preferred slip planes because they allow easier atomic movement. Angle brackets such as $\langle 110 \rangle$ denote a family of equivalent crystallographic directions. In FCC metals, the $\langle 110 \rangle$ directions are the closest packed directions within the $\{111\}$ planes, making them the preferred slip directions. Together, a slip plane and slip direction form a slip system, written as $\{111\}\langle 110 \rangle$. The number and nature of available slip systems strongly influence the mechanical properties of materials, including ductility, strength, and resistance to deformation under applied stress.

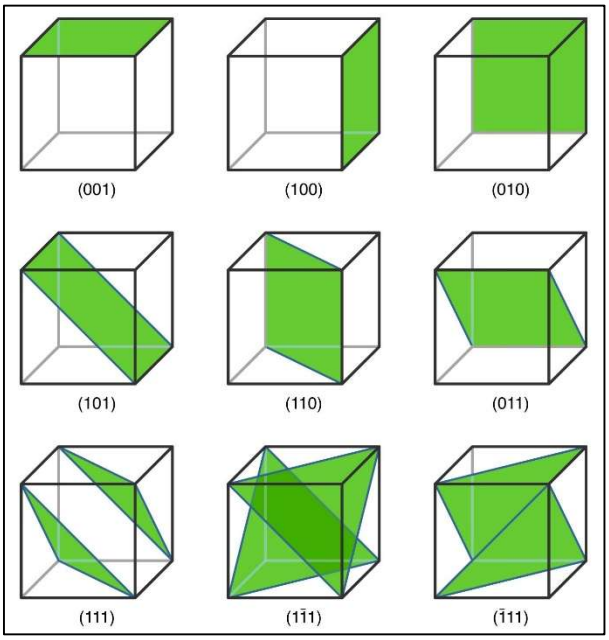

Figure 6-2: Miller indices of planes in a cubic crystal

Slip in FCC crystals occurs along the close packed plane: specifically, the slip plane (plane of greatest atomic density) is of type $\{111\}$ and the slip direction (close-packed direction within the slip plane) is of type $\langle 110 \rangle$. In the BCC case, slip occurs along the plane of shortest Burgers vector as well; however, unlike FCC, there are no truly close-packed planes in the BCC crystal structure. Thus, a slip system in BCC requires heat to activate. Some BCC materials (e.g. α-Fe) can contain up to 48 slip systems. There are six slip planes of type $\{110\}$, each with two

⟨111⟩ directions (12 systems). There are 24 {123} and 12 {112} planes each with one ⟨111⟩ direction (36 systems, for a total of 48). While the {123} and {112} planes are not exactly identical for activation energy to {110}, they are so close in energy that for all intents and purposes they can be treated as identical. For the specific slip plane {110} and direction ⟨111⟩ we have:

$$N_T^{(d)} = \frac{2}{\sqrt{3}a}\,\rho \tag{53}$$

where again the Burgers vector corresponds to the inverse of the prefactor. With these considerations, we proceed to describe some of the most commonly used constitutive laws for determining $N_T^{(d)}$ from the deformation state of the material, all of which have been implemented in the numerical implementation.

6.1.6.1 Kumnick and Johnson & Sofronis and McMeeking

For models based on equivalent plastic strain, such as [65] and [50], empirical formulas are needed to describe the relationship between $N_T^{(d)}$ and ε_p. A widely used model was developed from the early work of Kumnick and Johnson [65] and Sofronis and McMeeking [45]. They performed permeation tests on pure iron exposed to hydrogen gas and observed that the trap density in iron rises quickly at small deformation levels, then continues to increase more slowly as deformation becomes larger.

$$log_{10}N_T = 23.26 - 2.33\exp\left(-5.5\varepsilon_p\right) \tag{54}$$

It immediately follows from (54) that

$$N_T = 10^{23.26-2.33\exp\left(-5.5\varepsilon_p\right)}\ \ [\text{sites/m}^3] \tag{55}$$

Note that the experiments were conducted in uniaxial conditions, implying that the important role of plastic strain gradients in increasing the dislocation density is not accounted for.

6.1.6.2 Kumnick and Johnson & Krom et al.

Krom et al. [51] argue that a factor depending on the strain rate should be included to ensure a correct hydrogen balance. If a one-trap model is considered for simplicity, as the concentration of trapped hydrogen C_T depends on the trap density N_T , and the latter depends on the plastic deformation, by means of the chain rule one reaches:

$$\frac{\partial C_T}{\partial t} = \frac{\partial C_T}{\partial C_L}\frac{\partial C_L}{\partial t} + \frac{\partial C_T}{\partial N_T}\frac{\partial N_T}{\partial \varepsilon_p}\frac{\partial \varepsilon_p}{\partial t} \tag{56}$$

Recalling that

$$\frac{\partial C_T}{\partial C_L} = \frac{C_T(1-\theta_T)}{C_L} \tag{57}$$

and from (27), $\partial C_T/\partial C_L = \theta_T$ can be obtained. Consequently, the partial derivative of the hydrogen concentration in trap sites with respect to time is:

$$\frac{dC_T}{dt} = \frac{C_T(1-\theta_T)}{C_L}\frac{dC_L}{dt} + \theta_T\frac{dN_T}{d\varepsilon_p}\frac{d\varepsilon_p}{dt} \tag{58}$$

The model depicted before can be therefore extended, with (48) being:

$$\left(1 + \frac{C_T(1-\theta_T)}{C_L}\right)\frac{dC_L}{dt} + \theta_T\frac{dN_T}{d\varepsilon_p}\frac{d\varepsilon_p}{dt} = D_L\nabla^2 C_L - \nabla\left(\frac{D_L C_L}{RT}\bar{V}_H\nabla\sigma_H\right) \tag{59}$$

or, by making use of the effective diffusion constant:

$$\frac{D_L}{D_e}\frac{\partial C_L}{\partial t} + \theta_T\frac{dN_T}{d\varepsilon_p}\frac{d\varepsilon_p}{dt} = D_L\nabla^2 C_L - \nabla\left(\frac{D_L C_L}{RT}\bar{V}_H\nabla\sigma_H\right) \tag{60}$$

In a similar manner, we can again use the multivariable chain rule to reformulate (40) as:

$$\frac{\partial C}{\partial t} = \frac{\partial C}{\partial C_L}\frac{dC_L}{dt} + \frac{\partial C}{\partial N_T}\frac{dN_T}{d\varepsilon_p}\frac{\partial \varepsilon_p}{\partial t} \tag{61}$$

The derivative of the total hydrogen concentration with respect to N_T can be readily obtained from (37) as:

$$\frac{\partial C}{\partial N_T} = \frac{\partial C_L + \partial C_T}{\partial N_T} = \frac{KC_L}{KC_L + N_L} \tag{62}$$

And finally note that one should also estimate the term $dN_T/d\varepsilon_p$. The experiments of Kumnick and Johnson [65] were adopted by Krom et al. [51] . Thus, considering (56) one reaches:

$$\frac{dN_T}{d\varepsilon_p} = \frac{12.815}{10^9}\exp\left(-5.5\varepsilon_p\right) 10^{23.26-2.33\exp\left(-5.5\varepsilon_p\right)}\, ln10 =$$

$$= 29.5\exp\left(-5.5\varepsilon_p\right)N_T \tag{63}$$

where we have already taken into consideration that, in our numerical implementation, the units used for N_T are sites/mm^3.

6.1.6.3 Gilman & Dadfarnia et al.

Sofronis and co-workers (see, e.g.: [44] and [58]), have presented a dislocation based relationship, using Eq. (30) and building upon the work of Gilman. The dislocation density, in line length per cubic meter, is related to the plastic strains via:

$$\bar{\rho} = \begin{cases} \bar{\rho}_0 + \gamma\varepsilon_p & for\ \ \varepsilon_p < 0.5 \\ \bar{\rho}_1 & for\ \ \varepsilon_p \geq 0.5 \end{cases}, \tag{64}$$

where $\rho_0 = 10^{10} line\ length/m^3$ denotes the dislocation density for annealed material and $\gamma = 2.0\ x\ 10^{16} line\ length/m^3$. The magnitude of γ is obtained experimentally and differs from other works. A rate-dependent term can also be included as:

$$\frac{\partial C}{\partial t} = \frac{\partial C}{\partial C_L}\frac{dC_L}{dt} + \frac{\partial C}{\partial N_T}\frac{dN_T}{d\rho}\frac{\partial \rho}{\partial t} \tag{65}$$

6.2 Numerical Implementation – UMATHT Subroutine

The numerical implementation is carried on in ABAQUS by means of a UMATHT subroutine. A number of variables must be defined in the subroutine, whose equivalence to heat transfer and mass diffusion variables are defined in Table 7-1.

Table 6-1: Quantities to be defined in the UMATHT Subroutine

UMATHT variable	Heat transfer	Mass Diffusion
U	U^q	C
T	T	C_L
DUDT	$\frac{\partial U^q}{\partial T}$	$\frac{\partial C}{\partial C_L}$
DUDG(NTGRD)	$\frac{\partial U^q}{\partial \nabla T}$	$\frac{\partial C}{\partial \nabla C_L}$
FLUX(NTGRD)	J^q	J
DFDT(NTGRD)	$\frac{\partial J^q}{\partial T}$	$\frac{\partial J}{\partial C_L}$
DFDG(NTGRD,NTGRD)	$\frac{\partial J^q}{\partial \nabla T}$	$\frac{\partial J}{\partial \nabla C_L}$

where the variable **NTGRD** is the number of spatial gradients of temperature. One should note that ∇C_L does not need to be computed, as it is given by ABAQUS to the subroutine through the variable **DTEMDX** (∇T). The subroutine gives as input the following variables at the beginning of the increment: total hydrogen concentration $C(U)$, lattice hydrogen concentration C_L (**TEMP**), and gradient of the lattice hydrogen concentration ∇C_L (**DTEMDX**). Moreover, it provides the incremental lattice hydrogen concentration ΔC_L (**DTEMP**) as well. So, the first step is to work with the current C_L value, which is assigned to a variable **CL**:

```
CL=TEMP+DTEMP
```
(66)

Now, let us consider each term individually. First, we shall define the total hydrogen concentration at the end of the increment, (**U**). This is given by: (recall that $\Delta a = \dot{a}\Delta t$)

$$C(t+\Delta t) = C(t) + \frac{\partial C}{\partial \mathrm{t}}\Delta t = C(t) + \frac{\partial C}{\partial C_L}\frac{\partial C_L}{\partial t}\Delta t + \frac{\partial C}{\partial C_T}\frac{\partial C_T}{\partial t}\Delta \tag{67}$$

which can be expressed as:

U=U+DUDT*DTEMP+DU2 (68)

Here, the variable **DUDT** is addressed below and the variable **DU2** corresponds to the rate-dependent term of the dislocation trapping law. For example, based on the model developed by Krom et al. [51], it can be expressed as:

$$\mathbf{DU2} \equiv \frac{\partial C}{\partial N_T}\frac{dN_T}{d\varepsilon^p}\frac{\partial \varepsilon^p}{\partial t} = \frac{KC_L}{KC_L+N_L} 29.5\exp(-5.5\varepsilon^p) N_T \Delta\varepsilon^p \tag{69}$$

While for the case of Dadfarnia et al. [14] (Section 2.6.3), the variable **DU2** corresponds to the second term in Eq. (44); i.e., considering Eq. (41) and Eq. (43):

$$\mathbf{DU2} \equiv \frac{\partial C}{\partial N_T}\frac{dN_T}{d\varepsilon^p}\frac{\partial \varepsilon^p}{\partial t} = \frac{KC_L}{KC_L+N_L}\frac{1}{b}\gamma\Delta\varepsilon^p \tag{70}$$

And one should be careful with the units, as in (15) the dislocation density is given in m^{-2} but we have chosen to work with mm^{-2} instead. In both dislocation-based or ε^p based dislocation trapping schemes there is an obvious coupling with the mechanical problem. This can be easily addressed in ABAQUS exploiting the fact that the solution-dependent state variables (STATEV) are shared between UMAT and UMATHT subroutines.

Let us consider now the term **DUDT**, which is given by:

$$\frac{\partial C}{\partial C_L} = \frac{\partial C_L}{\partial C_L} + \sum_i \frac{\partial C_T^{(i)}}{C_T} = 1 + \sum_i \frac{C_T^{(i)}(1-\theta_T^{(i)})}{C_L} = \\ = 1 + \sum_i \frac{K^{(i)} N_L N_T^{(i)}}{(K^{(i)} C_L + N_L)^2} \tag{71}$$

which can expressed as:

```
DUDT=1.D0+DUDT2
DUDT2=0.d0
do k1=1, ntraps
 DUDT2=DUDT2+xNt(k1)*xK(k1)*xNl/((xK(k1)*CL+xNl)**2.d0)
end do
```

where **ntraps** is the number of traps, **xNt** $\equiv N_T^{(i)}$, **xK** $\equiv K^{(i)}$ and **xNl** $\equiv N_L$. On the other hand, the term **DUDG**, equivalent to $\partial C/\partial \nabla C_L$, is zero. Each component of the J (**FLUX**) is given by:

$$J = -D_L \nabla C_L + \frac{D_L C_L V_H}{RT} \nabla \sigma_H \tag{72}$$

which can be expressed as:

```
FLUX(i)= - D*DTEMDX(i)+D*CL*Vh*sig(i)/(R*T)
```

where **sig(i)** is the gradient of the hydrostatic stress, $\nabla \sigma_H$, whose computation will be addressed below. Accordingly, the term **DFDT** reads,

$$\frac{\partial J}{\partial C_L} = \frac{D_L V_H}{RT} \nabla \sigma_H \tag{73}$$

which can be expressed as:

```
DFDT(i)=D*Vh*sig(i)/(R*T)
```

and in both the definition of the flux and its derivative, one should be careful with the units when defining the gas constant (**R**). The term $V_H \nabla \sigma_H / RT$ must be non-dimensional. Assuming

that the stresses are given in MPa (N/mm^2), then R = 8314 Nmm/(mol K). Note that the gas constant also appears in the calculation of the equilibrium constant K. This means that the binding energy, WB, should be given in units of Nmm/mol (1 kJ/mol = 10^6 Nmm/mol).

Finally, it remains to define the variable DFDG, which is given as follows:

$$\frac{\partial J}{\partial \nabla C_L} = -D_L \boldsymbol{I} \tag{74}$$

which can be expressed as:

DFDG(i,i)=-D

with $\boldsymbol{I}$ being the identity matrix, as only the diagonal terms in $\partial J/\partial \nabla C_L$ are non-zero (only $\nabla^x C_L$ is involved in the x component of $\boldsymbol{J}$).

In addition to the quantities required by ABAQUS, one might choose to define additional quantities for visualisation such as the trapped hydrogen concentration as per Eq. (15).

6.2.1 General case: θ_L not much smaller than 1

Note that, if the approximation $\theta_L << 1$ cannot be assumed (e.g., FCC metals), then Eq. (14) does not hold. Consequently, the computation of **DUDT** will be affected and should be reformulated as:

$$\frac{\partial C}{\partial C_L} = \frac{\partial C_L}{\partial C_L} + \sum_i \frac{\partial C_T^{(i)}}{C_T} = 1 + \sum_i \frac{C_T^{(i)}(1-\theta_T^{(i)})}{C_L} = \\ = 1 + \sum_i \frac{K^{(i)} N_L N_T^{(i)}}{\left((K^{(i)}-1)C_L + N_L\right)^2} \tag{75}$$

which can be expressed as:

```
DUDT=1.D0+DUDT2
DUDT2=0.d0
do k1=1, ntraps
 DUDT2=DUDT2+xNt(k1)*xK(k1)*xNl/(((xK(k1)-1)*CL+xNl)**2.d0)
end do
```

Also, for computing the concentration in each trap $C_T^{(i)}$, one cannot longer use Eq. (15), which should instead read:

$$C_T^{(i)} = \frac{C_L N_T^{(i)} K^{(i)}}{N_L + (K^{(i)} - 1) C_L} \tag{76}$$

6.3 Numerical Implementation – Gradient of Hydrostatic Stress

The mechanical behaviour of the solid will be described using conventional plasticity and will not be elaborated here. A user material (UMAT) subroutine is used, which corresponds to the UMAT for power law hardening plasticity. What will be addressed here is the computation of hydrostatic stress gradient, a feature specific to this problem and thus not be available in the original UMAT subroutine.

The quantity $\nabla\sigma_H$ is computed using a relatively simple differentiation scheme at the element level. First, the magnitude of σ_H is interpolated through its values at the Gauss points in the isoperimetric space and afterwards $\nabla\sigma_H$ is computed by differentiation of the shape functions. This procedure is outlined below for the particular case of a plane strain quadrilateral element with 8 nodes and 4 integration points. Extension to other types of elements can be performed in a relatively straightforward manner.

The hydrostatic stress values within the element can be readily obtained from its values at the Gauss integration points $(\sigma_H)_k$:

$$\sigma_H = \sum_{k=1}^{4} N_K^i(x, y)(\sigma_H)_k \tag{77}$$

where $N_K^i(x, y)$ is the interpolation function in global coordinates. By performing the classic isoparametric mapping, the coordinate transformation is:

$$x = \sum_{k=1}^{4} N_k(\xi, \eta) x_k \tag{78}$$

$$y = \sum_{k=1}^{4} N_k(\xi, \eta) y_k \tag{79}$$

where $N_k(\xi, \eta)$ is the shape function vector. For convenience, the interpolation function in local coordinates takes the same form as the shape functions and (77) becomes:

$$\sigma_H = \sum_{k=1}^{4} N_k(\xi, \eta)(\sigma_H)_k \tag{80}$$

Accordingly, linear shape functions are adopted:

$$N_i = \frac{1}{4}(1 + \xi_i \xi)(1 + \eta_i \eta) \tag{81}$$

with ξ_i and $\eta_i$denoting the integration point coordinates in the isoparametric space. The differentiation of the shape functions readily follows:

$$\frac{\partial N_i}{\partial \xi} = \frac{1}{4}\xi_i(1 + \eta_i \eta) \tag{82}$$

$$\frac{\partial N_i}{\partial \eta} = \frac{1}{4}\eta_i(1 + \xi_i \xi) \tag{83}$$

which, by means of the chain rule, can be easily converted to the global coordinate system,

$$\begin{bmatrix} \frac{\partial N_k}{\partial x} \\ \frac{\partial N_k}{\partial y} \end{bmatrix} = J^{-1} \begin{bmatrix} \frac{\partial N_k}{\partial \xi} \\ \frac{\partial N_k}{\partial \eta} \end{bmatrix} \tag{84}$$

with J being the Jacobian matrix:

$$J = \frac{\partial(x,y)}{\partial(\xi,\eta)} = \begin{bmatrix} \frac{\partial x}{\partial \xi} & \frac{\partial y}{\partial \xi} \\ \frac{\partial x}{\partial \eta} & \frac{\partial y}{\partial \eta} \end{bmatrix} = \begin{bmatrix} \sum_{k=1}^{4} \frac{\partial N_k}{\partial \xi} x_k & \sum_{k=1}^{4} \frac{\partial N_k}{\partial \xi} y_k \\ \sum_{k=1}^{4} \frac{\partial N_k}{\partial \eta} x_k & \sum_{k=1}^{4} \frac{\partial N_k}{\partial \eta} y_k \end{bmatrix} \tag{85}$$

The hydrostatic stress gradient $\nabla\sigma_H$ is then computed as:

$$(\nabla\sigma_H)_x = \sum_{k=1}^{4} \frac{\partial N_i}{\partial x} (\sigma_H)_i \tag{86}$$

$$(\nabla\sigma_H)_y = \sum_{k=1}^{4} \frac{\partial N_i}{\partial y} (\sigma_H)_i \tag{87}$$

These operations take place inside of the UMAT subroutine and the information is then passed to the UMATHT. Both UMAT and UMATHT are integration point level subroutines, but it is obvious that the computation of $\nabla\sigma_H$ requires access to the magnitude of σ_H in all the integration points of the elements. This is achieved by means of a Fortran module (the modern version of common blocks).

6.4 Dislocation model

In analogy with [58], the dislocation-based model by Sofronis and co-workers is used in this numerical model as per following:

- Dislocations, with a binding energy of $W_B^{(d)} = 20.2 \times \frac{10^6 Nmm}{mol}$ and a trap density given by the dislocation-based scheme of Sofronis and co-workers;
- Grain boundaries, with $W_B^{(c)} = 58.6 \times \frac{10^6 Nmm}{mol}$ and $N_T^{(c)} = 8.464 \times \frac{10^{13} sites}{mm^3}$;

- Carbides, with $W_B^{(c)} = 11.5 \times \frac{10^6 Nmm}{mol}$ and $N_T^{(c)} = 8.464 \times \frac{10^{17} sites}{mm^3}$.

6.5 Numerical Analysis

6.5.1 Calibration and Dislocation Model

To compare the outcomes with experimental findings from initiation time tests and crack-growth-rate tests as per [124] and [125] [48], a further refinement of the numerical simulations presented in Section 4 and Section 5 is done in this section.

In accordance to [129], above reported Figure 5-3 provides the stress-strain tensile experimental points related to AISI 4340 alloy steel having a Specified Ultimate Tensile Strength - Ftu = 1800 MPa. As reported in Section 5.2.1 a calibration exercise has been conducted to derive the various isotropic hardening power law coefficients associated to (21) and the following coefficients are obtained:

- σ_y is equal to 950MPa;
- $N$is the coefficient of hardening equal to 0.95; and
- Young's Modulus E of 175,000 MPa

Above Figure 5-4 shows the good approximation between the ABAQUS Stress Output and the experimental results reported within [129].

6.5.2 Results, Consideration and Conclusions

Below Figure 6-3 shows the comparison between the model with dynamic hydrogen coverage, implementation of characteristic AISI 4340 alloy steel stress-strain tensile curve, implementation of different hydrogen trapping dislocation mechanisms, and experimental data given in [[124] and [125]].

In particular, the relationship between the crack propagation speed (logarithmic scale) and the stress intensity factor for all five loading conditions (SIFs) is presented in below Figure 6-3 and the speed of the crack is calculated for every simulation as the ratio of the crack's total propagation length to its propagation time.

Finally comparison between the results reported within Figure 6-3 highlights not only the key advantage of incorporating dynamic hydrogen coverage, but also the importance of the current implementation of characteristic AISI 4340 alloy steel stress-strain tensile curve and the various trapping dislocation mechanisms. Specifically, the results clearly indicate the better correlation between the experimental results and the numerical model in presence of dynamic hydrogen coverage, the specific stress-strain tensile curve and the trapping mechanisms.

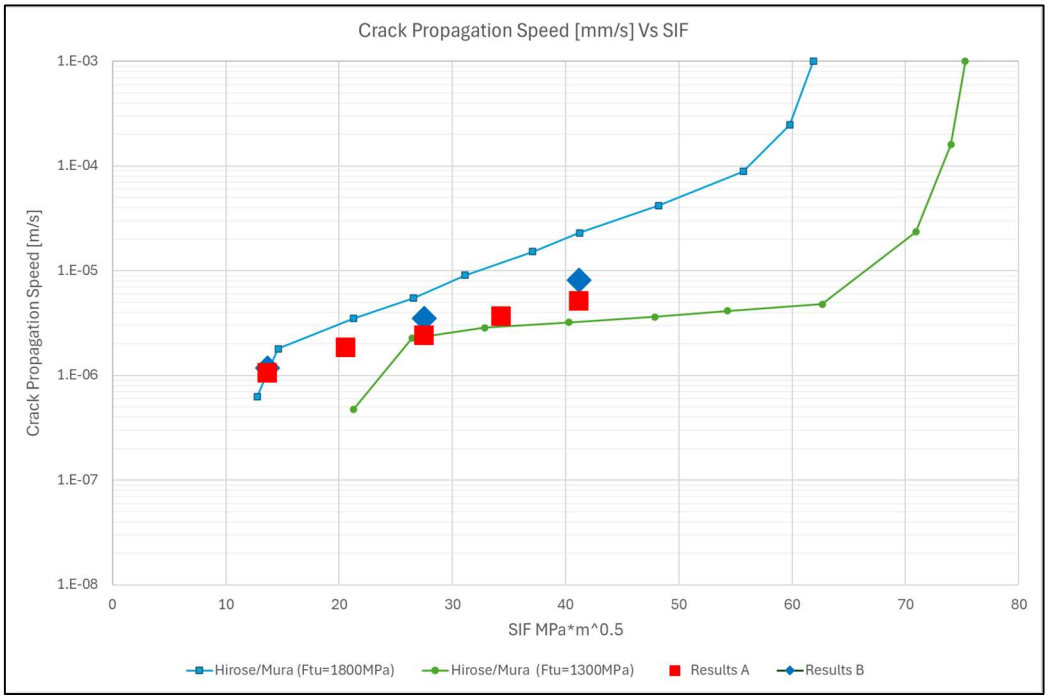

Figure 6-3: Crack Propagation Speed: Comparison of calculated crack-growth rates from numerical simulations [numerical analysis with a mesh 0.0025x0.0025 (blue diamond results – Results B) and 0.005x0.005mm (red square results – Results A)] considering specific AISI 4340 alloy steel stress-strain tensile curve] and experimental data of Hirose and Mura [[124] and [125]] over a range of applied stress-intensity factors (ftu).

The study accounts for the heat treatment due to the isotropic hardening power law coefficients which have been established/derived based on the selected stress-strain curve (related to an Ftu=1800 MPa in accordance to [124] and [125]]

Additional numerical sensitivities have also been performed to capture any beneficial effects due to the mesh sizing. Figure 5-8 shows that analyses with a more refined mesh (having size of 0.0025x0.0025mm instead of 0.005x0.005mm) produce numerical results which are closer to the experimental results associated to an Ftu=1800 MPa, however the computation price associated to this exercise is notable and not to be underestimated.

This study case introduces a fully coupled numerical implementation in ABAQUS to simulate hydrogen embrittlement. The proposed framework captures the bidirectional coupling between hydrogen diffusion and mechanical stress-strain fields during crack propagation, leveraging the similarities between mass diffusion and heat transfer equations.

The implementation involves several user subroutines, interconnected via FORTRAN common blocks, integrated into ABAQUS coupled thermal-stress analysis to compute total hydrogen concentration. To be able to correctly evaluate that hydrogen flux, the adopted methodology also estimates the hydrostatic stress gradients.

In conclusion, this analysis study presents an innovative approach for simulating hydrogen-induced stress corrosion cracking (SCC) in a controlled test setting. The results indicate that the developed model reliably forecasts fracture patterns caused by hydrogen embrittlement. Furthermore, the study highlights the critical role of an appropriate traction-separation law (TSL) in capturing dynamic hydrogen distribution within the specimen. The work also reveals that ignoring dynamic hydrogen coverage – a frequent assumption in prior studies – may lead to underestimated crack growth rates.

In conclusion our validation studies on AISI 4340 steel indicate that the model delivers both qualitative and quantitative predictions that align well with experimental results. The strong correlation between the model and experimental data supports the hypothesis that hydrogen-induced decohesion is likely the primary mechanism behind hydrogen-assisted fracture in high-strength steels exposed to aqueous environments. Notably, the model can generate fracture curves typical of environment-assisted cracking, including crack growth rates as a function of stress-intensity factors. To note that the model can be tailored to specific materials through various calibration approaches.

7 Conclusions

7.1 Difficulties and Achievements

One of the main difficulties encountered in modelling hydrogen embrittlement in ABAQUS is accurately capturing the strong coupling between hydrogen diffusion, stress evolution, and material degradation. A particular challenge is the representation of local material hardening, which is not solely a geometrical effect but is primarily associated with the heterogeneous stress and strain fields that develop around microstructural features such as inclusions, grain boundaries, dislocation networks, and crack tips. While geometric discontinuities, such as notches or sharp corners, can intensify stress concentrations and therefore promote local hardening effects, the phenomenon is fundamentally driven by the interaction between plastic deformation and hydrogen accumulation. In finite element simulations, these localized regions experience elevated hydrostatic stresses that attract diffusing hydrogen, leading to a reduction in ductility and fracture resistance. Another important aspect is the apparent contradiction between microscopic and macroscopic behaviour. At the microscopic level, many hydrogen-assisted fracture mechanisms involve significant plastic deformation. Processes such as hydrogen-enhanced localized plasticity (HELP) facilitate dislocation motion, resulting in locally ductile deformation around crack tips. However, when these microscopic processes accumulate throughout the material, the macroscopic response often appears brittle because crack initiation and propagation occur with very limited global plastic strain. Consequently, a component may fail suddenly without exhibiting the large-scale deformation typically associated with ductile failure. This transition from local ductility to global brittleness is one of the most difficult phenomena to reproduce numerically and remains an active area of research. Comparisons with real-life scenarios highlight the practical importance of these modelling challenges. Hydrogen embrittlement has been observed in pipelines, offshore infrastructure, storage vessels, and high-strength steel components intended for hydrogen transport and energy applications. In many cases, components that satisfy conventional design criteria under mechanical loading alone have experienced premature cracking after prolonged exposure to hydrogen-rich environments. Such failures can significantly increase maintenance costs, inspection requirements, and operational risks. Furthermore, the implications extend beyond service life considerations to decommissioning strategies. Assets affected by hydrogen degradation may require earlier replacement or more extensive rehabilitation than originally planned, thereby increasing lifecycle costs. Reliable numerical models developed in ABAQUS can therefore provide valuable insight into damage evolution, support safer design practices, optimize inspection intervals, and inform economic decisions related to asset management and eventual decommissioning. The ability to predict hydrogen-assisted failure with greater confidence is essential for the long-term viability of hydrogen infrastructure and the transition toward a hydrogen-based energy economy.

Conclusions 7

Even though structural integrity problems in corrosive environments often arise due to cyclic loading, modelling efforts have been mainly restricted to monotonic loading conditions. A numerical framework to assess fracture and hydrogen embrittlement by means of a hydrogen-sensitive cohesive formulation under monotonic loading conditions has been developed within a finite strain plasticity setting. This numerical scheme is also enhanced to evaluate non-local plasticity effects on notched specimens by means of a mechanism-based strain gradient plasticity theory in the absence of hydrogen. In addition, hydrogen diffusion towards the fracture process zone has been widely examined by means of a phenomenological strain gradient plasticity formulation. The numerical models have been successfully implemented, validated and used to address several cases of particular interest from the structural integrity perspective.

The numerical framework has been validated through the modelling of cracked and notched specimens under monotonic loading, which is of particular interest to engineering practice. Furthermore, hydrogen diffusion to the crack tip has been thoroughly investigated for both conventional theories. The following achievements must be highlighted:

- A novel hydrogen cohesive zone model, suitable for large deformations, has been presented. The model is able to predict a relevant increase in crack growth rates with hydrogen content in the surrounding environment and decreasing load frequency, in agreement with experimental observations.
- The capacity of the model to capture the sensitivity of fatigue crack growth rates in a hydrogenous environment is investigated, taking into account material properties, constraint conditions and applied loads. This investigation revealed the need to incorporate additional sources of stress elevation, such as gradient-enhanced dislocation hardening, to attain agreement with the experiments.
- The diffusion of hydrogen into the fracture process zone has been modelled considering the influence of plastic strain gradients. The stress fields and hydrogen concentration at the crack front have been characterized within the framework of finite deformation theory, with an in-depth investigation into the relevant implications of geometrically necessary dislocations on hydrogen embrittlement mechanisms.
- The study has been carried out on the influence of geometrically necessary dislocations on the modelling of fracture and fatigue behaviour in notch-type defects. In the first case, the critical fracture load was determined, as well as the influence of the applied remote stress on the crack length under monotonic loading. In the second case, the influence on the crack growth rate under cyclic loads in notched specimens with different geometries was evaluated.
- The study has highlighted the influence associated to hydrogen dynamic coverage. The model is able to predict the influence on the crack growth rates due to hydrogen

content in the surrounding environment and underlined the risk of underestimated the crack growth rates neglecting the above-mentioned mechanism.

7.2 Conclusions

The research work was first oriented toward studying the predictive capacity of the cohesive zone model within linear elasticity and considering plasticity theory in finite deformations to model fracture mechanics problems. Subsequently, the influence of hydrogen-assisted cracking was investigated by means of a phenomenological formulation of the plastic strain gradient theory within the framework of finite deformations and the numerical implementation of Fick's law (incorporating the effect of hydrostatic stress).

Finally, the influence of plastic strain gradients on the failure of notched components has been investigated using the conventional mechanism-based theory and a cohesive zone formulation suitable for both monotonic and cyclic loading. Particularly:

- Numerical analyses of rack propagation reveal a significant increase in the crack growth rate with rising hydrogen content in the environment. This is a consequence of the reduction in fracture energy, as well as with a decrease in the load application frequency. These analyses qualitatively capture the degradation and failure of a wide range of metal alloys in aggressive environments due to static (and potential cyclic) loads.
- The low susceptibility of the crack growth rate to the load application frequency in slow tests necessitates the incorporation of additional stress sources. Since modifying the yield limit, the hardening coefficient, and the constraint conditions is not sufficient, it is suggested that other effects need to be incorporated, such as local hardening due to plastic strain gradients.
- Numerical analysis based on the theory of plastic strain gradients indicates that geometrically necessary dislocations promote local material hardening. This leads to stress fields that are significantly elevated compared to the predictions of conventional plasticity, at a distance of several micrometres beyond the crack tip.
- The incorporation of plastic strain gradient theories into the structural integrity assessment of notched components shows that geometrically necessary dislocations are responsible for a substantial reduction in ductility and the maximum load-bearing capacity under monotonic loading conditions.

The successful outcomes of this PhD thesis demonstrate the critical importance of incorporating both dynamic hydrogen coverage and plastic strain gradient theories into the modelling of hydrogen embrittlement, while also validating the effectiveness of cohesive zone models for predicting hydrogen environmentally assisted crack propagation. The findings of this research are highly encouraging, as the proposed numerical framework provides a strong foundation for the development of a new generation of predictive modelling tools.

The success criterion is clearly identified from Figure 6-3, where the number analysis results show excellent alignment with the reported experimental data/results.

Beyond its scientific contribution, this thesis addresses a challenge of major industrial relevance: the reliable prediction of hydrogen embrittlement in structural components, particularly within the energy sector. By advancing the understanding and predictive capability of hydrogen-assisted failure, this work contributes to overcoming current barriers to the safe and cost-effective use of high-strength steels in hydrogen transport and storage infrastructure.

7.3 Future Work

The results highlight the need to adopt plastic strain gradient theories for modelling hydrogen-assisted cracking, with particular significance for hydrogen-assisted fatigue modelling. The goal is to obtain numerical predictions that faithfully reproduce experimental results.

Consequently, future work is outlined, focusing primarily on the development of a generalized numerical framework that incorporates:

(i) a cohesive model sensitive to hydrogen concentration and cyclic damage,

(ii) a description of mechanical behaviour characterized by plastic strain gradient theories, and

(iii) a characterization of hydrogen trapped in dislocations associated with plastic strain and its gradients.

This numerical framework must be used to predict both the initiation and propagation of damage in cracked and notched components, with special emphasis on the following aspects:

- Investigating Trapped Hydrogen: Delving deeper into the role of hydrogen trapped in reversible traps and its correlation with geometrically necessary dislocations is particularly interesting. This is due to the high density of dislocations in the crack vicinity caused by plastic strain gradients. The modelling of other types of microstructural traps is also of interest.
- Modelling Ductile Damage Mechanisms: Although hydrogen-assisted fracture appears brittle at the macroscopic level, it is particularly important to investigate microstructural effects in numerical modelling to account for damage mechanisms characteristic of ductile fracture. Therefore, developing a numerical model with a cohesive formulation that considers, at the microscopic level, the growth and coalescence of micro voids—within the framework of the local plasticity mechanism produced by hydrogen at the crack front—and that accounts for the scale effect in micro void growth, could be a particularly attractive topic for future work. The combined modelling of ductile and

brittle fracture mechanisms is of special interest for understanding the influence of hydrogen concentration on the ductile-to-brittle transition.

- Analysing Hydrogen Adsorption: Research into hydrogen adsorption processes, analysing the suitability of the theoretical model used within the developed numerical framework and its correlation with experimental results, seems particularly interesting.

8 References

[1] R. Violette, . E. de Langre and J. Szydlowski, “Computation of vortex-induced vibrations of long structures using a wake oscillator model: Comparison with DNS and experiments,” *Computers and Structures,* vol. 85, p. 1134–1141, 2007.

[2] W. H. Johnson, “On some remarkable changes produced in iron and steel by the action of hydrogen and acids,” *Proc. R. Soc. London,* p. 168–179, 1874.

[3] R. L. S. Thomas, J. R. Scully and R. P. Gangloff, “Internal hydrogen embrittlement of ultrahigh-strength AERMET100 steel,” *Metall. Mater. Trans., vol. 34,* p. 327–44, 2003.

[4] D. Li, R. P. Gangloff and J. R. Scully, “Hydrogen trap states in ultrahigh-strength AerMet 100 steel,” *Metall. Mater. Trans., vol. 35,* p. 849–964, 2004.

[5] R. Ayer and P. Machmeier, “Transmission electron microscopy examination of hardening and toughening phenomena in AerMet100,” *Metall. Mater. Trans., vol. 24,* p. 1943–1955, 1993.

[6] D. Figueroa and M. J. Robinson, “The effects of sacrificial coatings on hydrogen embrittlement and re-embrittlement of ultra high strength steels,” *Corros. Sci., vol. 50,* p. pp. 1066–1079, 2008.

[7] S. Serebrinsky, E. A. Carter and M. Ortiz, “A quantum-mechanically informed continuum model of hydrogen embrittlement,” *J. Mech. Phys. Solids, vol. 52,* p. 2403–2430, 2004.

[8] E. Martínez-Paneda, C. F. Niordson and R. P. Gangloff, “Strain gradient plasticity-based modeling of hydrogen environment assisted cracking,” *Acta materalia, vol. 117,* p. 321–332, 2016..

[9] J. Sanchez, S. F. Lee, M. A. Martin-Rengel, J. Fullea, C. Andrade and J. Ruiz-Hervías, “Measurement of hydrogen and embrittlement of high strength steels,” *steels’, Eng. Fail. Anal., vol. 59,* p. 467–477, 2006.

[10] M. Koyama, M. Rohwerde, C. C. Tasan, A. Bashir, E. Akiyama and K. Takai, "Recent progress in microstructural hydrogen mapping in steels: quantification, kinetic analysis, and multi-scale characterization," *Mater Sci Technol,* vol. 33, no. 13, pp. 1481-96, 2017.

[11] R. P. Gangloff and B. P. Somerday, "Characterisation and analysis of hydrogen embrittlement," in *Gaseous hydrogen embrittlement of materials in energy technologies - Volume1: The problem, its characterisation and effects on particular alloy classes*, Cambridge, Cambridge: Woodhead Publishing, 2012, p. 329–338.

[12] X. Kong, H. Jiang, Y. Lv, W. Xie, S. Lu and D. Xu, "Research Progress on the Hydrogen Embrittlement Resistance Performance of High-Entropy Alloys," *Materials,* vol. 18 (12), no. 2862, p. 34, 2025.

[13] C. A. Zappfe and C. E. Sims, "Hydrogen embrittlement, internal stress and defects in steel," *Trans. Metall. Soc. AIME, vol. 145,* p. 225–271, 1941.

[14] R. P. Gangloff and B. P. Somerday, "Modelling hydrogen embrittlement," in *Gaseous hydrogen embrittlement of materials in energy technologies - Volume 2: Mechanisms, modelling and future developments*, Cambridge, Cambridge: Woodhead Publishing, 2012, p. 207–242.

[15] A. R. Troiano, "The role of hydrogen and other interstitials in the mechanical behaviour of metals," *Trans. ASM, vol. 52,* p. 54–80, 1960.

[16] A. S. Tetelman and W. D. Robertson, "Direct observation and analysis of crack propagation in iron-3% silicon single crystals," *Acta Metallica,* vol. 11, no. 5, pp. 415-426, 1963.

[17] G. G. Hancock and H. H. Johnson, "Hydrogen, oxygen, and subcritical crack growth in a high-strength steel," *Trans. Metall. Soc. AIME, vol. 236, no. 4,* p. 513–516, 1966.

[18] R. Oriani, "The Diffusion and Trapping of Hydrogen in Steel," *Acta Metallurgica 18,* pp. 147 - 157, 1979.

[19] C. S. John and W. W. Gerberich, "Effect of loading mode on hydrogen embrittlement," *Metall. Trans., vol. 4,* p. 589–594, 1973.

[20] D. P. Williams and H. G. Nelson, "Embrittlement of 4130 steel by low-pressure gaseous hydrogen," *Metall. Mater. Trans., vol. 1,* pp. 63-68, 1970.

[21] R. P. Gangloff and R. P. Wei, "Gaseous hydrogen embrittlement of high-strength steels," *Met. Trans,* vol. A8, no. 7, p. 1043–1053, 1977.

[22] W. W. Gerberich and A. G. Wright, "Recent studies of grain size and hydrogen concentration on hydrogen embrittlement in bcc metals," *2nd Intern. Conf. on Material Degradation,* p. 183–205.

[23] P. G. Marsh, W. Zielinski, H. Huang and W. W. Gerberich, "Crack-tip dislocation emission arrangements for equilibrium-III. Application to large applied stress intensities," *Acta Metall. Mater., vol. 40, no. 11,* p. 2883–2894, 1992.

[24] M. S. Daw and M. I. Baskes, "Application of the embedded atom method to hydrogen embrittlement," *Chem. Phys. Fract.,* p. 196–218, 1987.

[25] J. E. Angelo, W. W. Gerberich, N. R. Moody and S. M. Foiles, "Effects of Hydrogen on the Fracture Properties of 9 and 11 Tilt Boundaries in Nickel," *Materials Research Society symposium proceedings, vol. 278,* p. 159, 1992.

[26] U. Komaragiri, S. R. Agnew, R. P. Gangloff and M. R. Begley, "The role of macroscopic hardening and individual length-scales on crack tip stress elevation from phenomenological strain gradient plasticity," *J. Mech. Phys. Solids, vol. 56,* p. 3527–3540, 2008.

[27] Y. Lee and R. P. Gangloff, "Measurement and Modeling of Hydrogen Environment–Assisted Cracking of Ultra-High-Strength Steel," *Metall. Mater. Trans., vol. 38,* p. 2174–2190, 2007.

[28] C. D. Beachem, "A new model for hydrogen-assisted cracking (hydrogen embrittlement)," *Metall. Trans., vol. 3,* p. 437–451, 1972.

[29] I. M. Robertson and H. K. Birnbaum, "An HVEM study of hydrogen effects on the deformation and fracture of nickel," *Acta Metall., vol. 34,* p. 353–366, 1986.

[30] X. Li, X. Ma, J. Zhang, E. Akiyama, Y. Wang and X. Song, Review of Hydrogen Embrittlement in Metals: Hydrogen Diffusion, Hydrogen Characterization, Hydrogen Embrittlement Mechanism and Prevention, Acta Metallurgica Sinica (English Letters), 2020.

[31] S. A. Tetelman, “Fundamental Aspects of Stress Corrosion Cracking,” *Fundam. Asp. Stress Corros. Crack., vol. 446,* 1969.

[32] G. Lu, D. Orlikowski, I. Park, O. Politano and E. Kaxiras, “Energetics of hydrogen impurities in aluminum and their effect on mechanical properties,” *Phys. Rev., vol. 65, p. 64102, 2002.,* p. 64102, 2002.

[33] R. P. Gangloff, “Hydrogen assisted cracking of high strength alloys,” in *Comprehensive Structural Integrity, vol. 6*, New York, Eds. New York: Elsevier Science, 2003, p. 1–194.

[34] H. K. Birnbaum and P. Sofronis, “Hydrogen-enhanced localized plasticity–a mechanism for hydrogen-related fracture,” *Mater. Sci. Eng., vol. 176,* p. 191–202, 1994.

[35] P. Novak, R. Yuan, B. P. Somerday, P. Sofronis and R. O. Ritchie, “A statistical, physical-based, micro-mechanical model of hydrogen-induced intergranular fracture in steel,” *J. Mech. Phys. Solids, vol. 58,* p. 206–226, 2010.

[36] A. McNabb and P. K. Foster, “A new analysis of the diffusion of hydrogen in iron and ferritic steels,” *Trans. Metall. Soc. AIME, vol. 227,* p. 618–627, 1963.

[37] R. A. Oriani, “The diffusion and trapping of hydrogen in steel,” *Acta Metall., vol. 18,* p. 147–157, 1970.

[38] H. P. V. Leeuwen, “A Quantitative Model of Hydrogen Induced Grain Boundary Cracking,” *Corrosion, vol. 29,* p. 197–204, 1973.

[39] A. Turnbull and R. B. Hutchings, “Modelling of thermal desorption of hydrogen from metals,” *Mater. Sci. Eng., vol. 238,* p. 317–328, 1997.

[40] G. M. Pressouyre and I. M. Bernstein , “An example of the effect of hydrogen trapping on hydrogen embrittlement,” *Metall. Trans. A, vol. 12, no. 5,* p. 835–844, 1981.

[41] E. Barel, G. B. Hamu, D. Eliezer and L. Wagner, “The effect of heat treatment and HCF performance on hydrogen trapping mechanism in Timetal LCB alloy,” *J. Alloys Compd., vol. 468,* pp. 77-86, 2009.

[42] P. M. Novak, "A dislocation-based constitutive model for hydrogen-deformation interactions and a study of hydrogen induced intergranular fracture," PhD Thesis, University of Illinois at Urbana-Champaign, 2009.

[43] A. J. Kumnick and H. H. Johnson, "Deep trapping states for hydrogen in deformed iron," *Acta Metall., vol. 28,* p. 33–39, 1980.

[44] P. Sofronis, Y. Liang and N. Aravas, "Hydrogen induced shear localization of the plastic flow in metals and alloys," *Eur. J. Mech., vol. 20,* p. 857–872, 2001.

[45] G. J. Thomas, "Hydrogen trapping in FFC metals',," in *Hydrogen Effects in Metals, Proceedings of the Third International Conference on Effect of Hydrogen on Behavior of Materials*, New York, Eds. New York: Transactions of the Metallurgical Society AIME, 1981, pp. 77-85.

[46] J. Lufrano, P. Sofronis and D. Symons, "Hydrogen transport and large strain elastoplasticity near a notch in alloy X-750," *Eng. Fract. Mech., vol. 59, pp. 827–845, 1998.,* p. 827–845, 1998.

[47] J. C. M. Li, R. A. Oriani and L. Darken, "The thermodynamic of stressed solids," *Z für Phys Chem Neue Folge, vol. 49,* p. 271–290, 1966.

[48] S. Sun, "Investigation of deformation field and hydrogen partition around crack tip in fcc single crystal," *Metall. Mater. Trans., vol. 26,* p. 731–739, 1995.

[49] T. Zhang, W. Y. Chu, K. W. Gao and L. J. Qiao, "Study of correlation between hydrogen-induced stress and hydrogen embrittlement," *Mater. Sci. Eng., vol. 347,* p. 291–299, 2003.

[50] P. Sofronis and R. Mcmeeking, "Numerical analysis of hydrogen transport near a blunting crack tip," *Journal of the Mechanics and Physics of Solids 37 (3),* pp. 317 - 350, 1989.

[51] A. Krom, R. Koers and A. Bakker, "Hydrogen transport near a blunting crack tip.," *Journal of the Mechanics and Physics of Solids 47,* pp. 971 - 922, 1999.

[52] A. Turnbull, D. H. Ferriss and H. Anzai, "Modelling of hydrogen distribution at a crack tip," *Mater. Sci. Eng., vol. 206,* pp. 1-13, 1996.

[53] C. V. Di Leo and L. Anand, "Hydrogen in metals: A coupled theory for species diffusion and large elastic–plastic deformations," *Int. J. Plast., vol. 43,* p. 42–69, 2013.

[54] N. A. Fleck, G. M. Muller, M. F. Ashby and J. W. Hutchinson, "Strain gradient plasticity: theory and experiment," *Acta Metall. Mater., vol. 42,* p. 475–487, 1994.

[55] W. D. Nix and H. Gao, "Indentation size effects in crystalline materials: a law for strain gradient plasticity," *J. Mech. Phys. Solids, vol. 46,* p. 411–425, 1998.

[56] J. S. Stölken and A. G. Evans, "A microbend test method for measuring the plasticity length scale," *Acta materalia, vol. 46,* p. 5109–5115, 1998.

[57] E. Martínez-Pañeda, "Strain gradient plasticity-based modeling of damage and fracture," University of Oviedo, Oviedo, 2016.

[58] M. Dadfarnia, P. Sofronis and T. Neeraj, "Hydrogen interaction with multiple traps: can it be used to mitigate embrittlement?," *Int. J. Hydrogen Energy, vol. 36,* p. 10141–10148, 2011.

[59] M. Dadfarnia, M. L. Martin, A. Nagao, P. Sofronis and I. M. Robertson, "Modeling hydrogen transport by dislocations," *J. Mech. Phys. Solids, vol. 78,* p. 511–525, 2015.

[60] L. Jemblie, V. Olden and O. M. Akselsen, "A coupled diffusion and cohesive zone modelling approach for numerically assessing hydrogen embrittlement of steel structures," *Int. J. Hydrogen Energy, vol. 42,* p. 1980–11995, 2017.

[61] A. Alvaro, V. Olden and O. M. Akselsen, "3D cohesive modelling of hydrogen embrittlement in the heat affected zone of an X70 pipeline steel – Part II," *Int. J. Hydrogen Energy, vol. 39,* pp. 3528-3541, 2014.

[62] G. Bilotta, C. Moriconi, G. Hénaff and M. Arzaghi, "A cohesive zone model to simulate fatigue crack propagation under high pressure gaseous hydrogen," *Adv. Mater. Res., vol. 891,* p. 765–770, 2014.

[63] V. Olden, C. Thaulow, R. Johnsen, E. Østby and T. Berstad, "Influence of hydrogen from cathodic protection on the fracture susceptibility of 25%Cr duplex stainless steel – Constant load SENT testing and FE-modelling using hydrogen

influenced cohesive zone elements," *Engineering Fracture Mechanics 76,* pp. 827 - 844, 2009.

[64] C. Moriconi, "Modélisation de la propagation de fissure de fatigue assistée par l'hydrogène gazeux dans les matériaux métalliques.," Ph.d. thesis, 2012.

[65] J. H. Kumnick A., "Deep trapping states for hydrogen in deformed iron," *Acta Metallica 29,* pp. 33 - 39, 1980.

[66] D. S. Dugdale, "Yielding in Steel Sheets Containing Slits," *J. Mech. Phys. Solids 8,* pp. 100 - 104, 1960.

[67] G. I. Barenblatt, "The Mathematical Theory of Equilibrium Cracks," *Adv. Appl. Mech. 7,* pp. 55 - 129, 1962.

[68] S. Roth, G. Hütter and M. Kuna, "Simulation of fatigue crack growth with a cyclic cohesive zone model," *Int. J. Fract. 188,* pp. 23 - 45, 2014.

[69] M. Elices, G. V. Guinea, J. Gómez and J. Planas, "The cohesive zone model: advantages, limitations and challenges," *Eng. Fract. Mech. 69,* pp. 137 - 163, 2002.

[70] A. Cornec, I. Scheider and K.-H. Schwalbe, "On the practical application of the cohesive model," *Eng. Fract. Mech. 70,* pp. 1963 - 1987, 2003.

[71] A. Hillerborg, M. Modeer and P.-E. Petersson, "Analysis of Crack Formation and Crack Growth in Concrete by Means of Fracture Mechanics and Finite Elements," *Cem. Concr. Res. 6,* pp. 773 - 782, 1976.

[72] W. Brocks, A. Cornec and I. Scheider, "Computational aspects of nonlinear fracture mechanics," *Gkss Forschungszentrum Geesthacht 30,* pp. 2 - 187, 2003.

[73] W. I. Scheider, "The effect of the traction separation law on the results of cohesive zone propagation analyses," *Key Eng. Mater. 251–252,* p. 313 – 318, 2003.

[74] V. Tvergaard and J. W. Hutchinson, "The relation between crack growth resistance and fracture process parameters in elastic-plastic solids," *J. Mech. Phys. Solids, vol. 40,* p. 1377 – 1397, 1992.

[75] X. P. Xu and A. Needleman, "Void nucleation by inclusion debonding in a crystal matrix," *Model. Simul. Mater. Sci. Eng., vol. 1,* p. 111–132, 1993.

[76] X. P. Xu and A. Needleman, “Numerical simulations of fast growth in brittle solids,” *J. Mech. Phys. Solids, vol. 42,* p. 1397–1434, 1994.

[77] Z. P. Bazant, “Concrete fracture models: testing and practice,” *Eng. Fract. Mech., vol. 69,* p. 165–205, 2002.

[78] T. Siegmund and W. Brocks, “Modeling of crack growth in thin sheet aluminium alloys,” *ASTM Spec. Tech. Publ., no. 1389,* p. 475–485, 2000.

[79] M. Ortiz and A. Pandolfi, “Finite-deformation irreversible cohesive elements for three- dimensional crack- propagation analysis,” *Int. J. Numer. Methods Eng., vol. 44,* p. 1267–1282, 1999.

[80] W. Brocks, A. Cornec and I. Scheider, Comprehensive Structural Integrity, vol. Volume 3: Numerical and Computational Methods, 2003, pp. Pages 127-209.

[81] M. Elices, G. V. Guinea, J. Gómez and J. Planas, “The cohesive zone model: advantages, limitations and challenges,” *Eng. Fract. Mech., vol. 69,* p. 137–163, 2002.

[82] J. Planas, G. V. Guinea and M. Elices, “Size effect and inverse analysis in concrete fracture,” *Int. J. Fract., vol. 95,* p. 367–378, 1999.

[83] A. Needleman, “A continuum model for void nucleation by inclusion debonding,” *J. Appl. Mech., vol. 54,* p. pp. 525–531, 1987.

[84] A. Needleman, “An analysis of tensile decohesion along an interface,” *J. Mech. Phys. Solids, vol. 38,* p. pp. 289–324, 1990.

[85] V. Tvergaard and J. W. Hutchinson, “Effect of T-stress on mode I crack growth resistance in a ductile solid,” *Int. J. Solids Struct., vol. 31,* pp. 823–833,, 1994.

[86] V. Tvergaard and J. W. Hutchinson, “Toughness of an interface along a thin ductile layer joining elastic solids,” *Philos. Mag. A, vol. 70,* p. 2689–2703, 2001.

[87] V. Tvergaard, “Resistance curves for mixed mode interface crack growth between disimilar elastic-plastic solids,” *J. Mech. Phys. Solids, vol. 49,* p. 2689–2703, 2001.

[88] G. Lin, A. Cornec and K. H. Schwalbe, "Three-dimensional finite element simulation of crack extension in aluminium alloy 2024-FC," *Fatigue Fract. Eng. Mater. Struct., vol. 21,* p. 1159–1173, 1998.

[89] P. D. Zavattieri and H. D. Espinosa, "Grain level analysis of crack initiation and propagation in brittle solids," *Acta Materalia, vol. 49,* p. 195–208, 2001.

[90] A. L. Rosa, R. C. Yu, G. Ruiz and J. L. A. O. Sousa, "A loading rate dependent cohesive model for concrete fracture," *Eng. Fract. Mech., vol. 82,* p. 4291–4311, 2012.

[91] D. H. Allen and C. R. Searcy, "Micromechanical model for a viscoelastic cohesive zone," *Int. J. Fract., vol. 107pp.,* pp. 159–176,, 2001.

[92] M. G. A. Tijssens, E. Van der Giessen and L. J. Sluys, "Modelling of crazing using a cohesive surface methodology," *Mech. Mater., vol. 32,* p. 19–35, 2000.

[93] K. H. Schwalbe, I. Scheider and A. Cornec, Guidelines for applying cohesive models to the damage behaviour of engineering materials and structures, Berlin: Heidelberg: Springer Berlin Heidelberg, 2013.

[94] K. Park and G. H. Paulino, "Cohesive Zone Models: A Critical Review of Traction-Separation Relationships Across Fracture Surfaces," *Appl. Mech. Rev., vol. 2011,,* p. 60802, 2011.

[95] S. Roth, G. Hütter and M. Kuna, "Simulation of fatigue crack growth with a cyclic cohesive zone model," *Int. J. Fract., vol. 188,* p. 23–45, 2014.

[96] J. L. Bouvard, J. L. Chabobe, F. Feyel and F. Gallern, "A cohesive zone model for fatigue and creep–fatigue crack growth in single crystal superalloys," *Int. J. Fatigue, vol. 31,* p. 868–879, 2009.

[97] G. T. Camacho and M. Ortiz, "Computational modelling of impact damage in brittle materials," *Int. J. Solids Struct., vol. 33,* pp. 2899-2938, 1996.

[98] V. K. Goyal, E. R. Johnson and C. G. Davila, "Irreversible constitutive law for modeling the delamination process using interfacial surface discontinuities," *Compos. Struct., vol. 65,* pp. 289-305, 2004.

[99] L. J. Lucas, T. M. Black and D. P. Jones, “Use of cohesive elements in fatigue analysis,” *ASME Press. Vessel. Pip. Div. Conf.,* pp. 13-25, 2007.

[100] O. Nguyen, E. A. Repetto, M. Ortiz and R. A. Radovitzky, “A cohesive model of fatigue crack growth,” *Int. J. Fract., vol. 110,* p. 351–369, 2001.

[101] Y. Xu and H. Yuan, “Computational modeling of mixed-mode fatigue crack growth in quasi-brittle materials using extended finite element methods,” *Int. J. Fract., vol. 76,* p. 165–181, 2009.

[102] Y. Xu and H. Yuan, “On damage accumulations in the cyclic cohesive zone model for XFEM analysis of mixed-mode fatigue crack growth,” *Int. J. Fract., vol. 46,* p. 579–585, 2009.

[103] K. L. Roe and T. Siegmund, “An irreversible cohesive zone model for interface fatigue crack growth simulation,” *Eng. Fract. Mech., vol. 70,* p. 209–232, 2003.

[104] S. Brinckmann and T. Siegmund, “A cohesive zone model based on the micromechanics of dislocations,” *Mater. Sci. Eng., vol. 16,* p. 65003, 2008.

[105] J. Segurado and J. Llorca, “A new three-dimensional interface finite element to simulate fracture in composites,” *Int. J. Solids Struct., vol. 41 (11-22),* p. 2977–2993, 2004.

[106] H. Yu, J. S. Olsen, V. Olden, A. Alvaro, J. He and Z. Zhang, “Viscous regularization for cohesive zone modeling under constant displacement: An application to hydrogen embrittlement simulation,” *Eng. Fract. Mech., vol. 166,* p. 23–42, 2016.

[107] B. Wang and T. Siegmund, “A numerical analysis of constraint effects in fatigue crack growth by use of an irreversible cohesive zone model,” *Comput. Mater. Sci., vol. 132,* p. 175–196, 2005.

[108] B. Yang, S. Mall and K. Ravi-Chandar, “A cohesive zone model for fatigue crack growth in quasibrittle materials,” *Int. J. Solids Struct. vol. 22,* p. 3927–3944, 2001.

[109] H. H. M. Cleveringa, E. Van der Giessen and A. Needleman, “A discrete dislocation analysis of mode I crack growth,” *J. Mech. Phys. Solids, vol. 48,* p. 1133–1157, 2000.

[110] V. S. Deshpande, A. Needleman and E. Van der Giessen, "A discrete dislocation analysis of near-threshold fatigue crack growth," *Acta materalia, vol. 49,* p. 3189–3203, 2001.

[111] V. S. Deshpande, A. Needleman and E. Van der Giessen, "Discrete dislocation modeling of fatigue crack propagation," *Acta materalia, vol. 50,* p. 831–846, 2002.

[112] S. Brinckmann, T. Siegmund and Y. Huang, "A dislocation density based strain gradient model," *Int. J. Plast., vol. 22,* p. 1784–1797, 2006.

[113] F. O. Riemelmoser and R. Pippan, "Investigation of a growing fatigue crack by means of a discrete dislocation model," *Mater. Sci. Eng., vol. 234,* p. 135–137, 1997.

[114] Y. F. Gao and A. F. Bower, "A simple technique for avoiding convergence problems in finite element simulations of crack nucleation and growth on cohesive interfaces," *Model. Simul. Mater. Sci. Eng., vol. 12,* p. 453, 2004.

[115] V. Olden, C. Thaulow, R. Johnsen, E. Østby and T. Berstad, "Influence of hydrogen from cathodic protection on the fracture susceptibility of 25% Cr duplex stainless steel–Constant load SENT testing and FE-modelling using hydrogen influenced cohesive zone elements," *Eng. Fract. Mech., vol. 76,* p. 827–844, 2009.

[116] W. Brocks, R. Falkenberg and I. Scheider, "Coupling aspects in the simulation of hydrogen-induced stress-corrosion cracking," *Procedia IUTAM vol. 3,* pp. 11-24, 2012.

[117] E. Martínez-Pañeda and C. F. Niordson, "The role of Geometrically Necessary Dislocations in the fracture process of metallic materials," *12th International Conference on the Mechanical Behaviour of Materials,* p. 261, 2015.

[118] F. J. Gomez and M. Elices, "A fracture criterion for sharp V-notched samples," *Int. J. Fract., vol. 123, no. 3–4,* p. 163–175, 2003.

[119] F. J. Gomez and M. Elices, "A fracture criterion for blunted V-notched samples," *Int. J. Fract., vol. 127, no. 3,* p. 239–264, 2004.

[120] F. J. Gomez, G. V. Guinea and M. Elices, "Failure criteria for linear elastic materials with U-notches," *Int. J. Fract., vol. 141, no. 1–2,* p. 99–113, 2006.

[121] V. Olden, C. Thaulow, R. Johnsen and E. Østby, "Cohesive zone modeling of hydrogen-induced stress cracking in 25% Cr duplex stainless steel," *Scr. Mater., vol. 57, no. 7,* p. 615–618, 2007.

[122] D. A. Cendon, A. R. Torabi and M. Elices, "Fracture assessment of graphite V-notched and U-notched specimens by using the cohesive crack model," *Fatigue Fract. Eng. Mater. Struct., vol. 38, no. 5,* p. 563–573, 2015.

[123] D. De Meo, C. Diyaroglu, N. Zhu, E. Oterkus and M. Siddiq, "Modelling of stress-corrosion cracking by using peridynamics. Int. J. Hydrog. Energy 2016, 41(15), 6593-6609.," *Int. J. Hydrog. Energy 2016, 41(15), 6593-6609.,* pp. 6593-6609, 2016, 41(15).

[124] Y. Hirose and T. Mura, "Growth mechanism of stress corrosion cracking in high strength steel.," *Eng Fract Mech,* p. 19(6):1057e67., 1984.

[125] Y. Hirose and T. Mura, "Nucleation mechanism of stress corrosion cracking from notches.," *Eng Fract Mech,* p. 19(2):317e29, 1984.

[126] J. Rimoli and M. Ortiz, "A three-dimensional multiscale model of intergranular hydrogen-assisted cracking.," *Philos Mag,* pp. 90(917270850) - 2939-63, 2010.

[127] D. N. Jadhav and S. K. Maiti, "Characterization of stable crack growth through AISI 4340 steel using cohesive zone modeling and CTOD/CTOA criterion".

[128] D. De Meo, C. Diyaroglu, N. Zhu, E. Oterkus and M. Siddiq, "Modelling of stress-corrosion cracking by using peridynamics.," *Int. J. Hydrog. Energy, 41(15),* pp. 6593-6609, 2016.

[129] J. Rimoli, "A Computational Model for Intergranular Stress Corrosion Cracking," California Institute of Technology, Pasadena, California, 2009.

[130] R. Fernández-Sousa, C. Betegón and E. Martínez-Pañeda, "Analysis of the influence of microstructural traps on hydrogen assisted fatigue," *Acta Materialia 199,* pp. 253 - 263, 2020.

[131] A. Díaz, J. Alegre and I. Cuesta, "Coupled hydrogen diffusion simulation using a heat transfer analogy," *International Journal of Mechanical Sciences 115-116,* pp. 360 - 369., 2016.

[132] A. Taha and P. Sofronis, “A micromechanics approach to the study of hydrogen transport and embrittlement,” *Eng. Fract. Mech., vol. 68,* p. 803–837, 2001.

[133] G. R. Caskey and W. L. Pillinger, “Effect of trapping on hydrogen permeation,” *Metall. Mater. Trans., vol. 6,* p. 467–476, 1975.

[134] P. Sofronis, Y. Liang and N. Aravas, “Hydrogen induced shear localization of the plastic flow in metals and alloys,” *Eur. J. Mech. A/Solids 20,* p. 857–872, 2001.

[135] Y. Liang, P. Sofronis and R. J. Dodds, “Interaction of hydrogen with crack-tip plasticity: effects of constraint on void growth,” *Mater. Sci. Eng., vol. 366,* p. 397–411, 2004.

[136] M. R. Ayatollahi, A. R. Torabi and A. S. Rahimi, “Brittle fracture assessment of engineering components in the presence of notches: A review,” *Fatigue Fract. Eng. Mater. Struct., vol. 39, no. 3,* p. 267–291, 2016.

[137] Y. Hirose and T. Mura, “Nucleation mechanism of stress corrosion cracking from notches.,” *Eng Fract Mech,* vol. 19, no. 2, pp. 317-329, 1984.

[138] Y. Hirose and T. Mura, “Growth mechanism of stress corrosion cracking in high strength steel.,” *Eng Fract Mech,* vol. 19, no. 6, pp. 1057-1067, 1984.